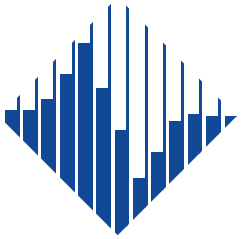

PACIFIC EARTHQUAKE ENGINEERING
RESEARCH CENTER

Implementation, Verification, and Validation of the PM4Sand Model in OpenSees

Long Chen
Pedro Arduino

Department of Civil and Environmental Engineering
University of Washington

PEER Report No. 2021/02

Pacific Earthquake Engineering Research Center
Headquarters at the University of California, Berkeley
April 2021

PEER 2021/02
April 2021

Disclaimer

The opinions, findings, and conclusions or recommendations expressed in this publication are those of the author(s) and do not necessarily reflect the views of the study sponsor(s), the Pacific Earthquake Engineering Research Center, or the Regents of the University of California.

Implementation, Verification, and Validation of the PM4Sand Model in OpenSees

Long Chen
Pedro Arduino

Department of Civil and Environmental Engineering
University of Washington

PEER Report No. 2021/02

Pacific Earthquake Engineering Research Center
Headquarters, University of California, Berkeley
March 2021

ABSTRACT

Human and economic losses caused by earthquake-induced soil liquefaction underscore the importance of assessing liquefaction hazards, both by determining whether a soil is likely to liquefy and by estimating consequences these events may cause. Numerical simulations have proven to be useful for these purposes. Reliable numerical analysis requires that constitutive models represent the *in situ* soil behavior as well as general loading and drainage conditions. For this purpose, comprehensive verification and validation studies of material models are imperative for successful deployment of advanced numerical tools. In this context, the main objective of this research is to implement, verify, and validate a newly developed constitutive model, PM4Sand (Boulanger and Ziotopoulou, 2017), using the finite-element platform OpenSees (OpenSees, 2007). This model was developed for earthquake engineering applications and can achieve reasonable approximations of desired behavior (including pore pressure generation and dissipation, limiting strains, and cyclic mobility) using a straightforward calibration process. After implementing PM4Sand in OpenSees, a parametric study was carried out to shed light on the model's general behavior and calibration process. Next, a verification study was performed to compare the response of the model implemented in three different frameworks, OpenSees, FLAC, and PLAXIS, using point, element, and one-dimensional model analyses. Lastly, a few well known case histories were considered to validate and demonstrate the model's ability to capture realistic soil behavior.

ACKNOWLEDGMENTS

The authors would like to thank two individuals who have contributed to this research in different forms:

- Andrew Makdisi at University of Washington for his contribution performing the 1D FLAC analysis presented in this report.
- Dr. Gregor Vilhar at PLAXIS B.V. for his contribution performing the 1D PLAXIS analysis presented in this report.

The authors acknowledge the NHERI DesignSafe Center and Texas Advanced Computing Center (TACC) at the University of Texas at Austin for providing high-performance computing resources that have contributed to the research results reported herein. Support from the University of Washington's Hyak HPC cyber infrastructure is also acknowledged.

This work was supported by the State of California through the Transportation Systems Research Program of the Pacific Earthquake Engineering Research (PEER) Center. Any opinions, findings, conclusions, or recommendations expressed in this material are those of the authors and do not necessarily reflect those of the funding agency or the Regents of the University of California.

CONTENTS

LIST OF FIGURES

LIST OF TABLES

1 Introduction

Through history earthquakes have caused tremendous losses of property and life. To mitigate these losses, the earth, social, and engineering sciences have made extensive efforts to reduce the risk of earthquake hazards. In this context, earthquake engineering has concentrated on developing methods that mitigate the aftermath of earthquakes on communities and their environment (Kramer, 1996). Geotechnical earthquake engineering, in particular, has focused on the engineering behavior of earth materials—especially soils—under earthquake shaking. Soil is a three-phase (air, water, and solids) composite. The interaction between these phases may cause complex behavior during earthquakes that may lead to instabilities. Soil liquefaction is one of these complex conditions that happens when the soil is fully or partially saturated, and the increase in pore water pressure, caused by shaking, reduces the inter-particle contact stress (effective stress) within solid particles, leading to substantial reduction in strength and stiffness. Under these circumstances soil can behave similarly to a viscous fluid. Liquefaction has been observed during many earthquakes including the 1964 Niigata earthquake, 1964 Alaska earthquake, 1989 Loma Prieta earthquake, 1995 Great Hanshin earthquake, 2010–11 Canterbury earthquake sequence, and the recent 2018 Sulawesi earthquake. Human and economic losses caused by earthquake-induced soil liquefaction underscore the importance of assessing liquefaction hazards, both by determining whether a soil is likely to liquefy and by anticipating subsequent damage.

Semi-empirical liquefaction triggering models have been developed based on frameworks of analysis that rely on case histories [Seed and Idriss (1971), Robertson and Wride (1998), Andrus and Stokoe (2000), Cetin et al. (2004), Moss et al. (2006), Idriss and Boulanger (2008)]. In general, these models are based on either SPT (Standard Penetration Test), CPT (Cone Penetration Test) or V_s (shear-wave velocity) field data, and include deterministic and probabilistic procedures. Efforts have also been made extending available databases to include more data from the recent New Zealand, Japan, and Indonesia earthquakes. However, the number of available case histories is still limited. In parallel to these efforts, numerical modeling has gained popularity and become an important tool to extend the understanding of liquefaction. Fully nonlinear modeling and advances in high-performance computing (HPC) now provide the opportunity to tackle problems at a greater scale and complexity and faster computing speed.

Constitutive models play a vital role in these analyses. Accurate and reliable numerical analyses require constitutive models to represent the *in situ* behavior of soil with different particle distributions, drainage conditions, and loading conditions. Models should be

able to capture soil behavior at the element level as observed in laboratory tests and 1D, 2D, and 3D geologic scenarios as observed in the field during earthquakes or reproduced by centrifuge tests. In this regard, both monotonic and dynamic behaviors, such as cyclic mobility and modulus reduction (Darendeli, 2001; Menq, 2003), are important. Furthermore, constitutive models by themselves only define stress–strain relationships and need to be implemented within boundary-value domain solution frameworks that include domain discretization. This means any model implemented into a numerical platform must be able to solve real problems. These platforms can be based on different numerical methods such as finite-element (FEM), finite-difference (FD), finite-volume (FVM), and particle based methods, like the material point method (MPM). FLAC (Itasca, 2016), PLAXIS (Plaxis.B.V, 2018), and OpenSees (OpenSees, 2007), are among the most popular codes currently available for these analyses.

To account for the nonlinear soil response, comprehensive constitutive models lay the foundation for simulating complex soil behavior. Unfortunately, they also add complexity to these models implementation. Therefore, before a model can be used in research and practice, verification and validation processes are necessary. ***Verification*** is meant to identify and remove programming errors in computer code and verify numerical algorithms. ***Validation*** is meant to assess the accuracy at which a numerical model represents reality and includes the essential features of a real model. Selecting representative properties for model's input is another vital step for a successful analysis. Spatial variability and uncertainty in soil properties is another imperative aspect to consider.

The research presented in this report aims to extend tools for nonlinear effective stress analysis and focuses on the verification and validation of an advanced constitutive model, referred as PM4Sand, implemented in the OpenSees computational framwork. PM4Sand is a sand plasticity model for earthquake engineering applications recently proposed by Boulanger and Ziotopoulou (2015, 2017). This 2D plane-strain model follows the plasticity framework proposed by Dafalias and Manzari (2004) and is based on bounding surface plasticity and critical state concepts. The model has been calibrated at an element level to capture general trends observed in the field and empirical correlations commonly used in geotechnical earthquake engineering practice. By changing three primary input parameters, the user can achieve reasonable approximations of desired behavior including pore pressure generation and dissipation, limiting strains, and cyclic mobility. Using secondary parameters (18 in total and optional), the user can further fine-tune the response although this is usually not necessary. Since its introduction, the PM4Sand model has drawn wide attention in geotechnical engineering practice and research communities due to its relatively easy calibration process and good agreement with field observations.

This report is organized in five chapters:

- **Chapter 2** presents an introduction to the PM4Sand model and details on its implementation in OpenSees. A parametric study is included to shed light on the model's capabilities and calibration process.
- **Chapter 3** presents simulation results to verify PM4Sand in OpenSees. For this purpose, monotonic and cyclic element tests were used to verify stress–strain behavior in carefully

controlled loading conditions. Then 1D canonical cases were used to verify the model's behavior in several computational frameworks. Results from FLAC and PLAXIS analyses were also considered and compared for verification purposes.

- **Chapter 4** presents simulation results to validate PM4Sand and OpenSees as a viable tool for site response analysis in liquefiable soils. For this purpose, the WildLife and Port Island liquefaction array case histories were used.

- **Chapter 5** presents summary and conclusions.

2 Implementation of PM4Sand in OpenSees

2.1 INTRODUCTION

This chapter presents a brief introduction to PM4Sand (Boulanger and Ziotopoulou, 2017) and its implementation in OpenSees. This 2D constitutive model follows the basic framework of the Dafalias and Manzari (2004) model (referred as MD model hereafter) based on bounding surface plasticity and critical state concepts. PM4Sand was developed specifically for plane–strain conditions and was simplified using only in-plane stresses. It has the advantage of simplifying the MD formulation and improving computational speed by reducing the number of operations (Boulanger and Ziotopoulou, 2017). Implementation details of the model's current version 3.1 are presented here. Readers are referred to the PM4Sand manual by Boulanger and Ziotopoulou (2017) for detailed information on the model.

2.2 INTRODUCTION TO PM4SAND

2.2.1 Elastic Response and Yield Surface

The model is based on effective stresses. Hence the conventional prime symbol is dropped from the stress terms for convenience. The matrix representation of the stress tensor, $\boldsymbol{\sigma}$, is simplified in plane-strain to,

$$[\boldsymbol{\sigma}] = \begin{bmatrix} \sigma_{xx} & \sigma_{xy} \\ \sigma_{xy} & \sigma_{yy} \end{bmatrix}, \tag{2.1}$$

where the brackets indicate matrix representation of the tensor, and a bold symbol represents a second-order tensor.

The mean confining pressure, p, is defined as,

$$p = \frac{\sigma_{xx} + \sigma_{yy}}{2}. \tag{2.2}$$

and the deviatoric stress tensor, $\mathbf{s}$, is defined as,

$$\mathbf{s} = \boldsymbol{\sigma} - p\mathbf{I}, \tag{2.3}$$

where $\mathbf{I}$ is the second-order unit tensor, and in matrix form results in

$$[\mathbf{s}] = [\boldsymbol{\sigma}] - p[\mathbf{I}] = \begin{bmatrix} s_{xx} & s_{xy} \\ s_{xy} & s_{yy} \end{bmatrix} = \begin{bmatrix} \sigma_{xx} - p & \sigma xy \\ \sigma xy & \sigma_{yy} - p \end{bmatrix}, \tag{2.4}$$

The volumetric strain in plane–strain is,

$$\epsilon_v = \epsilon_{xx} + \epsilon_{yy}\,, \tag{2.5}$$

and the deviatoric strain tensor, $\mathbf{e}$, is defined as,

$$\mathbf{e} = \boldsymbol{\epsilon} - \frac{\epsilon_v}{3}\mathbf{I}\,, \tag{2.6}$$

with matrix represented in the form,

$$[\mathbf{e}] = [\boldsymbol{\epsilon}] - \frac{\epsilon_v}{3}[\mathbf{I}] = \begin{bmatrix} \epsilon_{xx} - \frac{\epsilon_v}{3} & \epsilon_{xy} \\ \epsilon_{xy} & \epsilon_{xx} - \frac{\epsilon_v}{3} \end{bmatrix}. \tag{2.7}$$

The elastic deviatoric strain increment is,

$$\dot{\mathbf{e}}^{el} = \frac{d\mathbf{s}}{2G}\,, \tag{2.8}$$

where the shear modulus G is calculated using the mean stress p and current stress ratio as,

$$G = G_o p_A (\frac{p}{p_A})^{1/2} C_{SR}\,, \tag{2.9}$$

where G_o is a scalar parameter, p_A is atmospheric pressure for normalization, ν is Poisson ratio, and C_{SR} is a factor that accounts for the stress-ratio effect. C_{SR} is defined as,

$$C_{SR} = 1 - C_{SR,o} \cdot (\frac{\eta}{M^b})^{m_{SR}}\,, \tag{2.10}$$

where $C_{SR,o}, m_{SR}$ are constants, $\eta = q/p$ is the current stress ratio, and q is the difference in the major and minor principal in-plane stresses, or

$$q = \sqrt{(\sigma_{xx} - \sigma_{yy})^2 + (2\tau_{xy})^2}\,, \tag{2.11}$$

M^b is the bounding stress ratio, which is described later. In the current implementation, $C_{SR,o} = 0.5$ and $m_{SR} = 4$. The bulk modulus K is computed as,

$$K = \frac{2(1+\nu)}{3(1-2\nu)}G\,. \tag{2.12}$$

The yield surface is described by a cone in the principal stress space and can be defined in stress terms as,

$$f = [(\mathbf{s} - p\boldsymbol{\alpha}) : (\mathbf{s} - p\boldsymbol{\alpha})]^{1/2} - \sqrt{1/2}pm = 0\,, \tag{2.13}$$

or in terms of stress ratio as,

$$f = [(\mathbf{r} - \boldsymbol{\alpha}) : (\mathbf{r} - \boldsymbol{\alpha})]^{1/2} - \sqrt{1/2}m = 0\,, \tag{2.14}$$

where $\mathbf{r} = \mathbf{s}/p$ is the stress ratio, $\boldsymbol{\alpha}$ is back-stress ratio tensor that defines the center of the yield surface in stress ratio space, and m defines the radius of the cone.

2.2.2 Critical State Surface

The PM4Sand model incorporates the concept of critical state for soil, as defined by Schofield and Wroth (1968) and Muir Wood (1990). However, instead of the critical void ratio, e_c, the relative density at the critical state, $D_{R,cs}$, as presented by Bolton (1986) is used to define critical state in a $D_R - p$ space. Using this idea, Boulanger (2003a) used the relative state parameter index ξ_R defined as,

$$\xi_R = D_{R,cs} - D_R \,, \tag{2.15}$$

to relate soil behavior with the critical state. In Equation 2.15 D_R is the current relative density, and $D_{R,cs}$ is the relative density at a critical state for a current mean effective stress, which is defined as,

$$D_{R_cs} = \frac{R}{Q - \ln(100\frac{p}{p_A})} \,, \tag{2.16}$$

where Q and R for quartz sand were shown by Bolton to be 10 and 1.0, respectively. Using default values for $e_{max} = 0.8$ and $e_{min} = 0.5$, a default critical state line for the PM4Sand model can be plotted in $e - p$ space and compared with critical state lines calibrated for the MD model. The MD model has been calibrated for several sands, e.g., Nevada sand, Toyoura sand, Ottawa sand, etc., using laboratory tests; see Taiebat et al. (2010); Ramos (2010), Ramirez et al. (2018a), and Ghofrani (2018). In Figure 2.1, these critical lines are plotted together with the default critical state line for PM4Sand in $e-p$ space. As shown in the figure, the default critical state line provides a reasonable estimation of critical states for general sands when high-quality laboratory tests data are not available for calibration. In the $q - p$ space, the critical stress-state ratio is defined as $M = \frac{q_c}{p_c}$, where M can be related to the effective stress friction angle at critical state ϕ_{cv} as,

$$M = 2 \cdot \sin(\phi_{cv}) \,, \tag{2.17}$$

where ϕ_{cv} is the constant volume friction angle.

2.2.3 Bounding and Dilatancy Surfaces

The model simplifies the bounding, dilatancy, and critical state surfaces presented by Dafalias and Manzari (2004) by removing the Lode angle dependency. In PM4Sand, bounding and dilatancy ratios are related to critical stress ratio by,

$$M^b = M \cdot \exp(-n^b \xi_R) \,, \tag{2.18}$$

$$M^d = M \cdot \exp(n^d \xi_R) \,, \tag{2.19}$$

where n^b and n^d are model parameters. The default value of n^b is 0.50, and $n^b/4$ is used to compute M^b for loose of critical states. The default value of n^d is 0.10 and $4n^d$ is used to compute M^d for dense of critical states.

An image back-stress ratio tensor at the bounding surface is defined as,

$$\boldsymbol{\alpha}^b = \sqrt{1/2}[M^b - m]\mathbf{n} \,, \tag{2.20}$$

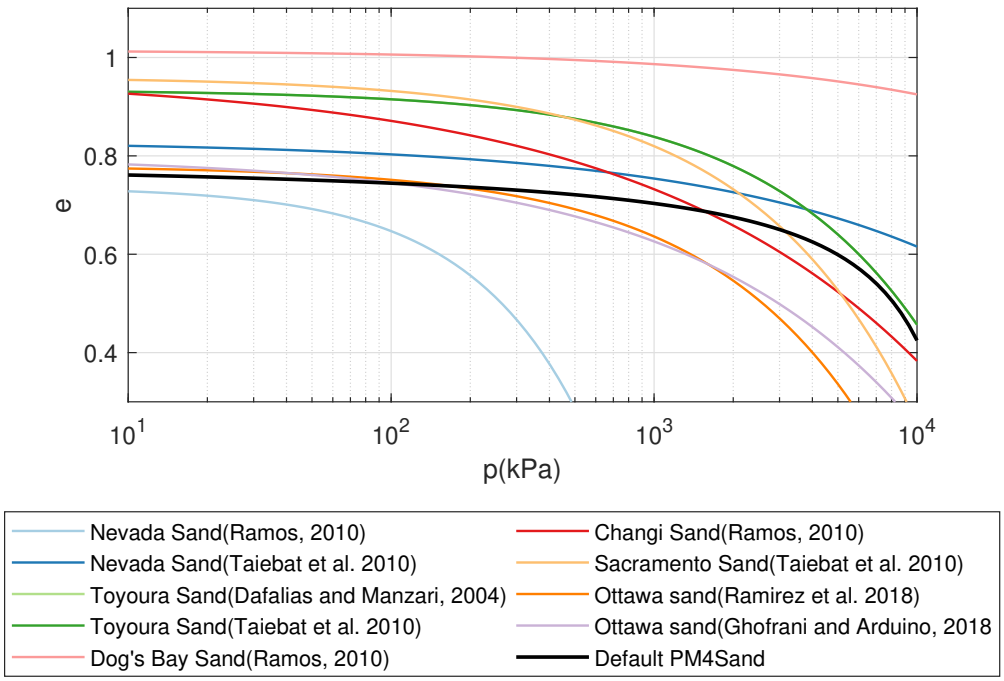

Figure 2.1: Default critical state line for PM4Sand compared to similar curves calibrated for MD.

where $\mathbf{n}$ is a second-order tensor representing the normal to the yield surface.

An image back-stress ratio tensor at the dilatancy surface is defined as,

$$\boldsymbol{\alpha}^d = \sqrt{1/2}[M^d - m]\mathbf{n}\,. \tag{2.21}$$

2.2.4 Flow Rule

The loading index, L, is used to compute the plastic component of volumetric and deviatoric strain increments as,

$$\dot{\epsilon_v^p} = \langle L \rangle D\,, \tag{2.22}$$

$$\dot{\boldsymbol{\epsilon}^p} = \langle L \rangle \mathbf{R}'\,, \tag{2.23}$$

where D is a dilatancy parameter; $\mathbf{R}$ is the direction of plastic strain increment $\dot{\boldsymbol{\epsilon}^p}$; $\mathbf{R}'$ is the deviatoric component of $\mathbf{R}$; and $\langle\rangle$ are MacCauley brackets. The tensor $\mathbf{R}$ for the assumption of no Lode angle dependency is,

$$\mathbf{R} = \mathbf{n} + \frac{1}{3}D\mathbf{I}\,. \tag{2.24}$$

The dilatancy parameter D relates the plastic volumetric strain increment to the magnitude of the plastic deviatoric strain increment,

$$D = \frac{\dot{\epsilon_v^p}}{|\dot{\boldsymbol{\epsilon}^p}|}\,, \tag{2.25}$$

The loading index, as derived in Dafalias and Manzari (2004) is,

$$L = \frac{1}{K_p}\frac{\partial f}{\partial \boldsymbol{\sigma}} : \dot{\boldsymbol{\sigma}} = \frac{1}{K_p}[\mathbf{n} : \dot{\mathbf{s}} - \mathbf{n} : \mathbf{r}\dot{p}]\,, \tag{2.26}$$

or

$$L = \frac{2G\mathbf{n} : \dot{\mathbf{e}} - \mathbf{n} : \mathbf{r}K\dot{\epsilon_v}}{K_p + 2G - KD\mathbf{n} : \mathbf{r}}\,, \tag{2.27}$$

and the stress increment for an imposed strain increment can be computed as,

$$\dot{\boldsymbol{\sigma}} = 2G\dot{\mathbf{e}} + K\dot{\epsilon}_v\mathbf{I} - \langle L\rangle(2G\mathbf{n} + KD\mathbf{I})\,, \tag{2.28}$$

2.2.5 Harding Rule

In the original MD model, the plastic modulus is defined as,

$$K_p = \frac{2}{3}Gh_0\frac{(\boldsymbol{\alpha}^b - \boldsymbol{\alpha}) : \mathbf{n}}{(\boldsymbol{\alpha} - \boldsymbol{\alpha}_{in}) : \mathbf{n}}\,, \tag{2.29}$$

where $\boldsymbol{\alpha}_{in}$ is the initial back stress ratio at the start of a loading branch. In the current implementation of PM4Sand, $\boldsymbol{\alpha}_{in}$ is updated at each loading reversal, which is determined when,

$$(\boldsymbol{\alpha} - \boldsymbol{\alpha}_{in}) : \mathbf{n}_{trial} < 0\,, \tag{2.30}$$

where $\mathbf{n}_{trial}$ is the trial norm to the yield surface.

During loading reversals, an "overshooting" problem may appear. This is a well-known problem in bounding surface plasticity; see Dafalias (1986). As a demonstration of the problem, Figure 2.2 depicts an undrained DSS simulation with gradually increasing CSR for loading reversals. Suppose that after loading with a given $\boldsymbol{\alpha}_{in}$, a very small reverse loading eliminates the previous $\boldsymbol{\alpha}_{in}$ so that if loading in the original direction (or nearby directions) is resumed, the process will begin with a new $\boldsymbol{\alpha}_{in}$. As a result, the corresponding stress–strain curve will "overshoot" the continuation of the previous curve, which would have occurred if no unloading/reverse loading/reloading had taken place (because at the initiation of the reloading $\boldsymbol{\alpha}_{in} = \boldsymbol{\alpha}$ and Equation 2.29 yields $Kp = \infty$). As the loading continues, the over-estimated K_p would produce over-stiffening in the response compared to a continuing branch without the small loading reversal. Such "overshooting," however, is not out of control because the existence of the bounds in stress-strain space restricts its extent; as shown in the black curve after around 0.5% of shear strain. Nevertheless, this is not a desirable feature, and in the current version of PM4Sand an apparent initial back stress ratio $\boldsymbol{\alpha}_{in}^{app}$ and previous (apparent) initial back stress ratio $\boldsymbol{\alpha}_{in}^{p}$ are introduced to remedy the problem. The components of $\boldsymbol{\alpha}_{in}^{app}$ are taken as: (i) for positive loading directions, the minimum (positive) value they have ever had, but smaller than zero; and (ii) for negative loading directions, the maximum (negative) value they have ever had, but no greater than zero. In this context, $\boldsymbol{\alpha}_{in}^{max}$, which is non-positive, and $\boldsymbol{\alpha}_{in}^{min}$, which is non-negative, are also tracked during loading. The $\boldsymbol{\alpha}_{in}$ from the MD model is then named $\boldsymbol{\alpha}_{in}^{true}$ in PM4Sand. A

factor C_{rev} is introduced in K_p to soften the stress-strain response when $\boldsymbol{\alpha}$ does not exceed $\boldsymbol{\alpha}_{in}^{app}$, i.e., $(\boldsymbol{\alpha} - \boldsymbol{\alpha}_{in}^{app}) : \mathbf{n} \leq 0$.

$$\begin{aligned} C_{rev} &= \frac{(\boldsymbol{\alpha} - \boldsymbol{\alpha}_{in}^{app}) : \mathbf{n}}{(\boldsymbol{\alpha} - \boldsymbol{\alpha}_{in}^{true}) : \mathbf{n}} \quad for \quad (\boldsymbol{\alpha} - \boldsymbol{\alpha}_{in}^{p}) : \mathbf{n} \leq 0 \\ &= 1 \quad \text{otherwise.} \end{aligned} \tag{2.31}$$

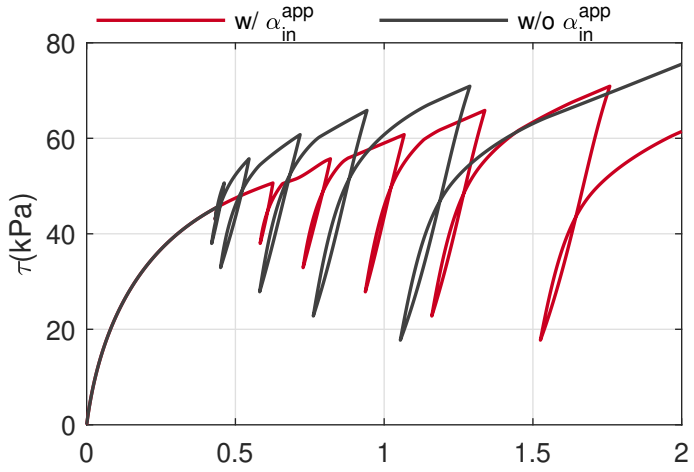

Figure 2.2: Effect of apparent initial back-stress ratio α_{in}^{app} to avoid "overshooting" following a small loading reversal.

The formulation for K_p is then modified to,

$$\begin{aligned} K_p &= Gh_o \frac{[(\boldsymbol{\alpha}^b - \boldsymbol{\alpha}) : \mathbf{n}]^{0.5}}{[\exp[(\boldsymbol{\alpha} - \boldsymbol{\alpha}_{in}^{app}) : \mathbf{n}] - 1] + C_{\gamma 1}} C_{rev} \\ &= Gh_o \frac{(\boldsymbol{\alpha}^b - \boldsymbol{\alpha}) : \mathbf{n}}{[[\exp[(\boldsymbol{\alpha} - \boldsymbol{\alpha}_{in}^{app}) : \mathbf{n}] - 1] + C_{\gamma 1}][(\boldsymbol{\alpha}^b - \boldsymbol{\alpha}) : \mathbf{n}]^{0.5}} C_{rev} \,, \end{aligned} \tag{2.32}$$

where $C_{\gamma 1}$ is added to prevent the denominator from becoming zero and generate nonlinearity even when $(\boldsymbol{\alpha} - \boldsymbol{\alpha}_{in}^{app}) : \mathbf{n}$ is small. Calibrations by Boulanger and Ziotopoulou (2017) show $C_{\gamma 1} = h_0/200$ produces a reasonable response. For a state with a stress ratio outside the bounding surface ($(\boldsymbol{\alpha}^b - \boldsymbol{\alpha}) : \mathbf{n} < 0$) and loose than critical ($\xi_R < 0$) condition, K_p is set to zero instead of allowing negative values. This restriction on K_p improves numerical stability but has little effect on the stress–strain response.

Assuming no isotropic hardening, $\dot{m} = 0$, and K_p is related to kinematic hardening aspects only as defined in Dafalias and Manzari (2004); therefore,

$$\dot{\boldsymbol{\alpha}} = \langle L \rangle \frac{2}{3} h (\boldsymbol{\alpha}_\sigma^b - \boldsymbol{\alpha}) \,, \tag{2.33}$$

where h is the hardening coefficient, and $\boldsymbol{\alpha}_\sigma^b - \boldsymbol{\alpha}$ is a distance between the bounding and current back-stress ratio tensors. The factor of 2/3 is included for convenience so that

model constants are the same in triaxial and multi-axial formulations. Using the consistency condition $\dot{f} = 0$, one can get,

$$K_p = \frac{2}{3} ph(\boldsymbol{\alpha}^b - \boldsymbol{\alpha}) : \mathbf{n} = \frac{2}{3} ph\mathbf{b} : \mathbf{n}\,, \tag{2.34}$$

where $\mathbf{b} = \boldsymbol{\alpha}^b - \boldsymbol{\alpha}$. This expression can be rearranged to show that the consistency equation can be satisfied by expressing the hardening coefficient as,

$$h = \frac{2}{3} \frac{K_p}{p(\boldsymbol{\alpha}^b - \boldsymbol{\alpha}) : \mathbf{n}}\,. \tag{2.35}$$

2.2.6 Dilatancy

Dilation

The dilatancy parameter D is made proportional to the difference between the current stress ratio and the dilatancy stress ratio defined by the dilatancy surface. Depending on $(\boldsymbol{\alpha}^d - \boldsymbol{\alpha}) : \mathbf{n} \lessgtr 0$, contraction ($D > 0$), dilation ($D < 0$), or zero volumetric rate ($D = 0$) can be obtained. Following the original MD formulation,

$$D = A_{do} \cdot [(\boldsymbol{\alpha}^d - \boldsymbol{\alpha}) : \mathbf{n}]\,, \tag{2.36}$$

where A_{do} can be related to the dilatancy relationship proposed by Bolton (1986),

$$A_{do} = \frac{1}{0.4} \frac{sin^{-1}(\frac{M^b}{2}) - sin^{-1}(\frac{M}{2})}{M^b - M^d}\,. \tag{2.37}$$

Contraction

In the MD model, plastic volumetric strain during both contraction and dilation is computed using,

$$D = A_{do} \cdot [(\boldsymbol{\alpha}^d - \boldsymbol{\alpha}) : \mathbf{n}]\,. \tag{2.38}$$

Although robust, this relatively simple expression has shown limitations in estimating cyclic resistance ratios (CRR); see Ghofrani and Arduino (2017) and Ramirez et al. (2018a). Therefore, in PM4Sand, the plastic volumetric strain during contraction is modified to the following expression,

$$D = A_{dc}[(\boldsymbol{\alpha} - \boldsymbol{\alpha}_{in}^{app}) : \mathbf{n}]^2 \frac{(\boldsymbol{\alpha}^d - \boldsymbol{\alpha}) : \mathbf{n}}{(\boldsymbol{\alpha}^d - \boldsymbol{\alpha}) : \mathbf{n} + C_D}\,, \tag{2.39}$$

where

$$A_{dc} = \frac{A_{do}}{h_p}. \tag{2.40}$$

The term $\frac{(\boldsymbol{\alpha}^d - \boldsymbol{\alpha}):\mathbf{n}}{(\boldsymbol{\alpha}^d - \boldsymbol{\alpha}):\mathbf{n} + C_D}$ ensures that D goes to zero smoothly as $\boldsymbol{\alpha}$ approaches $\boldsymbol{\alpha}^d$. C_D has a value of 0.10 in the current implementation in FLAC; As will be shown, $C_D = 0.16$ in

OpenSees provides a better match to the results from FLAC; therefore the value of 0.16 is implemented in OpenSees. A detailed discussion on the choice of this value is presented in Chapter 3.

$$h_p = h_{po} \exp(-0.7 + 7.0(0.5 - \xi_R)^2) \quad for \quad \xi_R \leq 0.5\,, \tag{2.41}$$

$$h_p = h_{po} \exp(-0.7) \quad for \quad \xi_R > 0.5\,, \tag{2.42}$$

where the sate parameter ξ_R is defined in Equation (2.15). An upper limit is imposed on the contraction rate, such that

$$D \leq 1.5 \cdot A_{do} \frac{(\boldsymbol{\alpha}^d - \boldsymbol{\alpha}) : \mathbf{n}}{(\boldsymbol{\alpha}^d - \boldsymbol{\alpha}) : \mathbf{n} + C_D}\,. \tag{2.43}$$

Effect of Fabric

Following the idea proposed in MD, a fabric tensor $\mathbf{z}$ is used to account for strain accumulation based on previous strain history. The change of fabric is based on plastic volumetric strain during dilation,

$$\dot{\mathbf{z}} = \frac{c_z}{1 + \langle \frac{z_{cum}}{2 z_{max}} - 1 \rangle} \frac{\langle -\dot{\epsilon}_v^p \rangle}{D} (z_{max}\mathbf{n} + \mathbf{z})\,, \tag{2.44}$$

where the parameter c_z controls the rate of fabric accumulation, and z_{max} controls the maximum value of $\mathbf{z}$. The scalar z_{cum} is the cumulative value of absolute change in $\mathbf{z}$; its rate is,

$$\dot{z}_{cum} = |\dot{\mathbf{z}}|\ . \tag{2.45}$$

The greatest past peak value for $\mathbf{z}$, z_{peak}, is tracked as,

$$z_{peak} = max(\sqrt{\frac{\mathbf{z} : \mathbf{z}}{2}}, z_{peak})\,. \tag{2.46}$$

Similar to $\boldsymbol{\alpha}_{in}$, the initial fabric tensor, $\mathbf{z}_{in}$, at each loading branch is also tracked and updated when a loading direction reversal is detected. This term is used to describe the degree of stress rotation and its effect on dilative plastic volumetric strain. The mean stress at which the fabric is formed, p_{zp}, along with zxp, defined as the product of $|\mathbf{z}|$ and p, are also tracked during loading; p_{zp} plays an important role in the plastic modulus and dilative plastic volumetric strain. It is used to address a couple of issues, including the issue of how fabric is formed during liquefaction and may be erased during reconsolidation. More details can be found in Boulanger and Ziotopoulou (2017). Note they are both positive in the current OpenSees implementation as will be discussed later. p_{zp} and zxp are updated at the same time whenever the current p_{zp} and zxp values exceed their previous peak value, respectively. Note: in the current implementation in FLAC 8.0, p_{zp} is always updated at the first loading reversal even though no fabric is formed. In order to better match the material behavior from FLAC, this change in p_{zp} is also allowed in OpenSees using a flag called $m\_pzpFlag$, which is set as true initially and changes to false after the first change of p_{zp}.

Effect of Fabric on Plastic Modulus

The plastic modulus K_p is expected to reduce as the fabric tensor grows. Therefore, Equation (2.32) is modified to,

$$K_p = Gh_o \frac{[(\boldsymbol{\alpha}^b - \boldsymbol{\alpha}) : \mathbf{n}]^{0.5}}{[\exp[(\boldsymbol{\alpha} - \boldsymbol{\alpha}_{in}^{app}) : \mathbf{n}] - 1] + C_{\gamma 1}} C_{rev} \frac{C_{k\alpha}}{1 + C_{K_p}\Big(\frac{z_{peak}}{z_{max}}\Big)\langle(\boldsymbol{\alpha}^b - \boldsymbol{\alpha}) : \mathbf{n}\rangle\sqrt{1 - C_{zpk2}}}\,, \tag{2.47}$$

where,

$$C_{k_\alpha} = 1 + \frac{C_{k\alpha f}}{1 + \big(2.5 \cdot \langle(\boldsymbol{\alpha} - \boldsymbol{\alpha}_{in}^{true}) : \mathbf{n}\rangle\big)^2} \cdot C_{pzp2} \cdot C_{zpk1}\,, \tag{2.48}$$

$$C_{zpk1} = \frac{z_{peak}}{z_{cum} + \dfrac{z_{max}}{5}}\,, \tag{2.49}$$

$$C_{zpk2} = \frac{z_{peak}}{z_{cum} + \dfrac{z_{max}}{100}}\,, \tag{2.50}$$

$$C_{pzp2} = \frac{\langle pzp - p\rangle}{\langle pzp - p\rangle + p_{min}}\,, \tag{2.51}$$

and

$$G = G_o p_A (\frac{p}{p_A})^{1/2} C_{SR} (\frac{1 + \dfrac{z_{cum}}{z_{max}}}{1 + \dfrac{z_{cum}}{z_{max}} C_{GD}})\,. \tag{2.52}$$

Details on these additional terms can be found in Boulanger and Ziotopoulou (2017).

Effect of Fabric on Volumetric Dilation

With the effect of fabric, the term A_{do} in Equation (2.36) is modified to,

$$A_d = \frac{A_{do} C_{zin2}}{(\frac{z_{cum}^2}{z_{max}})\big(1 - \frac{\langle -\mathbf{z}:\mathbf{n}\rangle}{\sqrt{2}\cdot z_{peak}}\big)^3 C_\epsilon^2 C_{pzp} C_{pmin} C_{zin1} + 1}\,, \tag{2.53}$$

where C_ϵ is a constant used to control the rate of plastic shear strain accumulation, and its default value varies with relative density as,

$$C_\epsilon = \begin{cases} = 0.2, & D_R > 0.75\,, \\ = 0.5 - (D_R - 0.55) \cdot 1.5 & 0.55 < D_R < 0.75\,, \\ = 0.5 & D_R < 0.55\,. \end{cases} \tag{2.54}$$

Note that Equation (2.54) is different than what is presented in Boulanger and Ziotopoulou (2017). The equation presented here is the same as that implemented in FLAC, which has

been confirmed by the model developers. C_{pzp} removes the effect of fabric on dilation when p is close to p_{zp} and is defined as,

$$C_{pzp} = \frac{1}{1 + (\frac{2.5p}{p_{zp}})^5} \,. \tag{2.55}$$

C_{pmin} removes the effect of fabric on dilation when p is sufficiently small and is defined as

$$C_{pmin} = \frac{1}{1 + (\frac{p_{min2}}{p})^2} \,. \tag{2.56}$$

Parameters p_{min2} and p_{min} (discussed below) are used to control the model behavior at small confining pressures and to obtain a better CRR curve slope. They are initialized when *FirstCall* is activated and their values are taken as,

$$p_{min} = \frac{p}{200} \, and \tag{2.57}$$

$$p_{min2} = \frac{p}{20} \,. \tag{2.58}$$

The term C_{zin1} facilitates strain-hardening when stress reversals are not causing fabric changes and it is defined as,

$$C_{zin1} = 1.0 - \exp\Big(-2.0 \Big| \frac{\mathbf{z}_{in} : \mathbf{n} - \mathbf{z} : \mathbf{n}}{z_{max}} \Big| \Big) \,. \tag{2.59}$$

The term C_{zin2} is used to decrease dilatancy by up to a factor of 3 under conditions of large strains and full stress reversals. It is defined as,

$$C_{zin2} = \frac{1 + C_{zin1} \dfrac{z_{cum} - z_{peak}}{3 z_{max}}}{1 + 3 \cdot C_{zin1} \dfrac{z_{cum} - z_{peak}}{3 z_{max}}} \,. \tag{2.60}$$

During dilation at very low effective stresses, i.e., $p \leq 2p_{min}$, D is constrained to ensure soil at dense than critical states continue to be dilative. For this purpose,

$$D = -3.5 A_{do} \langle M^b - M^d \rangle \frac{2p_{min} - p}{p_{min}} \,. \tag{2.61}$$

Effect of Fabric on Volumetric Contraction

With the effect of fabric, Equation (2.39) is extended to,

$$D = A_{dc} \cdot [(\boldsymbol{\alpha} - \boldsymbol{\alpha}_{in}^{app}) : \mathbf{n} + C_{in}]^2 \frac{(\boldsymbol{\alpha}^d - \boldsymbol{\alpha}) : \mathbf{n}}{(\boldsymbol{\alpha}^d - \boldsymbol{\alpha}) : \mathbf{n} + C_D} C_{pmin2} \,. \tag{2.62}$$

where A_{dc} also evolves with fabric as,

$$A_{dc} = \frac{A_{do}(1 + \langle \mathbf{z} : \mathbf{n} \rangle)}{h_p C_{dz}} \,. \tag{2.63}$$

where the term C_{dz} is included to increase the rate of contraction as z_{peak} approaches z_{max}, or a large amount of cumulative fabric formation/destruction has taken place. It is defined as,

$$C_{dz} = \Big(1 - C_{rot2} \cdot \frac{\sqrt{2} z_{peak}}{z_{max}}\Big)\Big(\frac{z_{max}}{z_{max} + C_{rot2} \cdot z_{cum}}\Big) \geq \frac{1}{1 + \frac{z_{max}}{2}} \ . \tag{2.64}$$

where C_{rot2} is defined as,

$$C_{rot2} = 1 - \frac{z_{peak}}{z_{cum} + \frac{z_{max}}{100}} \ . \tag{2.65}$$

The term C_{in} is included to enhance the contraction rate at the start of an unloading cycle; it is defined as,

$$C_{in} = \frac{2\langle \mathbf{z} : \mathbf{n} \rangle}{\sqrt{2} z_{max}} \, . \tag{2.66}$$

The term C_{pmin2} slows the rate of contraction when p is approaching p_{min} and stops further contraction when p is less than twice p_{min}. A linear variation is defined as,

$$C_{pmin2} = \begin{cases} = 0, & p \leq 2p_{min} \, , \\ = \frac{p - 2p_{min}}{16 p_{min}} & 2p_{min} < p < 18 p_{min} \, , \\ = 1 & p \geq 18 p_{min} \, . \end{cases} \tag{2.67}$$

This term is used to improve stability of the model at small confining pressures. It has a significant effect on the variation of p and, in turn, on the stress dependent behavior of the model, especially in how it relates to shear–strain accumulation.

Readers are encouraged to refer to the PM4Sand manual by Boulanger and Ziotopoulou (2017) for more details on these issues.

Post-Shaking Reconsolidation

Several studies (Ziotopoulou and Boulanger, 2013; Howell et al., 2014) have shown that predicted numerical volumetric strains tend to be much smaller than those observed in experimental studies. To improve the estimation of post-shake reconsolidation settlement, PM4Sand incorporates a function users can activate to reduce the value for the elastic shear and bulk modulus after a main shake. Then, the post-shaking elastic moduli can be determined by applying a reduction factor F_{sed} such that,

$$G_{post-shaking} = F_{sed} G \, , \tag{2.68}$$

$$K_{post-shaking} = F_{sed} K \, , \tag{2.69}$$

where F_{sed} is related to the accumulated fabric and the stress state at the end of the main shake; it can be calculated as,

$$F_{sed} = F_{sed,min} + (1 - F_{sed,min})(\frac{p}{20 p_{sed}})^2 \leq 1 \, , \tag{2.70}$$

where p_{sed} is,

$$p_{sed} = p_{sed_o}(\frac{z_{cum}}{z_{cum} + z_{max}}) \left\langle 1 - \frac{M^{cur}}{M^d} \right\rangle^{0.25} , \tag{2.71}$$

and $F_{sed,min}$ is,

$$F_{sed,min} = 0.03 * \exp(2.6 * D_R) \leq 0.99 , \tag{2.72}$$

and p_{sed_o} is,

$$p_{sed_o} = -\frac{P_{atm}}{5} . \tag{2.73}$$

Figure 2.3 compares the results between a liquefied 1D-level ground array obtained using OpenSees with and without *PostShake* activated after the main shake. The figure shows the increased predicted settlements due to the reduced stiffness meant to compensate for post-shake reconsolidation. It also shows that the excess pore pressure dissipation rate is also affected due to the reduction in the bulk modulus. Therefore, if dissipation of excess pore pressure is of interest, the *PostShake* flag should be activated with care.

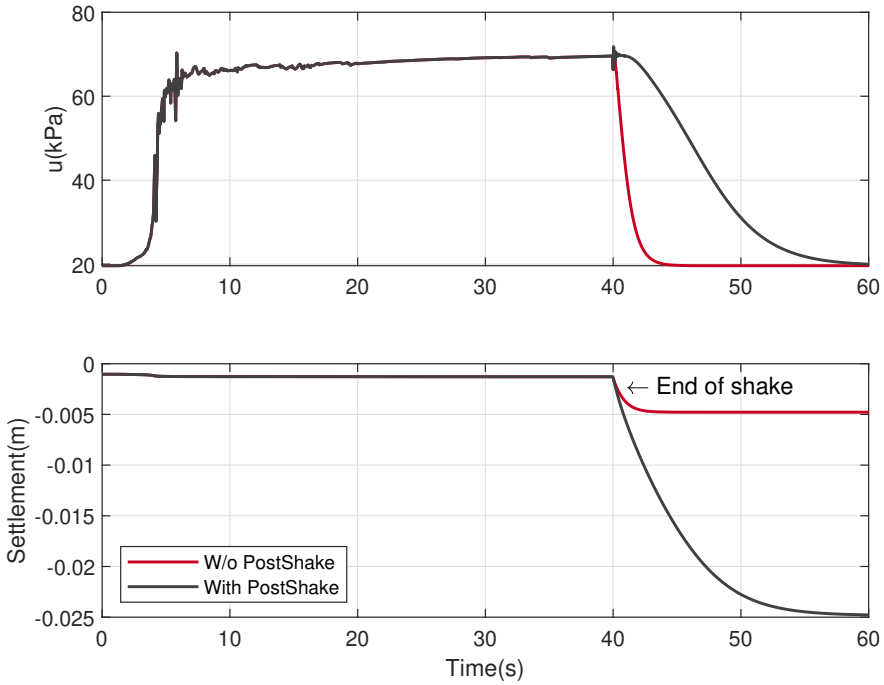

Figure 2.3: Comparison of excess pore pressure dissipation and settlement for cases with and without *PostShake* flag activated at the end of the main shake.

2.3 IMPLEMENTATION OF PM4SAND IN OPENSEES

2.3.1 Explicit Integration Schemes

The current implementation of PM4Sand in OpenSees includes three explicit integration schemes: Forward Euler, Modified (or two-step) Euler with sub-stepping and 4^{th}-order explicit Runge-Kutta method. During each strain sub-increment, an algorithm is used that accounts for the transition from elastic to elasto-plastic states (yield surface intersection) and correction of stresses to the yield surface (yield surface drift), respectively. Details on explicit schemes are presented by Sloan et al. (2001). Readers are encouraged to refer to the original paper by Sloan for more details; the basic steps are presented here.

Yield Surface Intersection

At the beginning of each step, an elastic trial stress increment $\dot{\boldsymbol{\sigma}}_e$ is calculated using the strain increments $\dot{\boldsymbol{\epsilon}}$,

$$\dot{\boldsymbol{\sigma}}_e = \mathbb{C}_e : \dot{\boldsymbol{\epsilon}}\,, \tag{2.74}$$

where the stress–strain matrix $\mathbb{C}_e$ can be replaced by the secant elastic stiffness matrix $\overline{\mathbb{C}_e}$, defined in terms of the secant shear modulus G and bulk modulus K evaluated using the previous stress state, $\boldsymbol{\sigma}_0$, and total volumetric strain increment. The previous equation can be replaced by,

$$\dot{\boldsymbol{\sigma}}_e = \overline{\mathbb{C}_e}(K,G)\dot{\boldsymbol{\epsilon}} = \overline{\mathbb{C}_e}(\boldsymbol{\sigma}_0, \mathbb{C}_e\epsilon_v)\dot{\boldsymbol{\epsilon}} = \overline{\mathbb{C}_e}\dot{\boldsymbol{\epsilon}}\,. \tag{2.75}$$

The elastic trial stress increment is used in the formulation to check if the stress state has changed from elastic to elasto-plastic. Such a change occurs if $f(\boldsymbol{\sigma}_0, \boldsymbol{\alpha}) < 0$ and $f(\boldsymbol{\sigma}_0 + \dot{\boldsymbol{\sigma}}_e, \boldsymbol{\alpha}) > 0$. If this occurs, then it is necessary to check the fraction of $\dot{\boldsymbol{\epsilon}}$ that moves the stress state from $\boldsymbol{\sigma}_0$ to the stress state on the yield surface. The exact yield condition $f(\boldsymbol{\sigma}_0, \boldsymbol{\alpha}) = 0$ can be replaced by $|f(\boldsymbol{\sigma}_0, \boldsymbol{\alpha})| \leq FTOL$, where $FTOL$ has a small positive tolerance. This minimizes the effect of finite precision arithmetic and modifies the transition condition to $f(\boldsymbol{\sigma}_0, \boldsymbol{\alpha}) < -FTOL$ and $f(\boldsymbol{\sigma}_0 + \dot{\boldsymbol{\sigma}}_e, \boldsymbol{\alpha}) > FTOL$. Sloan et al. (2001) recommends suitable values for $FTOL$ in the range of 10^{-6} to 10^{-9}. 10^{-8} is set as the default value in the current OpenSees implementation. The problem of finding the stresses at the yield surface intersection point is equivalent to finding the scalar quantity elastic ratio e that satisfies the nonlinear equation,

$$f(\boldsymbol{\sigma}_0 + e\dot{\boldsymbol{\sigma}}_e, \boldsymbol{\alpha}) = 0\,, \tag{2.76}$$

where $0 \leq e \leq 1$, and a value of 1 indicates purely elastic deformation; a value of 0 indicates purely elasto-plastic deformation. The Pegasus procedure of Dowell and Jarratt (1972) was implemented in this work to find the value of e.

Correction of Stresses to Yield Surface

In the explicit integration process, at the end of each sub-increment the stresses may diverge from the yield condition such that $f(\boldsymbol{\sigma}_0, \boldsymbol{\alpha}) > FTOL$. This violation is commonly known as

yield surface drift and varies with the accuracy of the integration scheme and the nonlinearity of the constitutive relations. The nonlinearity of the PM4Sand constitutive relations leads to a small drift at each integration sub-step. This drift is cumulative and can cause model instability. Therefore, it is imperative to impose a yield surface correction at the end of each sub-increment. Potts and Gens (1985) examined five methods for accounting for this drift. These involve correcting the stresses by projecting back along the plastic flow, the total strain increment, or the accumulated effective stress direction. In addition, Potts and Gens demonstrated that a consistent correction method that preserves the total strain increment during the correction step, known as a consistent correction, is both effective and successful. Under certain conditions, however, the corrected stress state is further from the yield surface than the uncorrected stress state, and the consistent correction may not converge. In these cases, the consistent return scheme may be abandoned for one iteration and replaced with a correction that is normal to the yield surface as the algorithm by Sloan et al. (2001). This correction is applied iteratively until $f(\boldsymbol{\sigma}_0, \boldsymbol{\alpha}) \leq FTOL$.

Forward Euler

A first-order forward Euler method was first used in the implementation of PM4Sand. This method is the most basic approximation method for the integration of ordinary differential equations of the form,

$$\dot{u} = u' = \frac{du}{dx} = f(x, u) \quad u(0) = u_0 \,. \tag{2.77}$$

Using Taylor's expansion, and neglecting $O(h^2)$ and higher terms,

$$\frac{u^{n+1} - u^n}{h} \approx f(x^n, u^n) \,. \tag{2.78}$$

resulting in a simple explicit approximation of the form,

$$u^{n+1} = u^n + hf(x^n, u^n) \,. \tag{2.79}$$

Although simple and straightforward, the forward Euler method is first-order accurate and can be unstable. Hence when choosing a forward Euler as the integration scheme, the time step should be carefully selected, and a maximum strain increment scheme might need to be considered.

Modified Euler with Sub-Stepping

A modified Euler scheme with sub-stepping as proposed in Sloan et al. (2001) was used in the implementation of PM4Sand in OpenSees to overcome the drawbacks of the forward Euler method. In this method, first a forward Euler step is calculated over half the time step and the differential function is evaluated at the resulting point. Then, this differential is used to calculate the next step in the solution.

- First Step (forward Euler): $\hat{u}^{n+\frac{1}{2}} = u^n + \frac{h}{2} f(u^n)$.
- Second Step: $u^{n+1} = u^n + h f(\hat{u}^{n+\frac{1}{2}})$.

A local error measurement is introduced by automatically subdividing the imposed strain increment. During each sub-increment, the local error is found by taking the difference between stress solutions of a second-order modified Euler and a first-order accurate Euler. Once the local error has been computed for a given step, the size of the next step is determined using,

$$\begin{aligned} &\Delta h^{k+1} = q \Delta h^k \,, \\ &q = min\{0.9\sqrt{STOL/R_{h^k + \Delta h^{n+1}}}, 1.1\} \,, \end{aligned} \tag{2.80}$$

and h is a pseudo strain or pseudo time.

4th-Order Runge-Kutta

A classical 4^{th}-order explicit Runge-Kutta method was also used in the implementation of PM4Sand in OpenSees. This method is reasonably simple and robust, and is a good general candidate for numerical solution of differential equations. This method can also be paired with automatic error control with adaptive step-size routine for future work. The currently implemented four stages of this method are summarized below:

1. $\hat{u}^{n+\frac{1}{2}} = u^n + \frac{h}{2} f(u^n)$,
2. $\tilde{u}^{n+\frac{1}{2}} = u^n + \frac{h}{2} f(\hat{u}^{n+\frac{1}{2}})$,
3. $\tilde{u}^{n} = u^n + h f(\tilde{u}^{n+\frac{1}{2}})$,
4. $u^{n+1} = u^n + \frac{h}{6}(f(u^n) + 2\hat{u}^{n+\frac{1}{2}} + 2f(\tilde{u}^{n+\frac{1}{2}}) + f(\tilde{u}^n))$.

Maximum Strain Increments

A scheme to control the maximum strain increment that is sent to any of the Euler methods was also implemented in OpenSees. This method can be coupled with either one of the two Euler integration methods presented earlier. This scheme checks the trial strain parsed to the integrator and subdivides it if a certain maximum strain increment is exceeded. In the current implementation, the maximum strain increment is set to be 10^{-6}.

The default and recommended integration scheme in the current implementation is the modified Euler method that has also been optimized for performance. Nevertheless, the user is also able to switch to a different scheme by changing an input parameter at the time of material creation or using the built-in *setParameter* command during the analysis.

2.3.2 Tcl Commands

OpenSees has both Tcl and Python interpreters for model building. Only commands using Tcl interpreter are discussed here. Information on the Python interpreter can be found at `https://openseespydoc.readthedocs.io/en/latest/`. In the current OpenSees implementation, the PM4Sand material can be created using the following Tcl command,

```
nDmaterial PM4Sand $matTag $Dr $Go $hpo $Den <$patm $h0 $emax $emin $nb \\
$nd $Ado $zmax $cz $ce $phic $nu $cgd $cdr $ckaf $Q $R $m $Fsed_min $p_sedo>
```

where *matTag* is an integer tag identifying the material. The material parameters discussed earlier is the other input. Secondary parameters are inside <> and are optional.

The integration scheme can be updated using the *setParameter* command:

```
setParameter -value $mScheme -eleRange $eleStart $eleEnd IntegrationScheme $matNum
```

where *mScheme* is an integer related to each integration scheme as shown below:

- *mScheme* = **1**: Modified Euler with automatic substepping.
- *mScheme* = **2**: Forward Euler.
- *mScheme* = **3**: 4th-Order Runge-Kutta.
- *mScheme* = **4**: Forward Euler with manual maximum strain increment.
- *mScheme* = **5**: Modified Euler with manual maximum strain increment.

The *PostShake* flag can be activated in OpenSees using:

```
setParameter -value 0 -eleRange $eleStart $eleEnd PostShake $matNum
setParameter -value 0 -ele $eleNum PostShake $matNum
```

where *$eleStart* and *$eleEnd* define the range of elements that activate the *PostShake*, and *$matNum* is the material tag assigned to the elements.

2.4 PARAMETRIC STUDY ON CALIBRATION OF PM4SAND

The calibration procedure for PM4Sand is straight forward for general sand-like behavior as intended by the model developers. When detailed laboratory tests results are available, the apparent relative density D_R can be estimated using void ratio and measured e_{max} and e_{min}. As discussed in Boulanger and Ziotopoulou (2017), however, D_R is defined to bound the model response rather than a strict measured of relative density from maximum and minimum density tests. Therefore, the user can adjust its value as part of the calibration process, and it might be necessary to re-position the default critical state line by adjusting secondary parameters Q and R. Nevertheless, the estimated D_R provides a reasonable value, such that the resulting model response is also reasonable. G_o can be estimated using small-strain shear modulus estimation methods for different confining pressures. Once D_R and G_o are determined, h_{po} can be calibrated iteratively by the following: (1) matching the

excess pore pressure evolution for a range of individual laboratory tests; and/or (2) matching specific values of CRR. Additional secondary parameters can also be adjusted to fine tune the model response. For example, adjusting h_o can result in different modulus reduction curves.

On the other hand, when comprehensive laboratory tests are not available for specific sites, model calibration needs to be based on *in situ* test data, such as SPT blow count, CPT penetration resistance, or shear-wave velocity (V_s). For example, D_R can be estimated by correlations to penetration resistances. Idriss and Boulanger (2008) recommended the following correlation to SPT,

$$D_R = \sqrt{\frac{(N_1)_{60}}{C_d}}\,, \tag{2.81}$$

where C_d is recommended to be 46. For CPT, the following correlation can be used,

$$D_R = 0.465\Big(\frac{q_{c1N}}{C_{dq}}\Big)^{0.264} - 1.063\,, \tag{2.82}$$

where C_{dq} is recommended to be 0.9. The second primary input parameter G_o can also be estimated from *in situ* data. Boulanger and Ziotopoulou (2017) modified the correlation by Andrus and Stokoe (2000) to constraint the extrapolation to very small $(N_1)_{60}$ values, as

$$V_{s1} = 85[(N_1)_{60} + 2.5]^{0.25}\,. \tag{2.83}$$

Alternatively, a simpler expression can be used when combined with a range of typical densities as,

$$G_o = 167\sqrt{(N_1)_{60} + 2.5}\,. \tag{2.84}$$

Subsequently, h_{po} can be calibrated to reproduce a specific value of CRR that can be computed using liquefaction triggering models. Numerous liquefaction triggering models incorporating the simplified cyclic stress approach have been proposed in the past by Youd and Idriss (2001), Cetin et al. (2004), and Idriss and Boulanger (2008).

Once D_R, G_o, and CRR are chosen, the modeler should iteratively vary the value of h_{po} until the simulated CRR matches the targeted value. Interpolation and extrapolation are common when the variables are within or close to the range of existing calibrated sets of parameters. Secondary parameters are less common to be modified when only *insitu* data are available. This calibration process can become cumbersome when *insitu* data show a large degree of variability and calibration has to be performed for each soil unit.

To simplify the calibration process under these circumstances, a parametric study was conducted to establish a correlation among D_R, G_o, h_{po}, and CRR, i.e., $CRR = f(D_R, G_o, h_{po})$. The function, f, should be solvable for h_{po} when the other variables are known and eventually yield $h_{po} = g(CRR, D_R, G_o)$. This correlation is intended to provide a preliminary estimation of h_{po} and simplify the iterative calibration process under selected D_R, G_o, and CRR, especially when both SPT and V_s data are available and the user wants to make G_o independent to D_R.

For this purpose, the Dakota (Adams et al., 2017) platform, run through the uqFEM [McKenna et al. (2018), now quoFEM] tool developed by the NHERI SimCenter, was used in this parametric study. The Dakota software provides advanced parametric analysis techniques enabling quantification of margins and uncertainty, risk analysis, model calibration, and design exploration with computational models. Its methods include optimization, uncertainty quantification, parameter estimation, and sensitivity analysis, which may be used individually or as components within surrogate-based and other advanced strategies. The uqFEM application is intended to advance the use of uncertainty quantification and optimization within the field of natural hazards engineering by combining existing finite-element applications, e.g., OpenSees, with uncertainty quantification applications, i.e., Dakota, behind a simple user interface. In this study, uqFEM was modified to include our MixedDriver tool and all the simulations were performed on the Texas Advanced Computing Center (`http://www.tacc.utexas.edu`) Stampede2 supercomputer made available through DesignSafe-ci (Rathje et al., 2017).

Using this tool, D_R, G_o, and h_{po} were varied while all the secondary parameters retained their default values (predifined by primary paramters and initial stresses). The Latin Hypercube Sampling (LHS) method was used to generate near-random variables. Each of these three variables was assigned an independent uniform distribution between minimum and maximum values. The range of these variables was chosen to cover a reasonable range of scenarios and can be extended in future studies. D_R was set to be between 0.2 to 0.9, G_o between 250 to 1200, and h_{po} between 0.05 to 1.2. A total of one million samples were generated. For each set of parameters, Dakota ran MixedDriver to simulate undrained cyclic simple shear tests for 15 different $CSRs$ ranging from 0.05 to 0.8 to produce smooth cyclic strength curves; see Figure 2.6.

A total of three initial conditions were considered: initial effective vertical stress $\sigma'_v = 1\ atm.$ with K_0 equal to 0.5 and 1.0, respectively, and $\sigma'_v = 2\ atm.$ with K_0 equal to 0.5. The analyses were capped at 350 uniform cycles. Once all 15 simulated CDSS tests were done, a python script was called by Dakota to calculate the number of cycles to reach liquefaction; which was defined as the number of cycles required to reach a single amplitude (SA) shear strain of 3%, as recommended by Ishihara (1993). The number of cycles to reach 1% and 2% SA and the slope (-b) and intercept (a) of the CSR curves (Idriss and Boulanger, 2008) in logarithmic scale were also recorded. The number of cycles were rounded up to the nearest half. Then a cyclic strength curve was interpolated to calculate the Cyclic Resistance Ratio, CRR, which was determined as the CSR corresponding to 15 cycles. The CRRs were bounded between 0.05 and 0.5 for interpolation accuracy. A sample of the the Dakota input file is shown below:

```
environment
tabular_data
tabular_data_file = 'dakotaTab.out'

method,
sampling
sample_type = lhs
samples = 1000000
seed = 215

variables,
```

```
uniform_uncertain = 3
lower_bounds = 0.2  200  0.05
upper_bounds = 0.95  1200  1.2
descriptors = 'dr'  'Go'  'hpo'

uncertain_correlation_matrix = 1.00000  0.00000  0.00000
                               0.00000  1.00000  0.00000
                               0.00000  0.00000  1.00000

interface,
fork
 asynchronous
analysis_driver = 'fem_driver'
parameters_file = 'params.in'
failure_capture = recover -1
results_file = 'results.out'
work_directory directory_tag
copy_files = 'templatedir/*'
named 'workdir'
aprepro

responses,
response_functions = 4
response_descriptors = 'a'
'b'
'crr'
'crr2'
'crr3'
no_gradients
no_hessians
```

Figure 2.4 illustrates the histograms of all three input variables, D_R, G_o, and h_{po}, and one of the outputs, i.e., $CRR_{3\%}$ for the case with $K_0 = 0.5$ and $\sigma'_v = 1\ atm.$. The input variable histograms generally show the predefined uniform distribution pattern, while the attained CRR histogram shows values concentrated near lower values, indicating a higher CRR, such as 0.6, is highly unlikely using the current range of input parameters. A small portion of the samples were discarded because not enough points were obtained to form a smooth $CSR - N$ curve, i.e., these sets of parameters produced 3% SA either under one cycle or beyond 350 cycles for a wide range of CSRs. This resulted in a slight reduction in the valid sample size from 1M to about 990k. Figure 2.5 presents the pair-wise relationships between each of the three input parameters and the $CRR_{3\%}$ for the same case. Positive correlations are shown in all three plots with more significant correlation evident between D_R and $CRR_{3\%}$.

Table 2.1 presents partial rank correlation values between all inputs and outputs, with larger values indicating greater correlation between input and output. The results echo the trend shown in Figure 2.5, with both D_R and h_{po} having stronger influence on CRR as compared to G_o. This phenomenon echos PM4Sand's dependency on D_R, which controls the state parameter and several other secondary parameters (including fabric), and h_{po}, which controls the rate of pore pressure accumulation during contraction. G_o has a stronger effect on CRR for larger strain criteria, i.e., 0.44 for 3% vs. 0.25 for 1%.

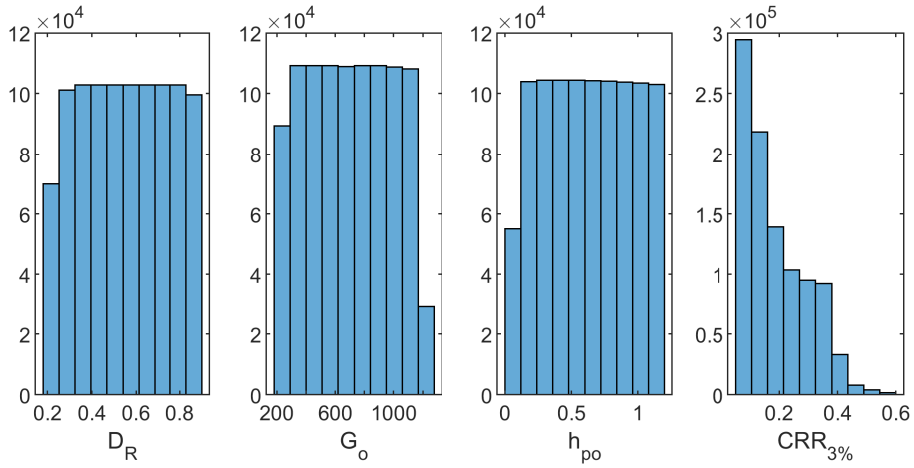

Figure 2.4: Pair-wise relationships between all inputs parameters and $CRR_{3\%}$, $K_0 = 0.5\,, and \sigma'_v = 1\ atm.$.

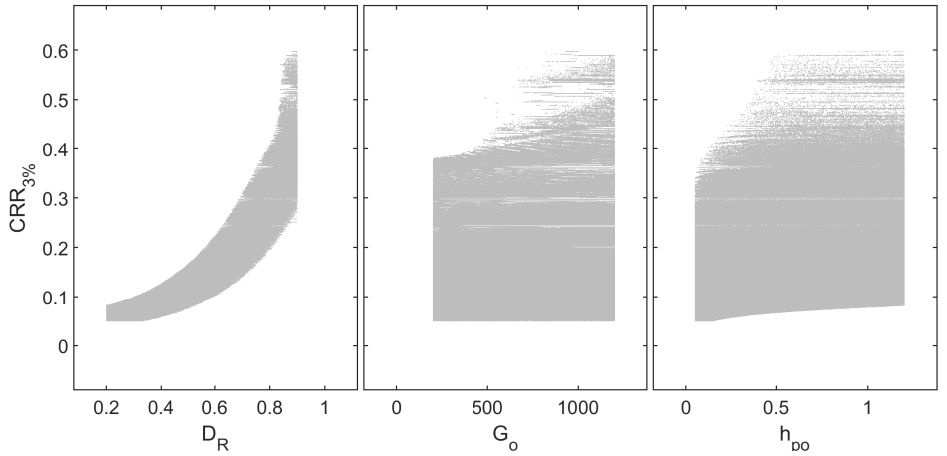

Figure 2.5: Pair-wise relationships between all the inputs and $CRR_{3\%}$, $K_0 = 0.5\,, and \sigma'_v = 1\ atm.$.

Table 2.1: Partial rank correlation matrix between inputs and outputs for $K_0 = 0.5, \sigma'_v = 1\ atm.$

	$CRR_{1\%}$	$CRR_{2\%}$	$CRR_{3\%}$
D_R	0.990279	0.992808	0.993168
G_o	0.247524	0.308400	0.441622
h_{po}	0.879294	0.903305	0.901287

The results were processed through a linear regression analysis using *Matlab* to find the correlation between the input, D_R, h_{po}, and G_o, and the output CRR. Different combination of terms were explored and the following format produced the largest R^2,

$$\begin{aligned} CRR_{3\%,K_0=0.5} =& 0.1282 - 0.4952 D_R - 5.0565 \times 10^{-5} G_o + 0.0749 h_{po} + 1.4665 \times 10^{-4} D_R G_o \\ &+ 0.1323 D_R h_{po} + 0.7252 D_R^2 - 0.0636 h_{po}^2 \,, \end{aligned} \tag{2.85}$$

with $R^2 = 0.989$. In this equation, D_R is in fractions. CRRs using criteria of 1% and 2% SA as well as for other σ'_v and K_0 were also analyzed. All the estimated coefficients are summarized in Tables 2.2 and 2.3. Note: the magnitude of these coefficients depends directly on the scale of the selected variables; smaller coefficients don't necessary imply less important features. For example, G_o is approximately three orders of magnitude larger than D_R, leading to much smaller coefficients.

Table 2.2: Summary of estimated regression coefficients.

	$\sigma'_v = 1$ *atm.*, $K_0 = 0.5$			$\sigma'_v = 1$ *atm.*, $K_0 = 1.0$		
	3%	2%	1%	3%	2%	1%
Intercept	0.1282	0.1127	0.1113	0.1262	0.1254	0.1279
D_R	-0.4952	-0.4437	-0.4186	-0.5038	-0.5002	-0.4727
G_o	-5.057×10^{-5}	-3.496×10^{-5}	-4.856×10^{-5}	-3.727×10^{-5}	-2.977×10^{-5}	-5.697×10^{-5}
h_{po}	0.07487	0.07790	0.08578	0.1090	0.1061	0.1163
$D_R G_o$	1.466×10^{-4}	9.953×10^{-5}	1.264×10^{-4}	1.148×10^{-4}	8.703×10^{-5}	1.491×10^{-4}
$D_R h_{po}$	0.1323	0.1282	0.1135	0.1483	0.1547	0.1301
D_R^2	0.7252	0.6962	0.6463	0.8485	0.8486	0.7729
h_{po}^2	-0.06362	-0.06437	-0.06568	-0.08380	-0.08349	-0.08379
R^2	0.989	0.993	0.987	0.995	0.995	0.987

Table 2.3: Summary of estimated regression coefficients (continued).

	$\sigma'_v = 2$ *atm.*, $K_0 = 0.5$		
	3%	2%	1%
Intercept	0.8540	0.8585	0.9228
D_R	-0.2928	-0.2942	-0.3060
G_o	-1.608×10^{-5}	-1.428×10^{-5}	-2.287×10^{-5}
h_{po}	0.02590	0.02587	0.02548
$D_R G_o$	5.285×10^{-5}	4.492×10^{-5}	6.921×10^{-5}
$D_R h_{po}$	0.03721	0.03748	0.03641
D_R^2	0.5971	0.5969	0.5807
h_{po}^2	-0.005031	-0.005042	-0.004916
R^2	0.990	0.989	0.987

Several visual-manual calibration studies presented in Chapter 3 and available in Boulanger and Ziotopoulou (2017) were revisited to evaluate the accuracy of the proposed correlation. These calibrations were done using the same initial conditions as in this study, and the 3% SA criterion was used. Table 2.4 compares these results. As shown in the table, the predicted CRRs fall within a 5% range of the targeted CRRs. The correlation obtained from the regression showed good agreement with the calibrations.

Equation (2.85) can be rearranged to isolate h_{po},

$$ah_{po}^2 + bh_{po} + c = 0\,, \tag{2.86}$$

where $a = 0.0636$; $b = -0.0749 - 0.1323D_R$; and $c = -0.1282 + 0.4952D_R + 5.0565 \times 10^{-5}G_o - 1.4665 \times 10^{-4}D_RG_o - 0.7252D_R^2 + CRR_{3\%,K_0=0.5}$. This correlation becomes a quadratic equation for h_{po} that can be solved for two real roots for h_{po} when values of D_R, G_o, and CRR are given. The lesser root is the one that can be paired with D_R and G_o to yield the desired CRR in a calibration process. Using this equation, h_{po} values were calculated and compared with those obtained using the visual-manual calibration process. Table 2.5 summarizes these results. The observed error in h_{po} was larger than that observed in CRRs, especially for higher D_Rs, e.g., 0.75. However, no significant discrepancy was observed in the comparison of CSR-N curves obtained using the visual-manual calibrated and predicted h_{po}'s; see Figure 2.6.

Two aspects should be considered: (1) the CRR obtained using PM4Sand is more sensitive to D_R—especially under higher D_Rs—thus a wider range of h_{po} can produce similar CRRs under these conditions; and (2) the CRR obtained using a visual-manual calibration process is usually estimated using fewer number of points to form the CSR-N curve, thus larger uncertainty occurs for h_{po} at a given combination of CSR and N. Nevertheless, the results demonstrate the predictive equation can be used to provide good initial h_{po} values and accelerate the calibration process.

Table 2.4: Comparison of predicted and targeted $CRR_{3\%}$.

N	D_R	G_o	h_{po}	CRR(Targeted)	CRR(Predicted)	error
5	0.330	354.0	0.533	0.086	0.088	2.2%
10	0.466	468.3	0.463	0.118	0.113	4.4%
20	0.659	651.0	0.425	0.206	0.207	0.7%
5*	0.35	476.0	0.53	0.090	0.090	0.8%
14*	0.55	677.0	0.40	0.148	0.144	2.3%
26*	0.75	890.0	0.63	0.312	0.302	4.4%

*From Boulanger and Ziotopoulou (2017)

Nonetheless, limitations exist in the predictive equation as real roots are not guaranteed for this quadratic equation under all combinations of D_R, G_o, and CRR, e.g., when D_R, G_o, and CRR exceed the range of parameters considered, and when the resulting h_{po} is either larger than 1.2 or smaller than 0.05 depending on the CRR. Under these circumstances, manual calibration is required.

Figure 2.7 shows all CRR (3%) calculated in this study plotted along with curves from empirical triggering models, where simulation $(N_1)_{60}$ was back-calculated from D_R using $C_d = 46$. Each simulation data point represents a unique combination of D_R, G_o, and h_{po}. The data are bounded by h_{po} under a given D_R as CRR is less sensitive to G_o (Table 2.1). The simulation data on the upper part of the plot correspond to h_{po} close to 1.2, while the

Table 2.5: Comparison of predicted and targeted h_{po}.

N	D_R	G_o	CRR (Targeted)	h_{po} (Visual-Manual calibration)	h_{po}(Predicted)	error
5	0.330	354	0.086	0.533	0.497	6.7%
10	0.466	468.3	0.118	0.463	0.534	15.4%
20	0.659	651	0.206	0.425	0.439	3.2%
5*	0.35	476	0.090	0.53	0.516	2.6%
14*	0.55	677	0.147	0.40	0.427	2.2%
26*	0.75	890	0.312	0.63	0.745	18.3%

*From Boulanger and Ziotopoulou (2017)

data on lower part of the plot correspond to h_{po} close to 0.05. This figure shows that the general trend obtained from the simulation follows the empirical models closely—especially the model by Idriss and Boulanger (2008)—between approximately $(N_1)_{60}$ of 5 and 25. For higher $(N_1)_{60}$, both empirical models and the simulations show greater uncertainty. The maximum h_{po} value selected in this parametric study was not large enough to cover CRR for higher D_R $[(N_1)_{60}]$.

Based on this observation, a series of additional simulations were performed using the constant h_{po}, ranging from 0.05 to 3.0, as shown in Figure 2.8. Each additional h_{po} case represented 250k cases, with all the other inputs remaining the same as in the previous study. The scatter plot shown in Figure 2.8 illustrates all obtained CRR for each constant h_{po}; these are shown in different colors. A series of polynomials were then fitted through the data points to show the general trend between D_R and CRR for each h_{po}. These curves can be interpolated to provide an initial estimation of h_{po} for a given D_R.

The relationship between the CRR and N, within the range of cycles of interest for earthquake engineering, can generally be approximated with a power function as,

$$CRR = a \cdot N^{-b}\,, \tag{2.87}$$

where the parameters a and b are determined by regression against the simulated data. The parameter b for clean sands is typically about 0.34, whereas the parameter a depends on a wide range of factors. As shown in Figure 2.9a, for relatively loose sand, i.e., D_R ranging from 0.2 to 0.6, the slope b is unlikely to go below 0.3 with changing primary parameters. Note, laboratory tests conducted on Ottawa F-65 sand have shown a b value of 0.08 ($D_R = 20\%$) and 0.11 ($D_R = 70\%$) using undrained simple shear tests (Bastidas, 2016). In this case, modifying only primary parameters is inadequate in reproducing the behavior observed in laboratory tests, and changing secondary parameters becomes necessary.

Although the correlation proposed in this study can be used to calculate h_{po} automatically, it is only intended to provide a preliminary estimation. The stress–strain behavior attained with the model should always be examined against general soil behavior.

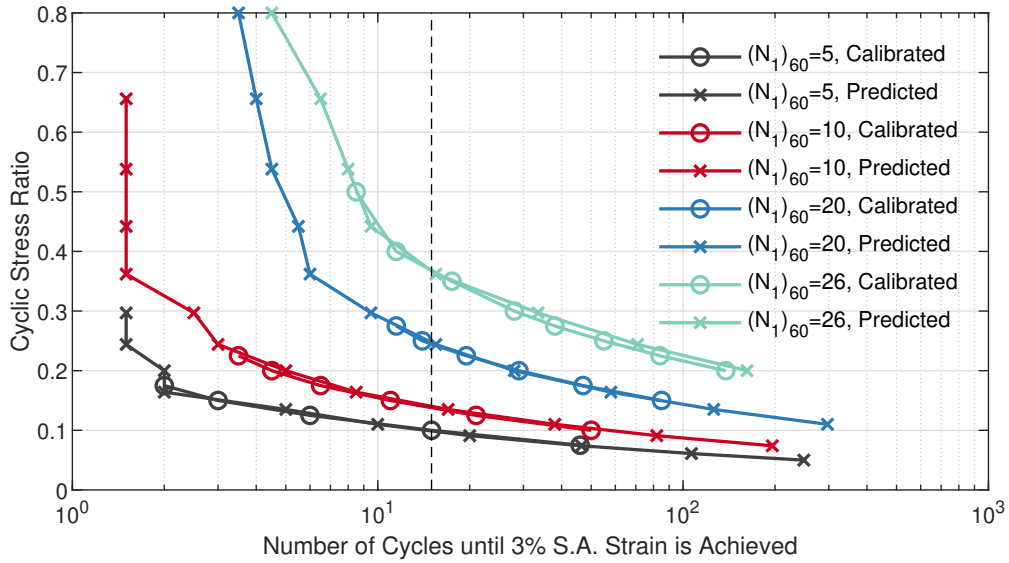

Figure 2.6: Comparison of CSR-N curves using visual-manual calibrated and predicted h_{po}.

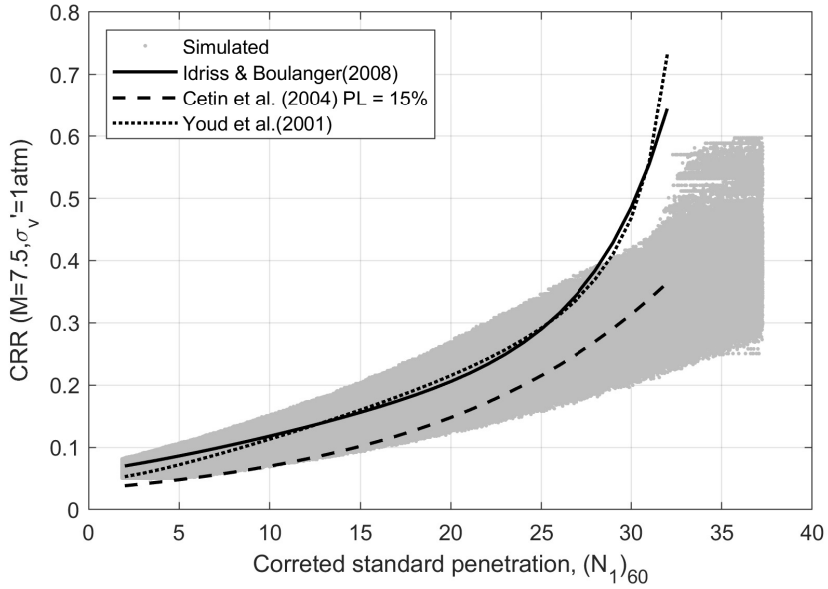

Figure 2.7: Comparison of CRR obtained using simulations with uniformly distributed h_{po} and using empirical models relating CRR to $(N_1)_{60}$ for clean sands with M = 7.5 and $\sigma'_{vc} = 1\ atm$..

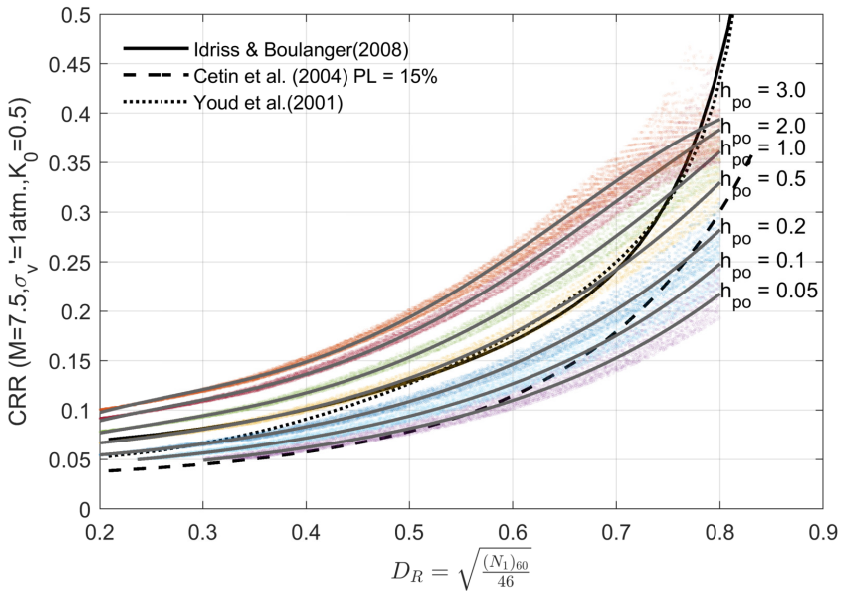

Figure 2.8: Comparison of CRR obtained using simulation with a series of constant h_{po} and using empirical models relating CRR to $(N_1)_{60}$ for clean sands with $M = 7.5$ and $\sigma'_{vc} = 1\ atm$.

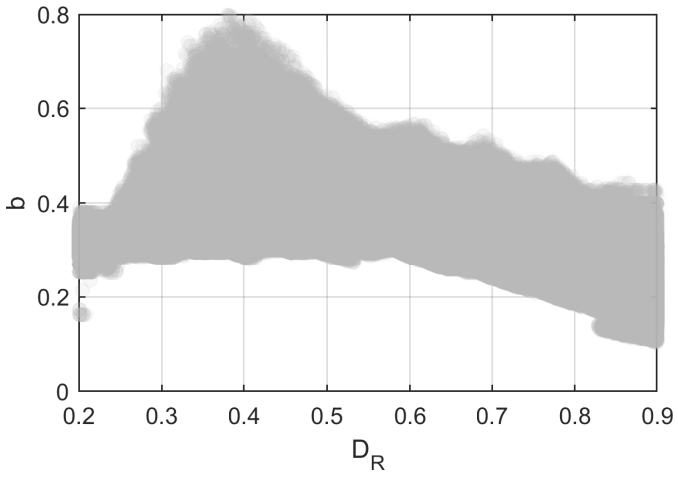

(a)

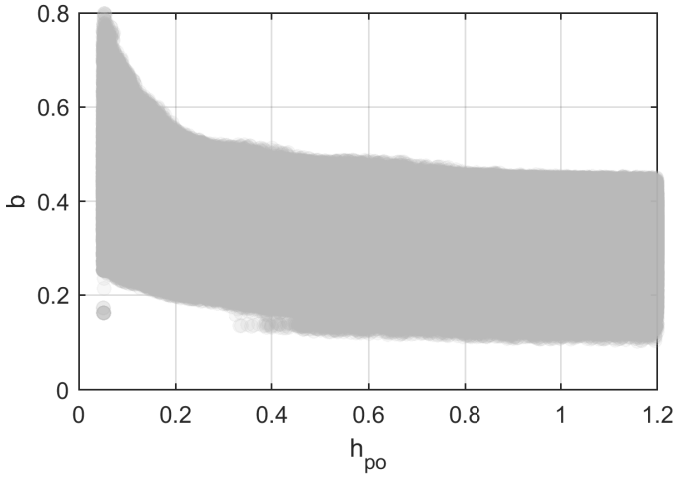

(b)

Figure 2.9: Correlation between the slope of CRR curves, b, and the primary parameters, D_R and h_{po}, respectively.

2.5 SUMMARY

This chapter presented a brief introduction to the PM4Sand model and a discussion on key formulation aspects. Implementation details, including stress correction strategies and integration schemes, were also presented, followed by a brief introduction to the OpenSees built-in commands considered in its implementation.

A parametric study was conducted to investigate PM4Sand's behavior under a large range of parameters. Despite limitations for representing dense sand behavior, a correlation was proposed that provides a reasonable estimation of h_{po} for a given combination of D_R, G_o, and CRR. This estimate can be used to speed up the calibration process when calibration has to be performed for each soil unit in a profile with large geological variability. The slope of the CRR curve, b, obtained using PM4Sand, was also presented and was shown to be representative for clean sands. However, undrained CDSS tests performed on Ottawa F-65 sand (Bastidas, 2016) showed b values that were less than what would be expected, indicating the limitation of calibrating only for primary parameters.

3 Verification of PM4Sand in OpenSees

3.1 INTRODUCTION

This chapter presents the results of a verification study of the PM4Sand model implemented in OpenSees. Verification is meant to identify and remove any programming errors and verify numerical algorithms. The goal of this verification phase was to ensure that OpenSees produced comparative results as the model's original implementation in FLAC. This proved challenging since comparisons involved responses obtained using different numerical tools and systems, i.e., between the finite-element method and finite-difference method. To address this issue, a series of stress point, single element, and 1D soil column analyses were considered such that system complexity was gradually increased, and the results were carefully examined to identify any inconsistencies.

3.2 VERIFICATION OF PM4SAND AT AN ELEMENT LEVEL

3.2.1 Point Level Simulations using MixedDriver

Verification of the OpenSees PM4Sand model was first performed using a constitutive driver based on the mixed control formulation proposed by Alawaji et al. (1992). This driver, refered to as the *MixedDriver* hereafter, uses a mixed control formulation designed to include all necessary OpenSees libraries; this way, the same model implemented in OpenSees can be tested in the driver. *Mixeddriver* gives the user full control of strain and/or stress loading under drained or undrained condition, thus representing a material point. In this context, it does not require definition of elements or boundary conditions as in standard OpenSees analyses. It is suitable for any verification study at the element level without bringing extra complexities related to the boundary value solution framework. Using this driver, a series of drained and undrained monotonic and cyclic tests for three different relative densities, namely 35%, 55%, and 75%, were simulated using PM4sand and the example parameters published in Boulanger and Ziotopoulou (2017). These parameters are summarized in Table 3.1. All FLAC results presented in this section were obtained using the FLAC example drivers provided by Boulanger and Ziotopoulou (2017) on `https://pm4sand.engr.ucdavis.edu/pm4sand-files/`. PM4Sand model version 3.1 compiled for FLAC 8.0 was used.

Table 3.1: PM4Sand parameters for verification cases.

$(N_1)_{60}$	V_{s1} using Andrus and Stokoe (2000)	$\text{CRR}_{M=7.5}$ using Idriss and Boulanger (2008)	D_R	G_o	h_{po}
6	144	0.090	0.35	476.0	0.53
14	171	0.147	0.55	677.0	0.40
26	196	0.312	0.75	890.0	0.63

*After Boulanger and Ziotopoulou (2017), all secondary input parameters were assigned default values.

Figure 3.1 compares the results using MixedDriver and the corresponding FLAC results for monotonic undrained tests under various initial consolidation pressures. In all these cases, the lateral pressure coefficient, K_0, was set to 1.0. The *MixedDriver* results matched well with FLAC results in terms of stress–strain behavior and change in pore pressure. Minor discrepancies were observed in post-peak softening for higher confining pressures (Figure 3.1a) and peak shear stress under sustained loading for a dense case (Figure 3.1c).

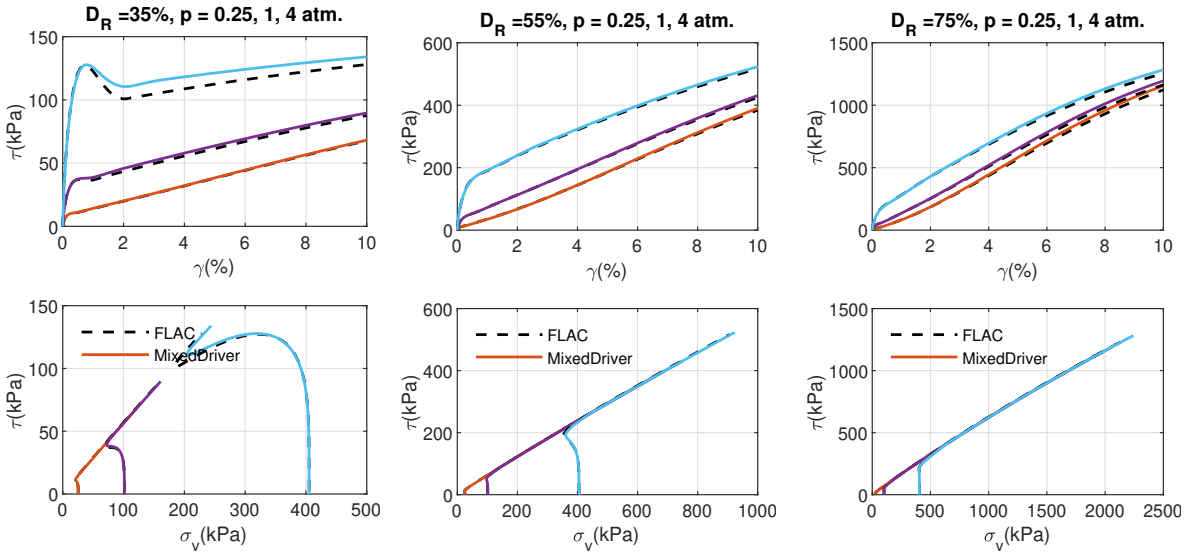

Figure 3.1: Comparison of responses obtained using *MixedDriver* (solid lines) and FLAC (dashed lines) for undrained monotonic DSS tests with (a) $D_R = 35\%$, (b) $D_R = 55\%$, and (c) $D_R = 75\%$ under various initial vertical stresses of $\sigma_v = 0.25$, 1, and $4\,atm.$, respectively, and $K_0 = 1.0$.

The same tests were repeated using an initial $K_0 = 0.5$, and the results are presented in Figure 3.2., where *MixedDriver* tends to over-predict the reduction in vertical effective stress, especially for loose cases (smaller relative density) under higher initial confining pressures; see Figure 3.2a. As shearing continues, the *MixedDriver* response tends to converge to the corresponding FLAC response. A detailed study was conducted to investigate the cause of this discrepancy. For this purpose, the strain history from FLAC was imported

into*MixedDriver* and internal parameters were compared with FLAC step by step to identify any possible discrepancy in the formulation and implementation. Although no errors were found, this discrepancy was narrowed down to be related to the method used for updating the back-stress ratio, $\boldsymbol{\alpha}$. As shown in Equation 2.33, the increment $\dot{\boldsymbol{\alpha}}$ is proportional to $\boldsymbol{\alpha}^b - \boldsymbol{\alpha}$. Under a simple shear-stress path, the loading direction, $\mathbf{n}$, written in vector form is,

$$\{\mathbf{n}\} = \begin{Bmatrix} 0 \\ 0 \\ \frac{\sqrt{2}}{2} \end{Bmatrix} . \tag{3.1}$$

Thus $\boldsymbol{\alpha}^b$ is in the form of,

$$\{\boldsymbol{\alpha}^b\} = \sqrt{1/2}[M^b - m]\{\mathbf{n}\} = \begin{Bmatrix} 0 \\ 0 \\ \alpha_{12}^b \end{Bmatrix} . \tag{3.2}$$

Assuming K_0 conditions with no initial static shear stress, the initial $\boldsymbol{\alpha}$ is,

$$\{\boldsymbol{\alpha}_o\} = \left\{\frac{\boldsymbol{\sigma} - p\mathbf{I}}{p}\right\} = \begin{Bmatrix} K_0\sigma_v \\ \sigma_v \\ 0 \end{Bmatrix} /p - \begin{Bmatrix} \frac{(K_0+1)\sigma_v}{2} \\ \frac{(K_0+1)\sigma_v}{2} \\ 0 \end{Bmatrix} /p = \begin{Bmatrix} \frac{(K_0-1)\sigma_v}{2} \\ \frac{(1-K_0)\sigma_v}{2} \\ 0 \end{Bmatrix} /p = \begin{Bmatrix} \frac{K_0-1}{K_0+1} \\ \frac{1-K_0}{K_0+1} \\ 0 \end{Bmatrix} , \tag{3.3}$$

where p is the mean effective stress. Recall that,

$$\dot{\boldsymbol{\alpha}} = \langle L \rangle \frac{2}{3} h(\boldsymbol{\alpha}_\sigma^b - \boldsymbol{\alpha}) . \tag{3.4}$$

Therefore, under a simple shear-stress path, $\boldsymbol{\alpha}$ will eventually converge to a state where $\alpha_{11} = \alpha_{22} = 0$ which is governed by $\boldsymbol{\alpha}^b$. The rate of this convergence was found to be related to the initial K_0. In FLAC's mixed discretization scheme, the zone-averaged stresses (consisting of four subzones) are used to compute a new dilatancy D and plastic modulus K_p that are consistent with the average response of the zone over a time step. These values for D and K_p are then used by all four subzones in the next time step, i.e., lagging one step. In OpenSees, however, the values of D and K_p are evaluated and used to update $\boldsymbol{\alpha}$ within the same step. The difference in calculated $\boldsymbol{\alpha}$ is cumulative and can lead to noticeable differences in the evolution of σ_v and σ_h at the beginning of loading when $K_0 \neq 0$. It can also lead to noticeable discrepancies in the pore pressure evolution under sustained loading, e.g., cyclic tests continued for multiple cycles.

Because PM4Sand was calibrated for general soil behavior using FLAC, it was preferable to apply a slight modification to the model formulation to capture the general response obtained using FLAC. In this case, matching the number of cycles to liquefaction instead of individual cycle's of pore pressure generation was emphasized. For this purpose, a parametric study was conducted to find out a reasonable implementation strategy to compensate for the faster pore pressure buildup. In this context, the term C_D in Equation (2.39), which is only for calibration purposes and not related to any physical quantity, was chosen and modified from 0.10 to 0.16 in the OpenSees implementation. All the results presented hereafter were obtained using this new value.

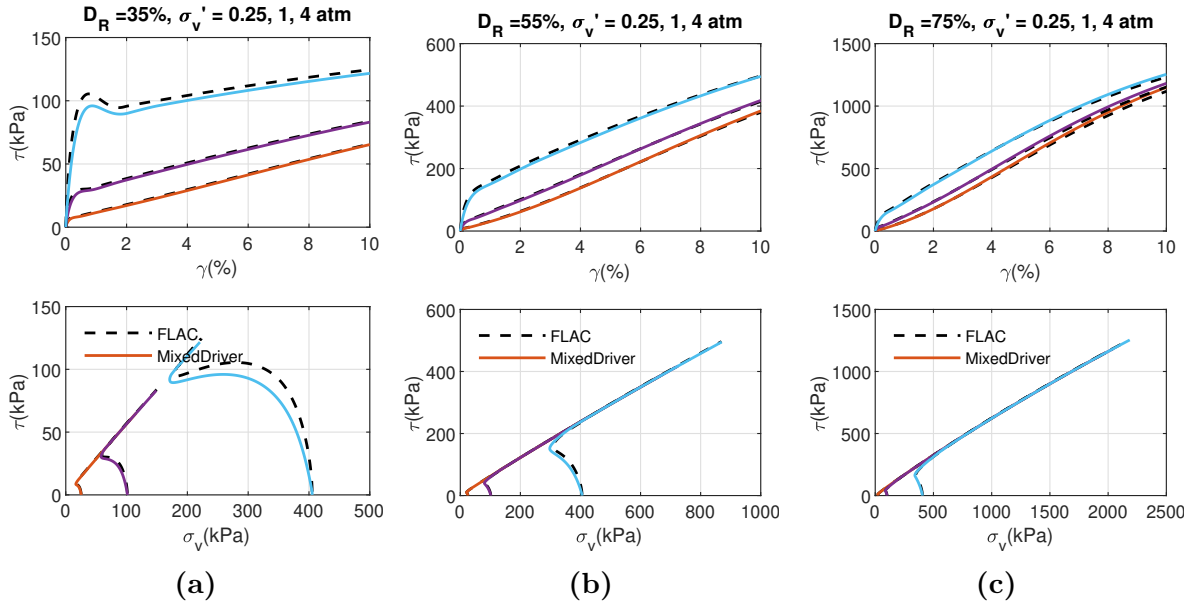

Figure 3.2: Comparison of responses obtained using *MixedDriver* (solid lines) and FLAC (dashed lines) for undrained monotonic DSS tests with (a) $D_R = 35\%$, (b) $D_R = 55\%$, and (c) $D_R = 75\%$ under various initial vertical stresses of $\sigma_v = 0.25$, 1, and $4\,atm.$, respectively, and $K_0 = 0.5$.

Figures 3.3 and 3.4 compare the results obtain using *MixedDriver* and corresponding FLAC results for cyclic direct simple shear (CDSS) tests using various D_Rs. The results show that the OpenSees implementation in *MixedDriver* captured the general trends produced by FLAC. The tests were repeated for different vertical consolidation stresses to show the effect of overburden pressure. A comparison between *MixedDriver* and FLAC results for cyclic stress ratios vs. number of uniform loading cycles is illustrated in Figure 3.5 and show good match. Figure 3.6 compares the overburden correction factor K_σ calculated using these simulations and the relationship recommended by Boulanger and Idriss (2004). The good agreement observed in the figure verifies the model's ability to capture the effect of confining stress at the stress point level.

The effect of initial static shear stress was also verified by simulations with various initial static shear stress ratios of 0.1, 0.2, and 0.3. These static shear stresses were applied during model initialization based on an effective vertical stress of 1 atm. Figure 3.7 compares the results obtained using *MixedDriver* and the corresponding FLAC results. The results are similar, indicating that the presence of an initial static shear stress results in lower cyclic strengths for loose sand and larger cyclic strengths for denser sands.

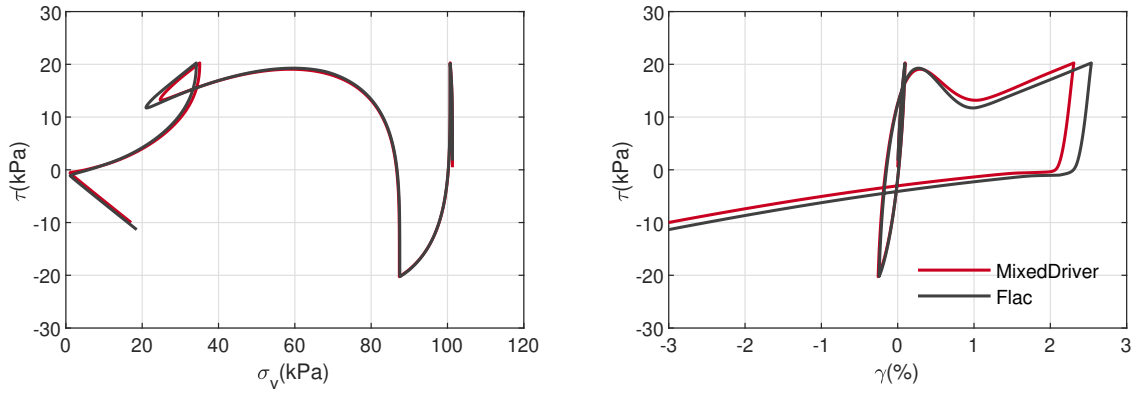

(a)

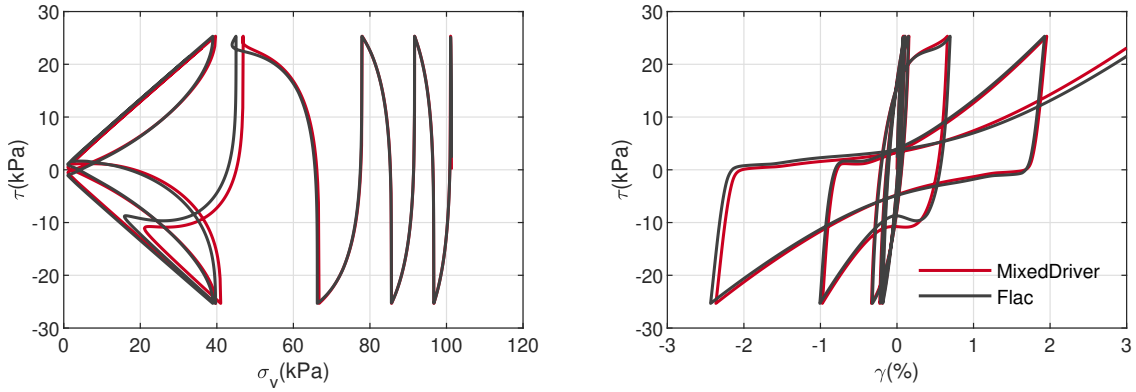

(b)

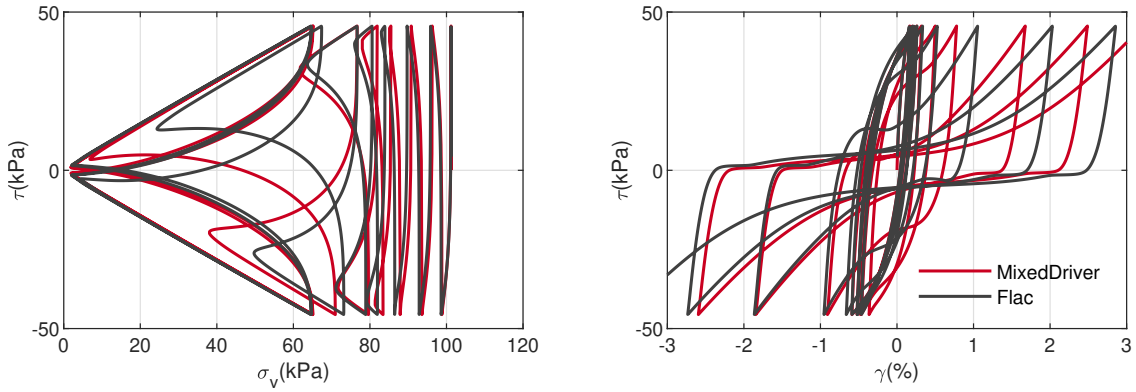

(c)

Figure 3.3: Comparison of results obtained using *MixedDriver* and FLAC for undrained CDSS tests for various D_Rs with an initial vertical stresses of 1 atm. and $K_0 = 1.0$; (a) $D_R = 35\%$, (b) $D_R = 55\%$, and (c) $D_R = 75\%$.

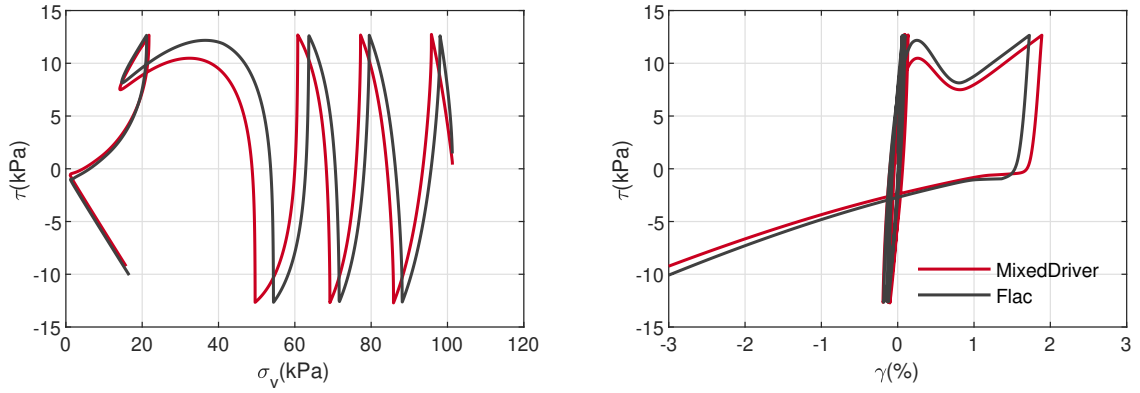

(a)

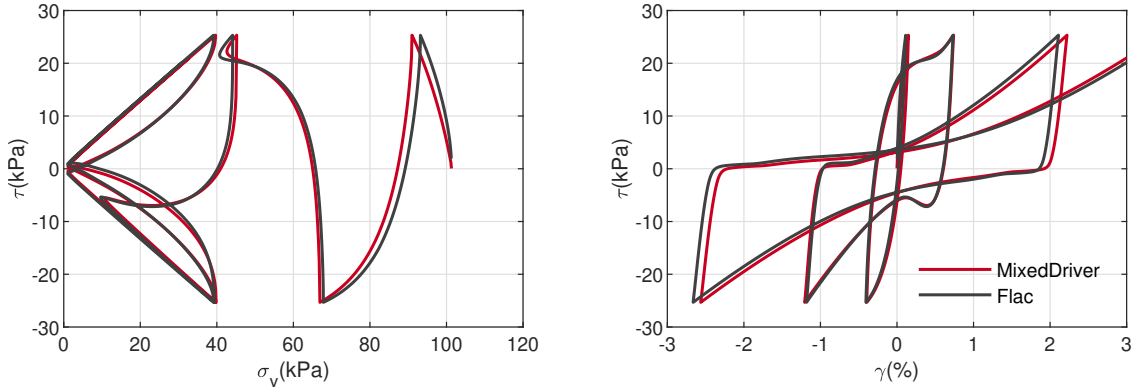

(b)

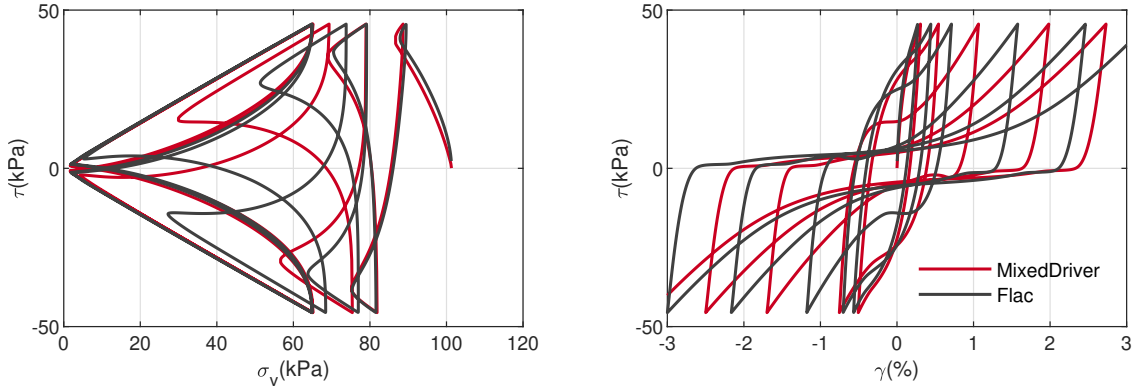

(c)

Figure 3.4: Comparison of results obtained using *MixedDriver* and FLAC for undrained CDSS tests for various D_Rs with an initial vertical stresses of 1 atm. and $K_0 = 0.5$; (a) $D_R = 35\%$, (b) $D_R = 55\%$, and (c) $D_R = 75\%$.

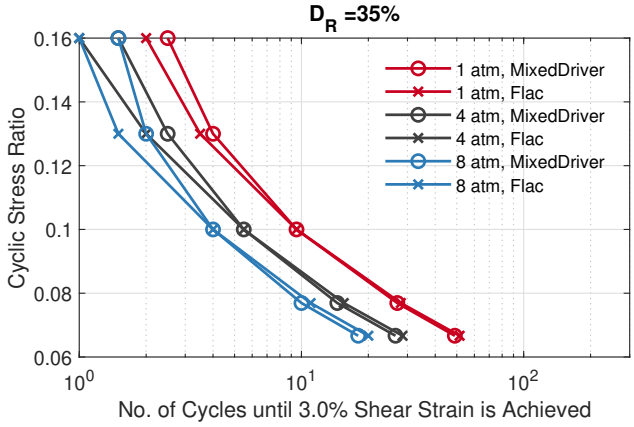

(a)

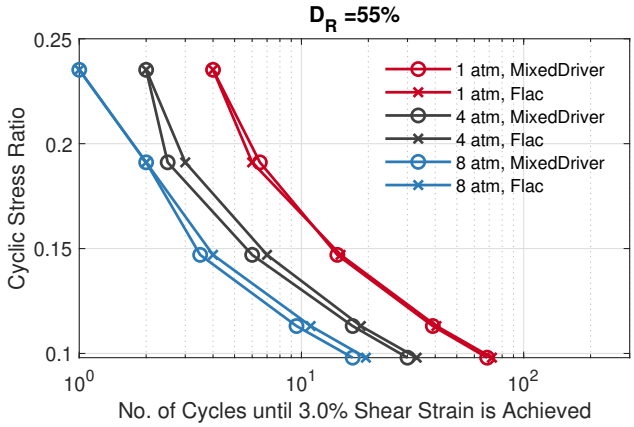

(b)

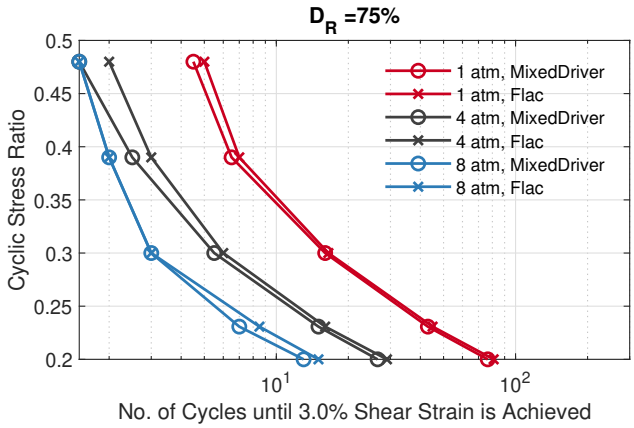

(c)

Figure 3.5: Cyclic stress ratios vs. number of cycles to reach 3% SA shear strain for (a) $D_R = 35\%$, (b) $D_R = 55\%$, and (c) $D_R = 75\%$, with initial vertical consolidation stresses of $\sigma_v = 1$, 4, and 8 atm., and $K_0 = 0.5$.

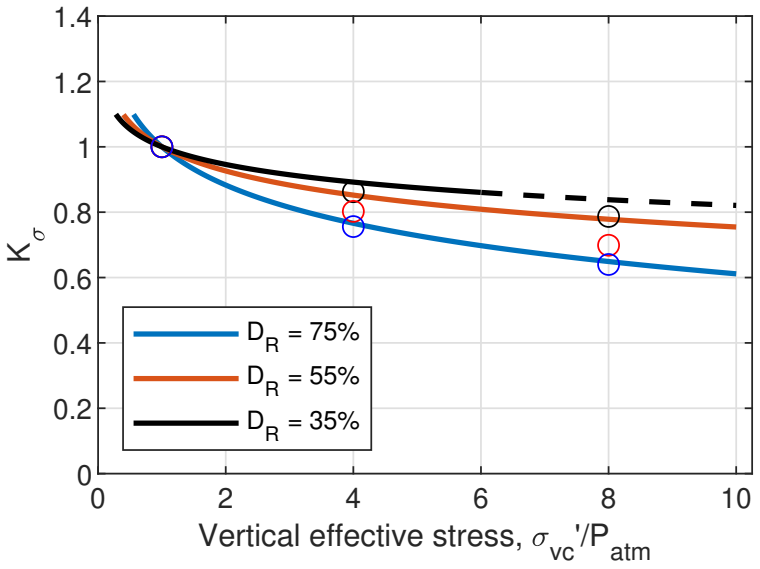

Figure 3.6: Comparison of simulated K_σ factors—determined at 15 uniform cycles resulting in 3% SA shear strain—to relationships recommended by Idriss and Boulanger (2008).

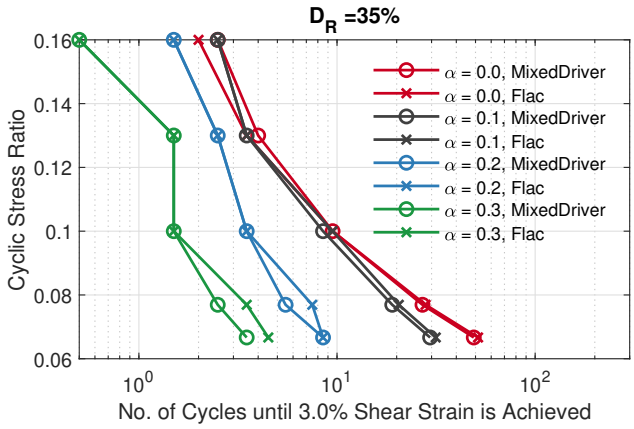

(a)

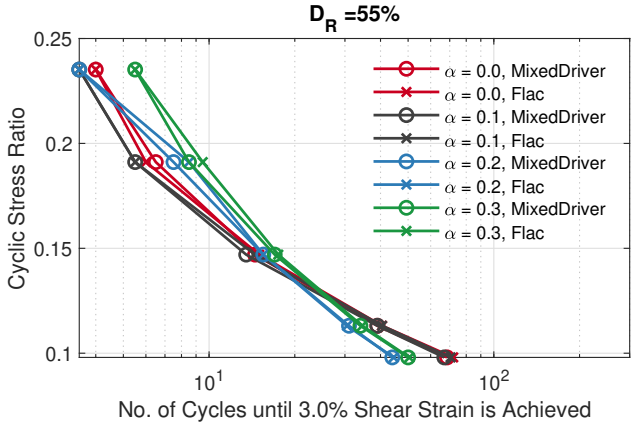

(b)

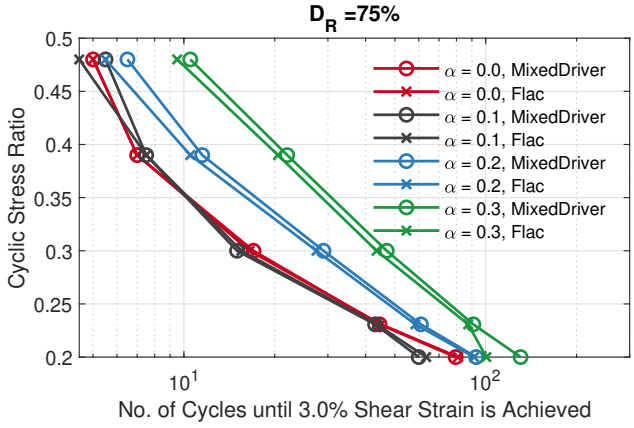

(c)

Figure 3.7: Cyclic stress ratios vs. number of cycles to reach a 3% SA shear strain for (a) $D_R = 35\%$, (b) $D_R = 55\%$, and (c) $D_R = 75\%$ with an initial static shear stress ratios (α) of 0.0, 0.1, 0.2, and 0.3, $\sigma_v = 1$ atm and $K_0 = 0.5$.

3.2.2 Single-Element Simulations using OpenSees

After simulations using *MixedDriver* showed satisfactory results, the model was carried into OpenSees and its response in OpenSees was verified using single-element analyses. The model was paired with coupled four-node quadrilateral elements in OpenSees: SSPquadUP (McGann et al., 2015) and QuadUp (Yang et al., 2003), respectively, to investigate the effective stress response under undrained conditions, which is the most common application scenario for this model.

The results using both elements showed a good match with *MixedDriver* and FLAC simulations. For brevity, only results obtained using the SSPquadUP element are presented here. This element uses a single integration point and a stabilization method to prevent hour-glass locking modes. In addition to nodal displacements, it provides a pore water pressure degree-of-freedom. Because this pore water pressure is stored in a velocity vector, transient analyses are necessary in all undrained simulations; therefore, during the OpenSees simulation the Newmark integration scheme was used to advance in time with parameters $\beta = \frac{5}{6}$ and $\gamma = \frac{4}{9}$. This pair of β and γ were chosen to introduce additional numerical damping and damp out any undesirable vibrations not included in *MixedDriver* results.

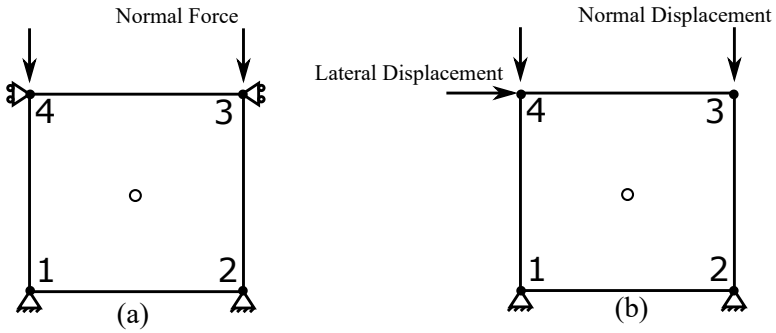

Figure 3.8: SSPquadUP element configuration for strain-controlled cyclic simple shear test during (a) consolidation phase and (b) shearing phase.

In contrast to *MixedDriver*, the OpenSees simulations require the application of forces and/or displacements to impose initial conditions and shearing loads. In OpenSees, during the consolidation phase, the bottom of the element was fixed in all directions, and the top nodes of the element were tied together in the horizontal direction (using *EqualDOF*). A normal pressure in the form of concentrated loads to the nodes was applied to the top nodes to create a consolidation condition. Figure 3.8 illustrates the test configuration during the consolidation stage. Normal forces were incrementally increased at the nodes until the desired consolidation pressure was reached in the element. During this phase, a Poisson's ratio, $\nu = 0.33$, was used to produce an initial lateral stress that matched a $K_0 = 0.5$.

Figure 3.8b illustrates the test configuration during the shearing phase where the normal forces were replaced by equivalent vertical nodal displacements to maintain the pressure. The material was re-initialized, and ν was updated to 0.3 before applying a lateral displacement used to apply shearing. Figures 3.9 and 3.10 compare the results obtained using the

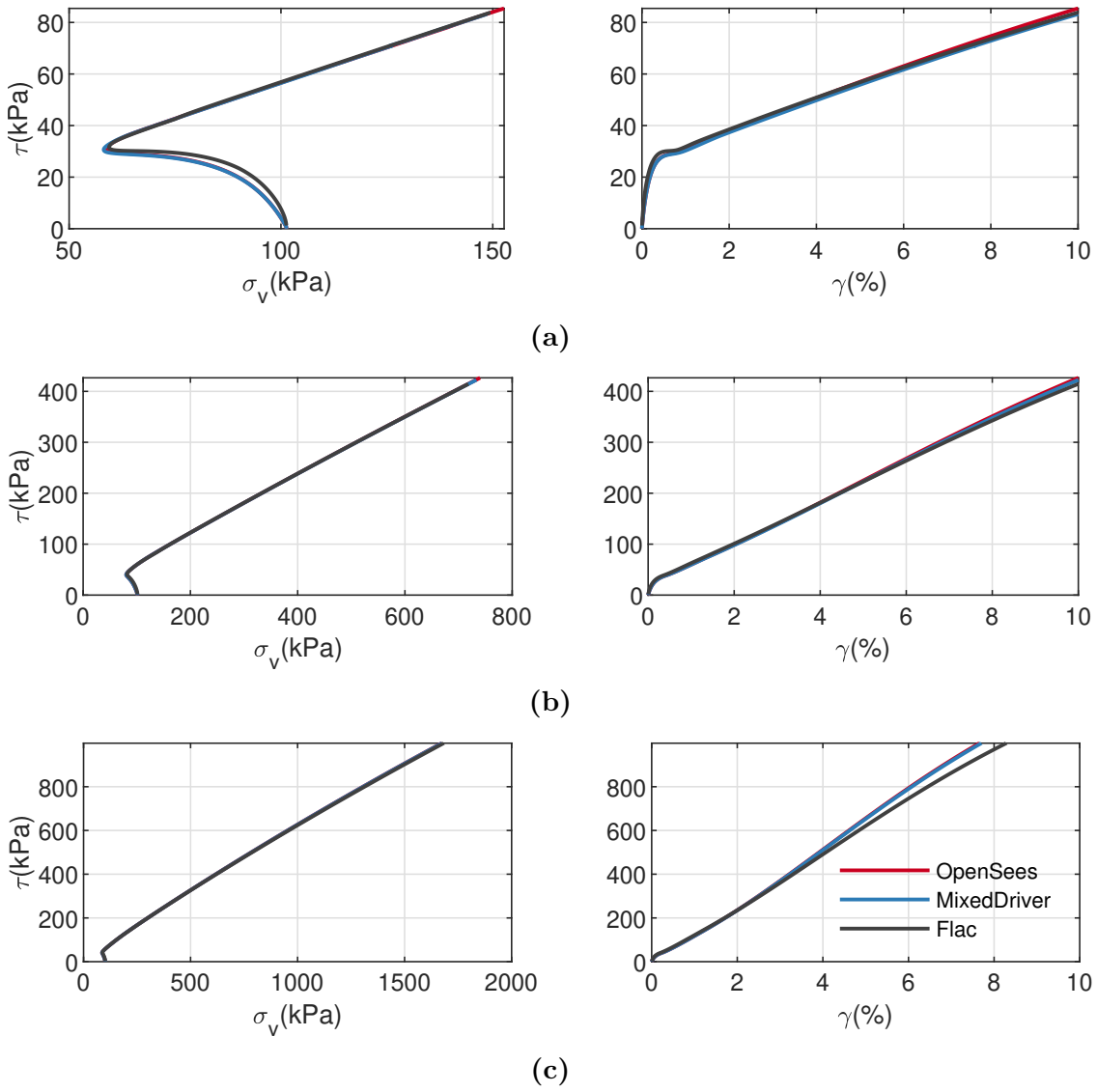

Figure 3.9: Comparison of results obtained using *MixedDriver*, OpenSees, and FLAC for an undrained monotonic DSS loading, initial vertical stress σ_v = 1 atm, and various D_R: (a) $D_R = 35\%$, (b) $D_R = 55\%$, and (c) $D_R = 75\%$.

OpenSees single-element model and the corresponding results from the single-point integration method using *MixedDriver* and the FLAC single-element model. The good match attained demonstrates that the implementation of the constitutive model in OpenSees is accurate and reproduces the expected response.

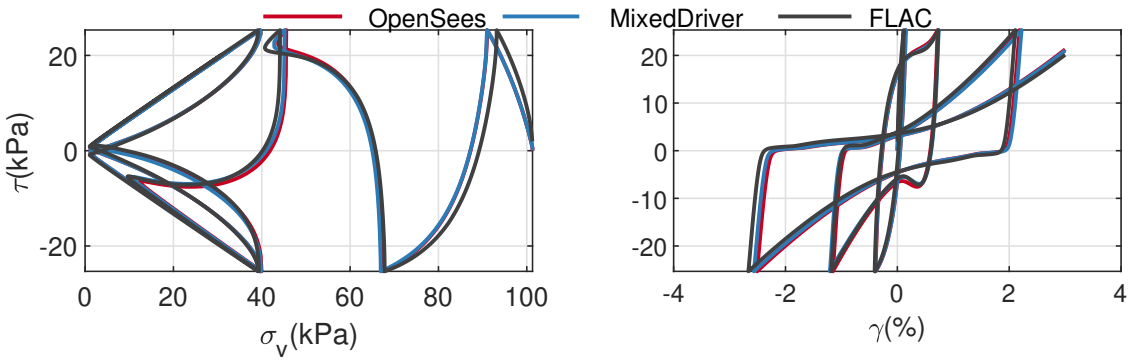

Figure 3.10: Comparison of results obtained using *MixedDriver*, OpenSees, and FLAC for an undrained cyclic DSS loading, initial vertical stress of 1 atm, and $D_R = 55\%$.

3.3 VERIFICATION OF PM4SAND USING 1D-LEVEL GROUND SITE RESPONSE ANALYSIS

Once verified at the point and element levels, PM4Sand was verified using 1D soil columns. For this purpose, a group of 1D single columns of quadrilateral elements was used to simulate site response analysis using the OpenSees framework. The objective was to test the implementation and assess whether or not the model performed well in a more practical geotechnical scenario. The results were also compared with FLAC analyses performed by Andrew Makdisi at the University of Washington, and PLAXIS 2D analyses performed by Gregor Vilhar at PLAXIS, BV. More details can be found in Chen (2020). This study offered the opportunity to directly compare the response of the same model (PM4Sand) implemented in three different frameworks and used by three different users. In addition, this study provided the opportunity to assess the variability associated with each framework, e.g., discretization scheme, solid-fluid coupling, and different implementation details. An independent verification study also showed good agreement between PLAXIS and FLAC at the element level (Vilhar et al., 2018).

3.3.1 Model building

Soil Profile and Material Properties

For this verification study, six synthetic 1D soil profiles were created. As shown in Figure 3.11, each profile had a layered soil configuration composed of a dry crust, a liquefiable layer, and a base layer. The dry crust and liquefiable layers had an uniform $(N_1)_{60}$. A total of three $(N_1)_{60}$ values—5, 10, and 20—were considered to cover a wide range of soil conditions. The ground water table (GWT) was located at 2 m below the surface for all three cases, and the liquefiable layer was underlain by a 1m base layer. Both the liquefiable layer and dry crust were modeled using PM4Sand. The base layer was modeled using an elastic isotropic material available in all three programs. Two different thicknesses of liquefiable layer—3m and 6m—were considered to study the effect of thickness of liquefiable layer on the response. As schematic of the soil column is illustrated in Figure 3.11. All the simulated soil profiles are listed in Table 3.2.

Table 3.2: Summary of 1D soil profiles.

ID	Thickness of liquefiable layer(m)	$(N_1)_{60}$
N5T3	3	5
N5T6	6	5
N10T3	3	10
N10T6	6	10
N20T3	3	20
N20T6	6	20

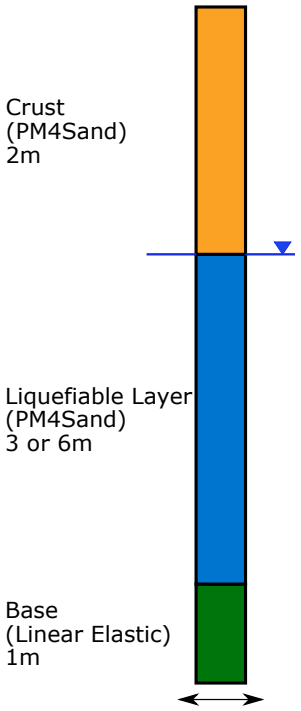

Figure 3.11: Illustration of the 1D level ground model.

The model calibration followed the procedure recommended by Boulanger and Ziotopoulou (2017) for a case where *in situ* tests were available. D_R was estimated based on $(N_1)_{60}$ as,

$$D_R = \sqrt{\frac{(N_1)_{60}}{C_d}}\,, \tag{3.5}$$

where $c_d = 46$ (Idriss and Boulanger, 2008). The overburden stress-corrected shear-wave velocity V_{s1} was estimated using the correlation proposed by Andrus and Stokoe (2000),

$$V_{s1} = 85[(N_1)_{60} + 2.5]^{0.25}\,, \tag{3.6}$$

and the small-strain shear-wave velocity V_s at each location was calculated using Robertson (1991),

$$V_s = \rho V_{s1}\left(\frac{\sigma'_v}{p_A}\right)^{0.25}\,, \tag{3.7}$$

where σ_v is the initial vertical effective stress, and p_A is the atmospheric pressure. The relationship for G_{max} in PM4Sand is based on the mean in-plane effective stress, and the model input parameter G_o was calculated from the following equation,

$$G_{max} = \rho V_s^2 = G_o p_A\left(\frac{p}{p_A}\right)^{0.5} = G_o p_A\left(\frac{1+K_0}{2}\frac{\sigma'_v}{p_A}\right)^{0.5}\,, \tag{3.8}$$

where $K_0 = 0.5$. ρ is the density of soil, which was computed using default values of $e_{max} = 0.8$ and $e_{min} = 0.5$, and specific gravity $G_s = 2.67$. Density was taken as the dry

density above GWT and saturated density below. Target CRRs were calculated following the correlation proposed by Idriss and Boulanger (2008) using $(N_1)_{60}$. After determination of D_R, G_o, and CRR, h_{po} was calibrated iteratively to match the CRR for a 3% single amplitude (SA) shear strain reached at 15 cycles in an undrained CDSS test. The cyclic strength curves obtained using the calibrated model parameters are presented in Figure 3.12, and the resulting input material properties are summarized in Table 3.3. All secondary parameters were kept at their default values.

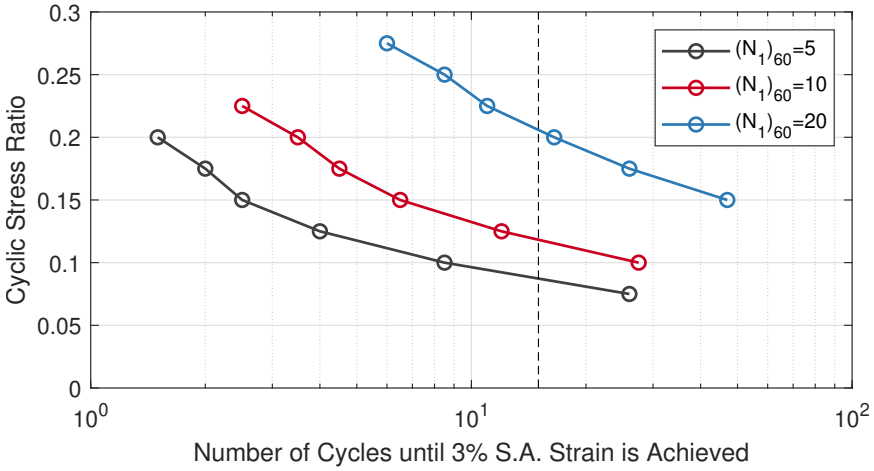

Figure 3.12: Number of cycles required to reach 3% SA shear strain in simulated undrained CSS tests with initial $K_0 = 0.5$ for three D_Rs.

Table 3.3: Input parameters for PM4Sand.

	N5T3 & N5T6		N10T3 & N10T6		N20T3 & N20T6	
	Dry	Saturated	Dry	Saturated	Dry	Saturated
D_R	0.330	0.330	0.466	0.466	0.659	0.659
G_o	354.0	447.0	468.3	584.1	651.0	798.0
h_{po}	0.533	0.533	0.463	0.450	0.425	0.388
$\gamma(kN/m^3)$	15.40	19.44	15.80	19.70	16.30	20.0
$CRR_{M=7.5}$	0.086	0.086	0.118	0.118	0.206	0.206

The soil columns were built to represent a compliance base condition. Because PM4Sand in FLAC has not been configured to work with FLAC's "free-field" boundary condition and cannot be assigned to the bottom row of elements above a compliance base, an elastic layer was included at the bottom of the model (Boulanger and Ziotopoulou, 2017). The density of the isotropic elastic material was set to be same as the saturated density of the layer above, and its stiffness was chosen to produce a wave impedance ratio $(\rho_2 v_2/\rho_1 v_1) = 1.3$. The properties of the isotropic elastic material are summarized in Table 3.4. A small (10^{-10}) permeability was chosen for all layers to minimize pore pressure migration and its effect on material response. Note: the so called *permeability* input parameter in FLAC and OpenSees

Table 3.4: Input parameters for isotropic elastic material.

	N5T3	N5T6	N10T3	N10T6	N20T3	N20T6
$V_s(m/sec)$	159.0	176.0	182.0	200.0	212.0	235.0
$E(kPa)$	1.30×10^5	1.60×10^5	1.73×10^5	2.09×10^5	2.38×10^5	2.93×10^5
ν	0.3					
$\gamma(kN/m^3)$	19.44	19.44	19.70	19.70	20.0	20.0

is defined as the conventional hydraulic conductivity (units: [L/T] - e.g., m/sec) divided by unit weight of water (units: [F/V] - e.g., Pa/m). Some literature refers to it as *dynamic permeability coefficient*; see Parra-Colmenares (1996). In PLAXIS, the conventional hydraulic conductivity is directly input.

Input Motions

Three outcrop motions were selected based on computed CRR so that their peak horizontal accelerations were high enough to induce factors of safety < 1 for liquefaction triggering following the correlation proposed by Seed and Idriss (1971),

$$CSR = 0.65 \frac{\sigma_{vc}}{\sigma'_{vc}} \frac{a_{max}}{g} r_d \,, \tag{3.9}$$

where r_d is a shear-stress reduction coefficient calculated using the correlation proposed by Idriss and Boulanger (2008).

Although a rigorous sensitivity study on the effect of input motion was not included in this study, attention was paid during motion selection so that the motions had different characteristics, including peak ground acceleration (PGA), duration, and predominant frequency. The selected motions were: RSN766, Gilroy #2 from the 1989 Loma Prieta earthquake; RSN963 from the 1994 Northridge earthquake; and RSN1203 from the 1999 Chi-Chi earthquake.

Hereafter, they are refereed by their ID number. Acceleration time histories and response spectra of each motion are presented in Figure 3.13. Details of these motions are listed in Table 3.5. Note that a fourth motion was also included. This motion is a scaled version of RSN766 with PGA of $0.02g$, which was used to verify boundary and initial conditions of the soil columns and ensure consistency among different platforms. More information on this process is given in the following section.

Boundary Conditions

In OpenSees, simulation of the groundwater table (GWT) was achieved by fixing the nodal degrees-of-freedom for pore pressure at the selected GWT depth. Therefore, no pore water pressure was allowed to develop in the dry zone. In FLAC, the GWT was modeled by setting initial pore pressures to be zero above the GWT. Note: these dry nodes could experience

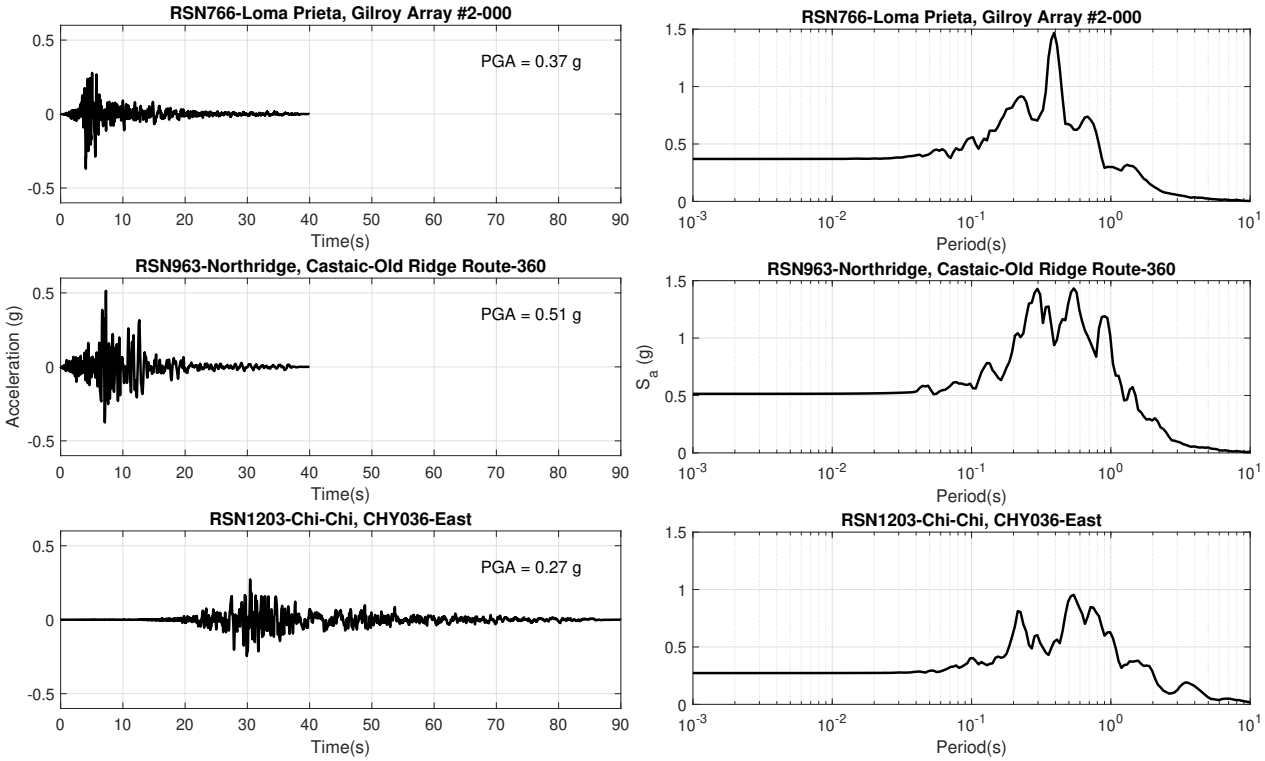

Figure 3.13: Summary of selected input motions: (a) acceleration time histories and (b) acceleration response spectra with 5% damping.

change in pore pressure due to dissipation of excess pore water pressure from underlain nodes. In PLAXIS, the dynamic-with-consolidation analysis type allows excess pore pressure development above the GWT. Thus, pore pressure migration to the dry layer above GWT was expected in FLAC as well as in PLAXIS results.

Displacement degrees-of-freedom were tied at the same elevation in all three programs. In this study, quadrilateral SSPquadUP elements were used in all OpenSees analyses. Quadrilateral zones with four overlapping triangular subzones were used in FLAC analyses. Therefore, the OpenSees and FLAC columns both had one element/zone at each level. Because there are no quadrilateral element available in PLAXIS, higher order fifteen-node triangular elements were used. This led to more than one element at each level in the PLAXIS columns; see Figure 3.15. Therefore, although vertical side boundaries were tied together in all three models to represent a 1D free-field wave propagation, some degree of two-dimensional response might be present in PLAXIS model results. The input motion was applied through a Lysmer dashpot (Lysmer and Kuhlemeyer, 1969), and the stiffness of the dashpot was the same as the base elastic layer.

Table 3.5: Details of selected input motions

Name	Duration(sec)	Time step(sec)	PGA(g)
RSN766_G02_000(Loma Prieta)	39.99	0.005	0.37
RSN963_ORR_360(NorthRidge)	40	0.02	0.51
RSN1203_CHY036_E(Chi-Chi)	90	0.005	0.27
RSN766_G02_000_VEL_0p02g(Loma Prieta, scaled)	39.99	0.005	0.02

Analysis Parameters

Rayleigh damping was added to compensate for small-strain damping observed in laboratory tests results and not captured by the model in its elastic range. FLAC uses a single-frequency formulation for Rayleigh damping, and f_{min} and ξ_{min} are the required input parameters. OpenSees and PLAXIS use a two-frequency formulation, where α and β are the required input parameters. f_{min} and ξ_{min} can be related to α and β through:

$$\begin{aligned} \alpha &= \frac{2\xi_c\omega_1\omega_2}{\omega_1+\omega_2}\,, \\ \beta &= \frac{2\xi_c}{\omega_1+\omega_2}\,, \end{aligned} \tag{3.10}$$

$$\begin{aligned} \alpha &= \xi_{min}\omega_{min}\,, \\ \beta &= \xi_{min}/\omega_{min}\,, \end{aligned} \tag{3.11}$$

and

$$\xi_{min} = 2\pi f_{min}\,, \tag{3.12}$$

where ξ_{min} is the minimum damping ratio, and f_{min} is the corresponding frequency. Figure 3.14 compares the attained Rayleigh damping in both cases. The two frequencies were selected as the natural frequency of the soil column ($\frac{V_s}{4H}$, where V_s is the average shear-wave velocity, and H is the total thickness of the soil column) and five times the natural frequency of the soil column. This follows recommendations by Kwok et al. (2007).

Table 3.6: OpenSees analysis parameters.

Rayleigh Damping	α	0.786969	f_{min}	5.01
	β	0.000794	ξ_{min}	0.025
Element Size	0.25m			
Time Step	0.0001s			

Hourglass locking is a well-known problem when using reduced integration schemes. To mitigate this effect, the PM4Sand implementation in FLAC includes an elasto-plastic material parallel to PM4Sand that inserts artificial stiffness to the hourglass deformation

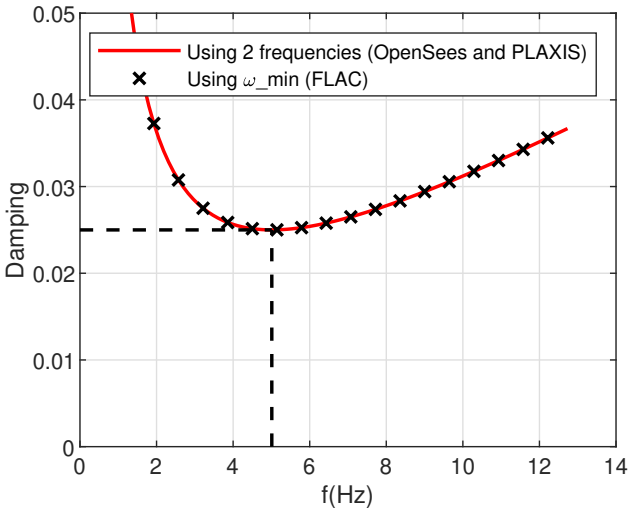

Figure 3.14: Comparison of Rayleigh damping in FLAC, OpenSees, and PLAXIS.

modes. In OpenSees, this effect is mitigated in the SSP-family elements that use a stabilization algorithm (McGann et al., 2012), resulting in an element that is free from volumetric and shear locking. In this study, the SSPquadUP with a stabilization parameter α of 10^{-6} was used. Since PLAXIS utilizes higher order elements and a more refined mesh, it does not require additional consideration for hourglass locking.

The selected model discretization for each platform is illustrated in Figure 3.15. The figure clearly shows that due to different discretization schemes, the meshes were different in all three numerical models. Therefore, a verification study was required to check sensitivity of results with mesh refinement.

3.3.2 Analysis Metrics

For the level ground case, peak horizontal acceleration (PHA), maximum horizontal displacement, maximum shear strain (γ_{max}), maximum excess pore pressure ratio (r_u), and maximum cyclic stress ratio (CSR) along the soil profile were used as metrics for comparison purposes and to assess the model behavior. The acceleration response at the surface was also used in this comparison.

r_u can be computed using excess pore pressure as,

$$r_u = \frac{\Delta u}{\sigma'_{v,0}}\,, \tag{3.13}$$

where Δu is the change in pore pressure, and $\sigma'_{v,0}$ is the initial vertical effective stress at that location, or using the change in effective vertical stress,

$$r_u = 1.0 - \frac{\sigma'_v}{\sigma'_{v,0}}\,, \tag{3.14}$$

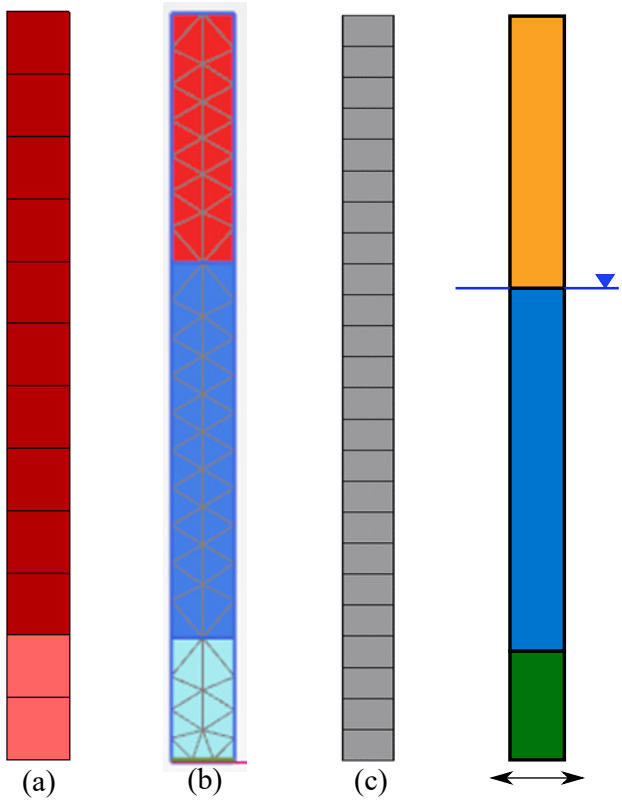

Figure 3.15: Comparison of model discretization for N10T3 case: (a) FLAC model with 12 quadrilateral zones with four triangles each; (b) PLAXIS model with 72 15-node triangular elements; and (c) OpenSees model with 24 four-node quadrilateral elements.

This study computed r_u using both definitions; the results were consistent within the saturated layer. In the dry layer, the stress state tended to converge to $K_0 = 1$, and σ'_v tended to change for the reason discussed above. Because this can lead to unrealistic r_u, only the excess pore pressure based r_u results are presented.

The cyclic stress ratio (CSR) was calculated as follows:

$$CSR = 0.65 \frac{\tau_{max}}{\sigma'_{v,0}}\,, \tag{3.15}$$

where the factor 0.65 is included for liquefaction evaluation procedures, and τ_{max} is the maximum shear stress observed during analysis at a certain location.

Arias intensity was used to measure the strength of each ground motion and computed as follows:,

$$I_A = \frac{\pi}{2g} \int_0^{T_d} a(t)^2 dt\,, \tag{3.16}$$

where T_d is the duration of the motion.

3.3.3 Model Verification

As a first step in this study, the soil columns were verified in the elastic range using a weak motion to ensure consistency among models and modelers. Motion RSN766 was scaled down to $0.02g$ so the new motion was weak enough to induce an almost purely elastic response and avoid possible discrepancies caused by material nonlinearity. By mostly staying in the elastic range, any small-strain damping, including damping induced by the integration scheme and Rayleigh damping, could be verified as well as the wave propagation based on the low-strain stiffness. Mesh refinement and boundary conditions were also verified by checking simulated acceleration responses.

Secondary parameters for PM4Sand were computed during the time of material initialization using the existing stress state. The stress state could be applied directly in FLAC, while in PLAXIS the so-called K_0 procedure was used. In OpenSees, a gravity analysis phase using an elastic material was applied. The elastic material had the same unit weight and low-strain stiffness as the corresponding nonlinear material. Note: the other differences between the models studied require computing for the initial stress state between the three programs: (a) in OpenSees and for the SSPquadUP element, density and a vector describing the gravitational acceleration are required; (b) in PLAXIS, the unit weight of the material has to be specified; and (c) in FLAC, the user specifies dry density and void ratio. In order to avoid inconsistencies in the initial stress state, and, in turn, in secondary parameters, initial stress fields were carefully compared and examined. For added confidence, the same analysis was also performed using ProShake [EduPro Civil Systems (2017), here referred as PS] and DeepSoil [Hashash et al. (2016), here referred as DS].

As shown in Figures 3.16 to 3.18, all five programs produced very similar results in terms of PHA, γ_{max}, and CSR along the column, as well as acceleration time history and Arias intensity at the surface. Note that a constant 2% damping instead of Rayleigh damping was used in PS and DS analyses; therefore, all the other three programs showed slightly smaller PHA in the profile plots and weaker Arias intensity in Figure 3.17 due to extra frequency dependent damping. γ_{max} and CSR profiles in Figure 3.16 also showed good agreement in spite of PLAXIS results showing the effect of discretization. Location of γ_{max} from PLAXIS was slightly shifted and contributed to its more refined mesh and higher density of stress points.

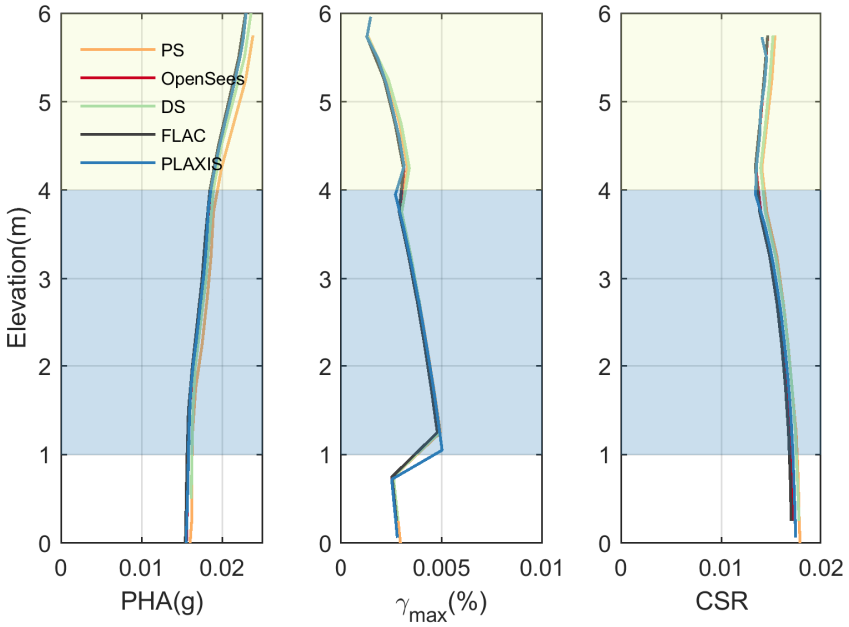

Figure 3.16: Comparison of PHA, γ_{max}, and CSR from PS, OpenSees, DS, FLAC, and PLAXIS.

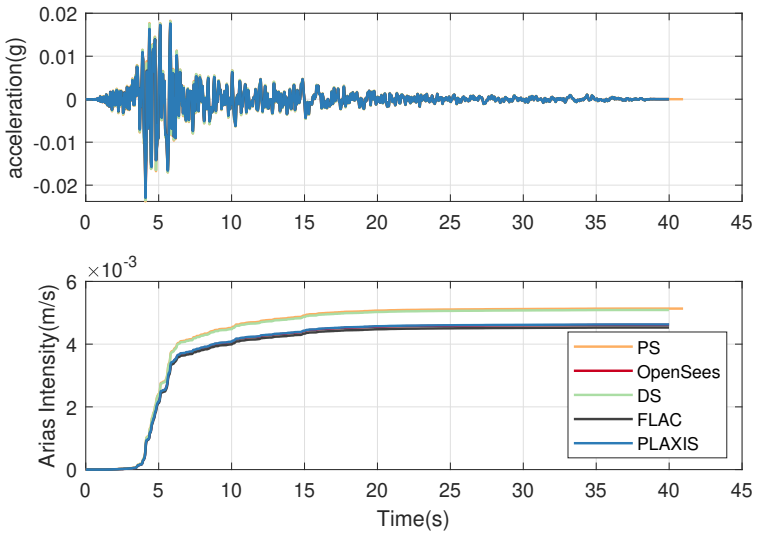

Figure 3.17: Comparison of simulated acceleration time histories and Arias intensity at the surface from PS, OpenSees, DS, FLAC, and PLAXIS.

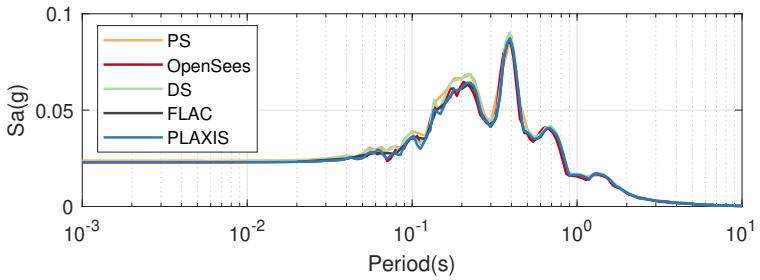

Figure 3.18: Comparison of simulated acceleration response spectra (5%) at the surface from PS, OpenSees, DS, FLAC, and PLAXIS.

3.3.4 Free-Field Verification Results

Once the model was verified, the complete set of free-field analysis was done using OpenSees, FLAC, and PLAXIS and results were compared. Due to space constraints, only N10T3 results are presented here. Results for all other five cases can be found in Appendix A. Figures 3.19 through 3.21 depict comparisons of simulated PHA, γ_{max}, maximum displacement, CSR, and max r_u along the soil column. In general, all three programs produced similar results, and liquefaction was triggered as expected. Presence of higher PHA coincided with large γ_{max} and max $r_u = 1$, which indicates the presence of dilation spikes after fully liquefaction of the soil. However, the predicted PHA from FLAC was noticeably higher than from OpenSees and PLAXIS.

Comparison of acceleration time histories at those locations (not shown here) revealed that FLAC tended to produce higher magnitudes of dilation spikes compared to OpenSees and PLAXIS, but all three programs predicted similar times of triggering of these spikes, and the overall acceleration responses were similar. Comparison of the acceleration response at the surface (Figures 3.22 through 3.27) also show the same trend. In terms of CSR, FLAC also tended to predict slightly larger values, which also coincided with higher PHA values. As discussed before, excess pore pressure could be generated within the dry layer in FLAC and PLAXIS analyses. This phenomenon was observed in maximum r_u response even when small permeability was assigned to minimize pore pressure migration. Nevertheless, the results clearly demonstrate that, when carefully performed, PM4Sand in all three programs can produce consistent results. Moreover, the PM4Sand in OpenSees and PLAXIS can be used in site response analysis to study liquefaction triggering.

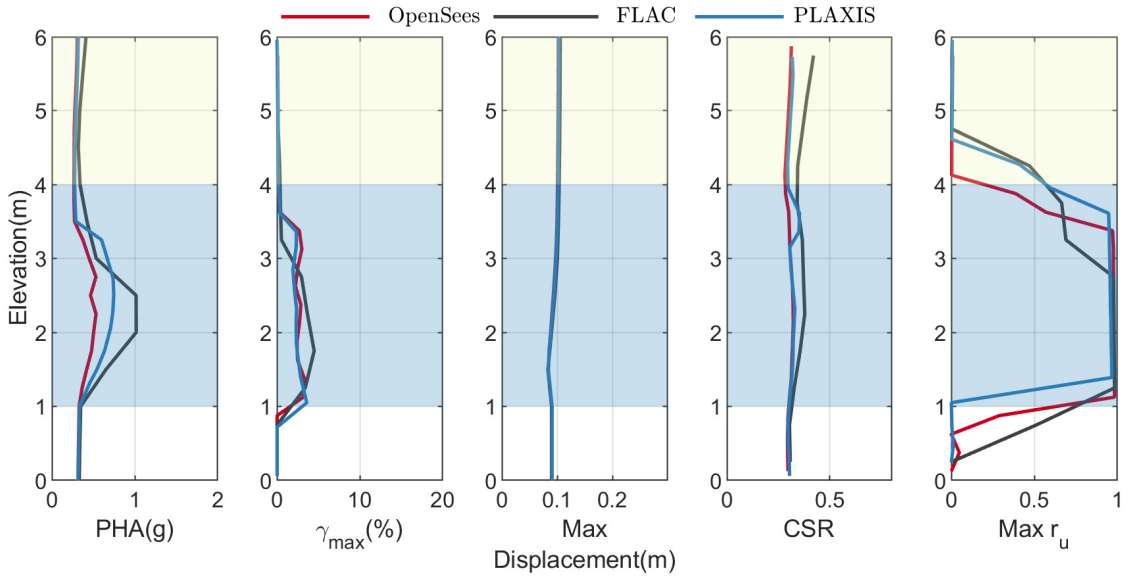

Figure 3.19: Comparison of PHA, γ_{max}, maximum displacement, CSR, and max r_u obtained using OpenSees, FLAC, and PLAXIS for motion RSN766.

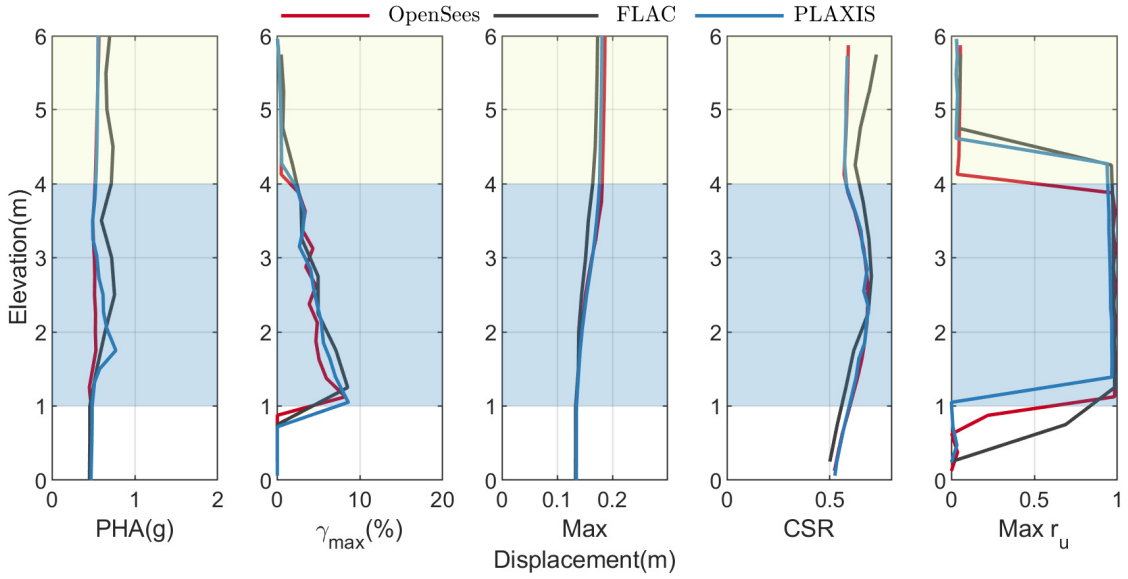

Figure 3.20: Comparison of PHA, γ_{max}, maximum displacement, CSR, and max r_u obtained using OpenSees, FLAC, and PLAXIS for motion RSN963.

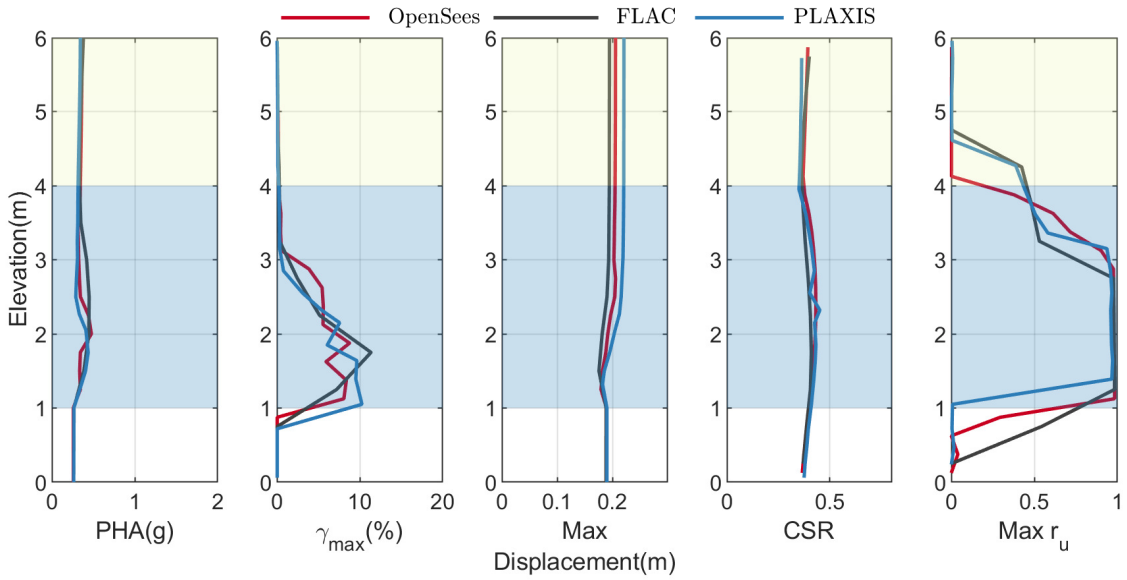

Figure 3.21: Comparison of PHA, γ_{max}, maximum displacement, CSR, and max r_u obtained using OpenSees, FLAC, and PLAXIS for motion RSN1203.

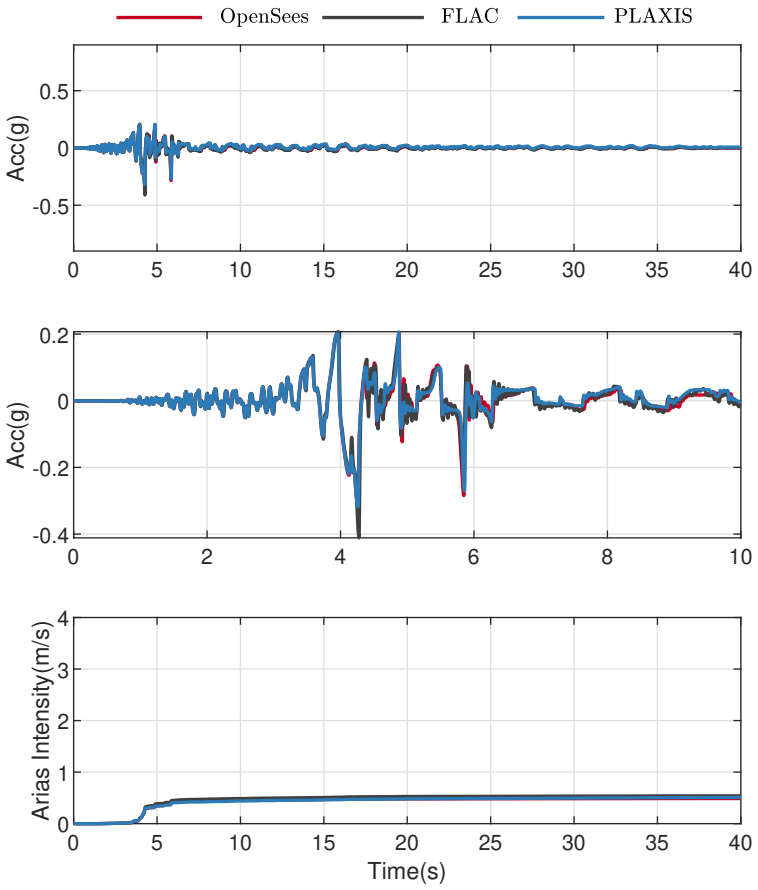

Figure 3.22: Comparison of acceleration time histories at the surface obtained using OpenSees, FLAC, and PLAXIS for motion RSN766. From top to bottom: acceleration time history, close up of acceleration time history, and Arias intensity.

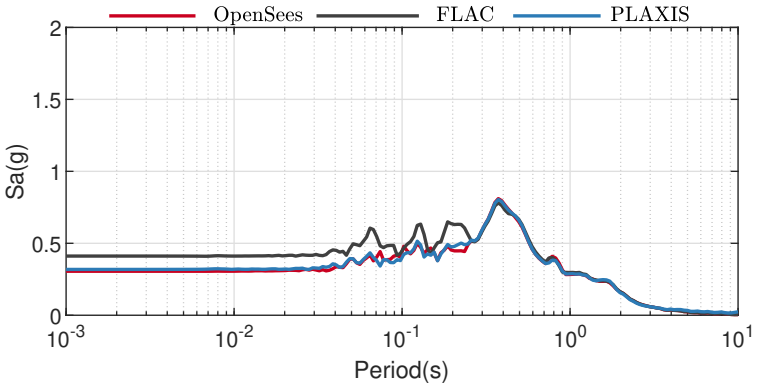

Figure 3.23: Comparison of acceleration response spectra (5%) at the surface obtained using OpenSees, FLAC, and PLAXIS for motion RSN766.

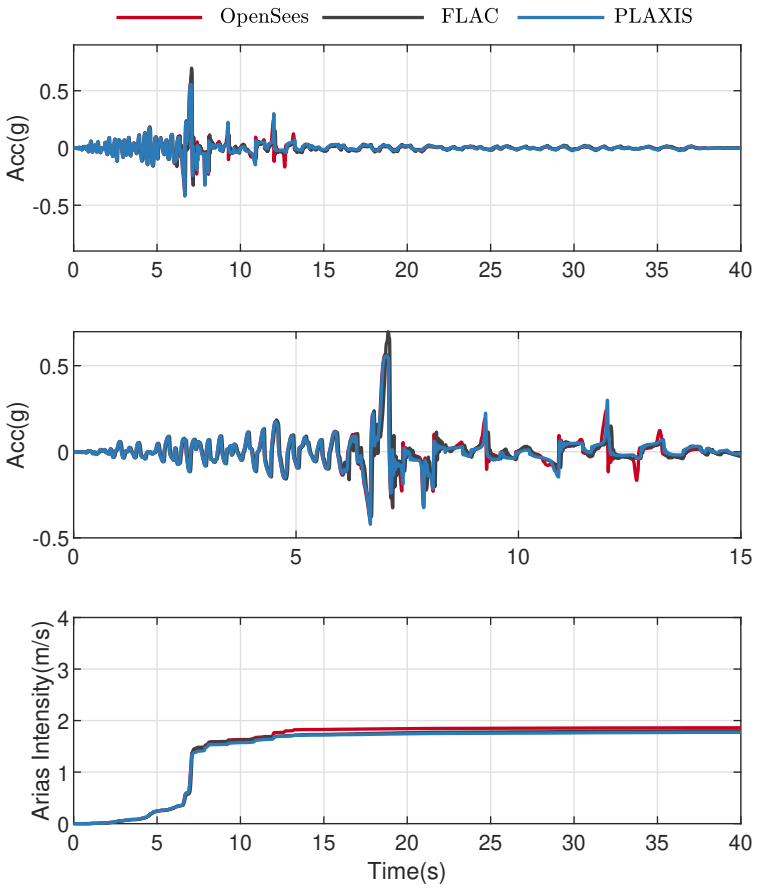

Figure 3.24: Comparison of acceleration time histories at the surface obtained using OpenSees, FLAC, and PLAXIS for motion RSN963. From top to bottom: acceleration time history, close up of acceleration time history, and Arias intensity.

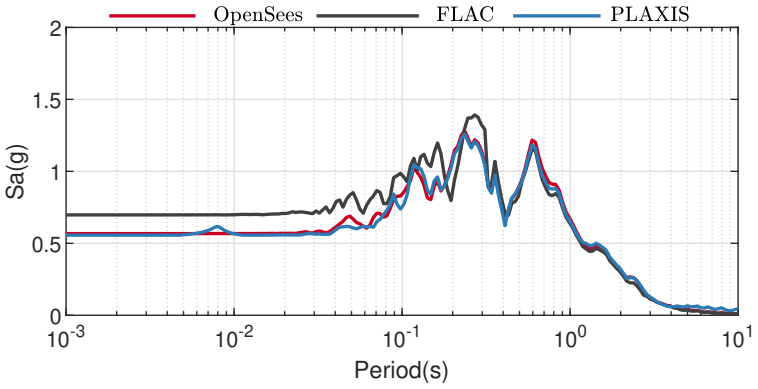

Figure 3.25: Comparison of acceleration response spectra (5%) at the surface obtained using OpenSees, FLAC, and PLAXIS for motion RSN963.

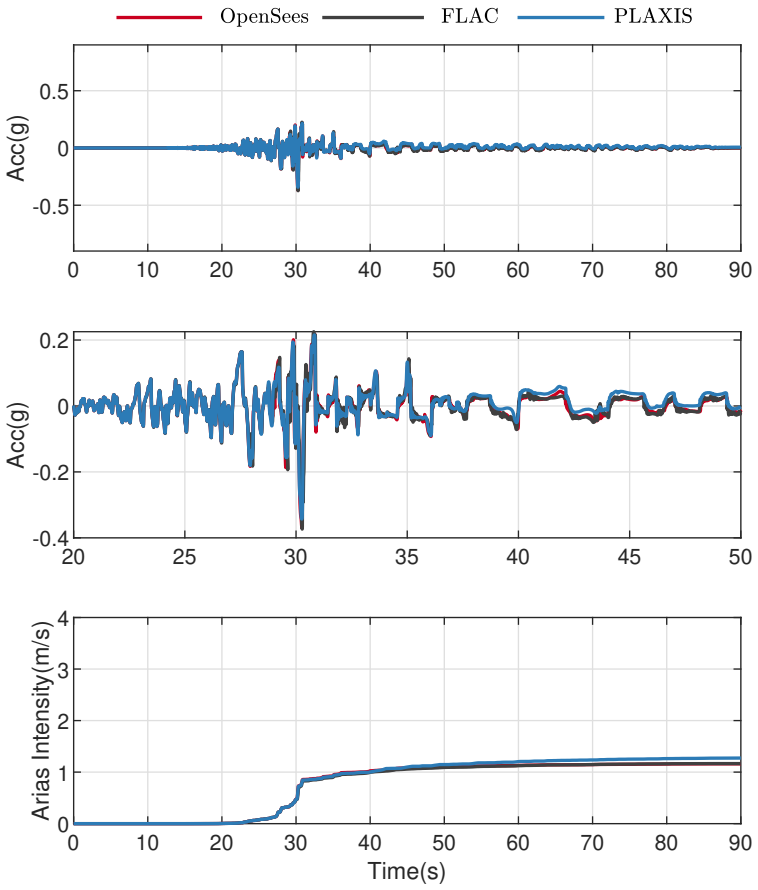

Figure 3.26: Comparison of acceleration time histories at the surface obtained using OpenSees, FLAC, and PLAXIS for motion RSN1203. From top to bottom: acceleration time history, close up of acceleration time history, and Arias intensity.

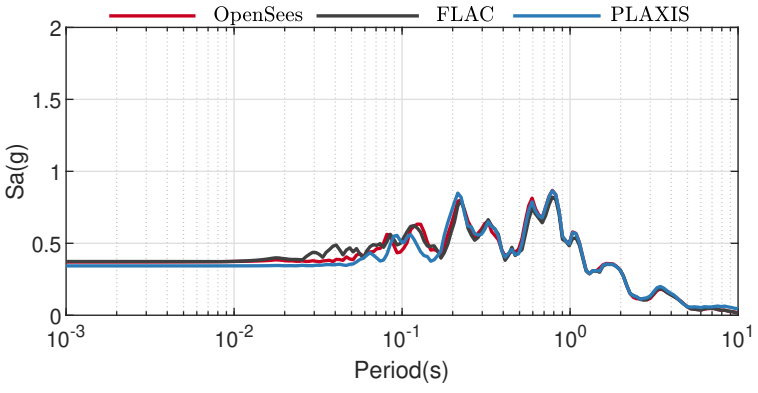

Figure 3.27: Comparison of acceleration response spectra (5%) at the surface obtained using OpenSees, FLAC, and PLAXIS for motion RSN1203.

3.4 ONE-DIMENSIONAL SLOPING GROUND SITE RESPONSE ANALYSIS

PM4Sand has already been used in nonlinear effective stress analyses to study earthquake-induced deformation in gently sloped ground [e.g., embankment dams (Montgomery, 2012)], and infinite slopes (Ziotopoulou, 2017). Although the effect of static shear stress on liquefaction resistance (K_α) of the PM4Sand model OpenSees implementation was verified as shown in Figure 3.7, it was still important to verify the model response within the OpenSees numerical framework. For this purpose, the 1D soil columns presented in the previous section were slightly modified to represent gentle (3%) infinite slopes, as shown in Figure 3.28. Instead of modifying the geometry of the column, the slope was simulated by changing the direction of the gravitational field such that a constant additional horizontal acceleration component representing the slope was applied to the entire column during the dynamic analysis. This case represents a constant infinite slope with no rotational behavior. All three programs (OpenSees, FLAC, and PLAXIS) allowed changes of the gravitational field so modifications were trivial. The three motions presented in the previous section were scaled to three PGA levels, namely $0.1g$, $0.2g$, and $0.3g$ in this study. All the material properties and analysis parameters remained the same.

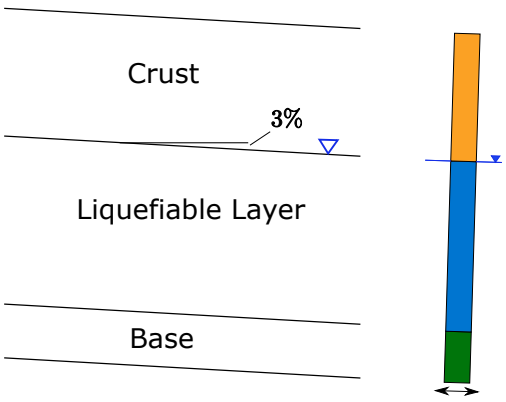

Figure 3.28: Illustration of 1D sloping ground model in terms of soil layering.

Simulation results using $0.3g$ motions are presented in Figures 3.29 to 3.34. For brevity, all other results are included in Appendix A.6. All three programs produced consistent results and showed similar liquefaction trends as observed in the level ground case; FLAC tended to predict higher PHA values. In terms of lateral displacements, all three programs showed the same trend. Only after fully-engaged liquefaction of the material did the programs show evidence of significant and different shear–strain magnitudes, leading to different lateral displacement magnitudes. In contrast to PLAXIS, OpenSees tended to predict slightly higher magnitudes compared to FLAC. Again, this is related to the domain discretization and algorithmic conditions for small confining pressures. Nevertheless, the observed good agreement verifies the OpenSees and PLAXIS implementations of PM4Sand and shows the models as being capable of predicting reasonable results. Note: the predicted shear strains were not

in the small-strain range. For example Figure 3.33 showed γ_{max} over 50%; therefore, the PM4Sand model formulation, as well as any other small strain constitutive model formulation, may not be valid under these circumstances; therefore, any results must be interpreted with caution. In addition to an appropriate formulation, more comprehensive 2D models might be needed for large deformation analyses.

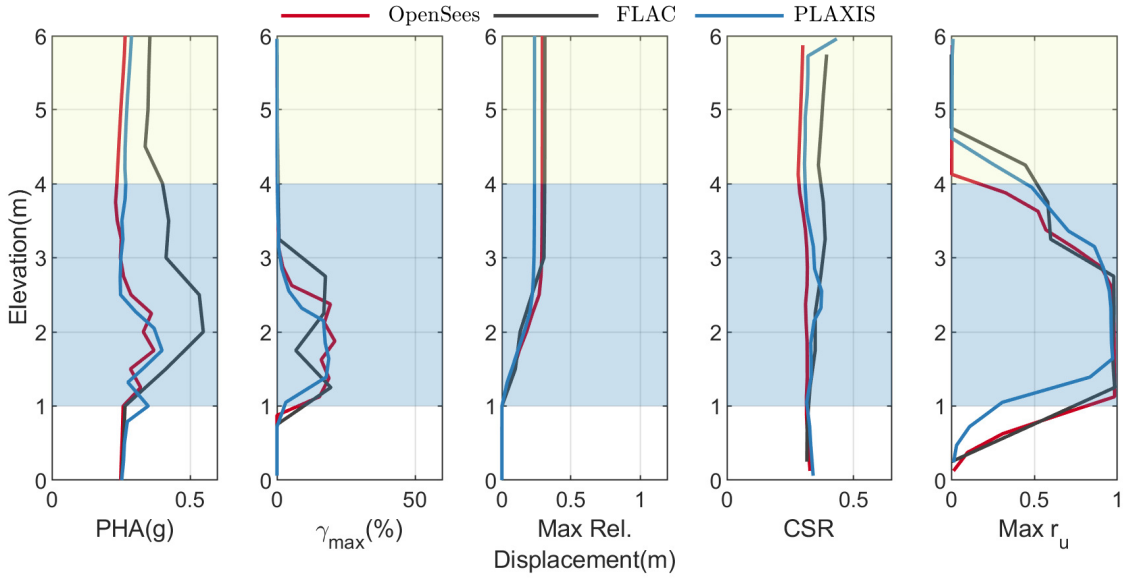

Figure 3.29: Comparison of PHA, γ_{max}, maximum displacement, CSR, and max r_u obtained using OpenSees, FLAC, and PLAXIS for motion RSN766 and $a_{max} = 0.3g$.

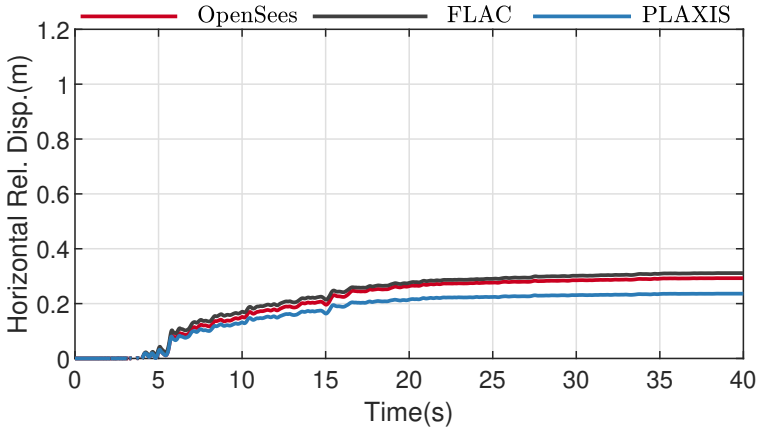

Figure 3.30: Comparison of horizontal displacement at the surface obtained using OpenSees, FLAC, and PLAXIS for motion RSN766 and $a_{max} = 0.3g$.

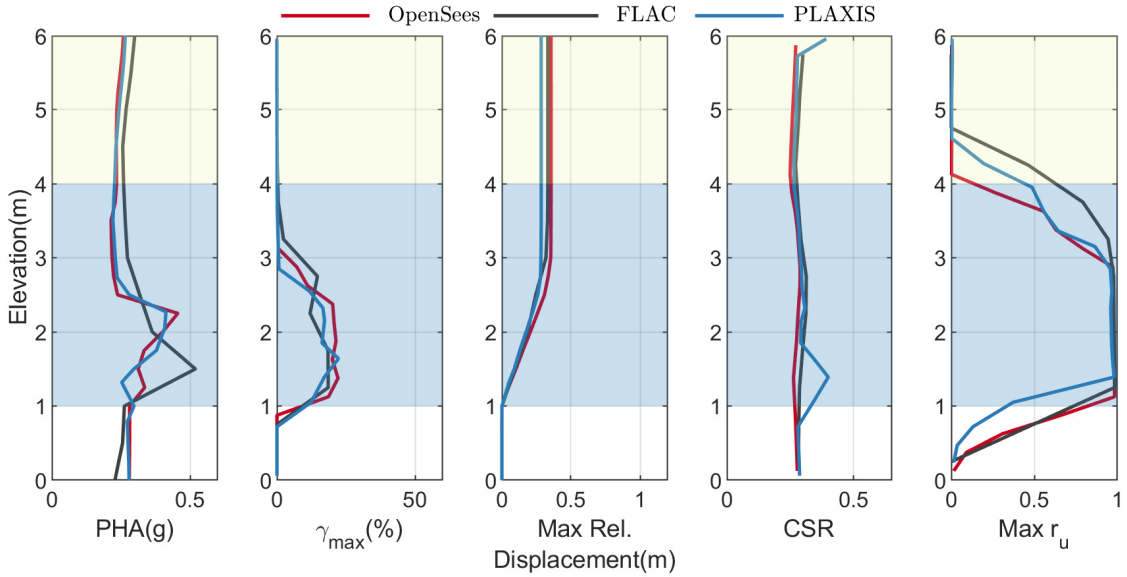

Figure 3.31: Comparison of PHA, γ_{max}, maximum displacement, CSR, and max r_u obtained using OpenSees, FLAC, and PLAXIS for motion RSN963 and $a_{max} = 0.3g$.

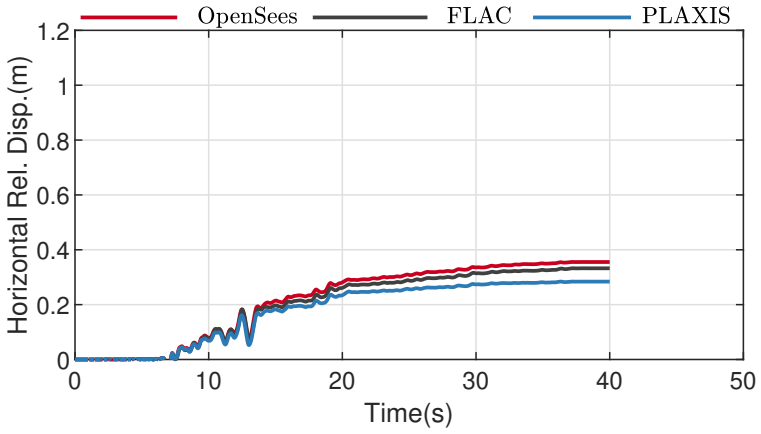

Figure 3.32: Comparison of horizontal displacement at the surface obtained using OpenSees, FLAC, and PLAXIS for motion RSN963 and $a_{max} = 0.3g$.

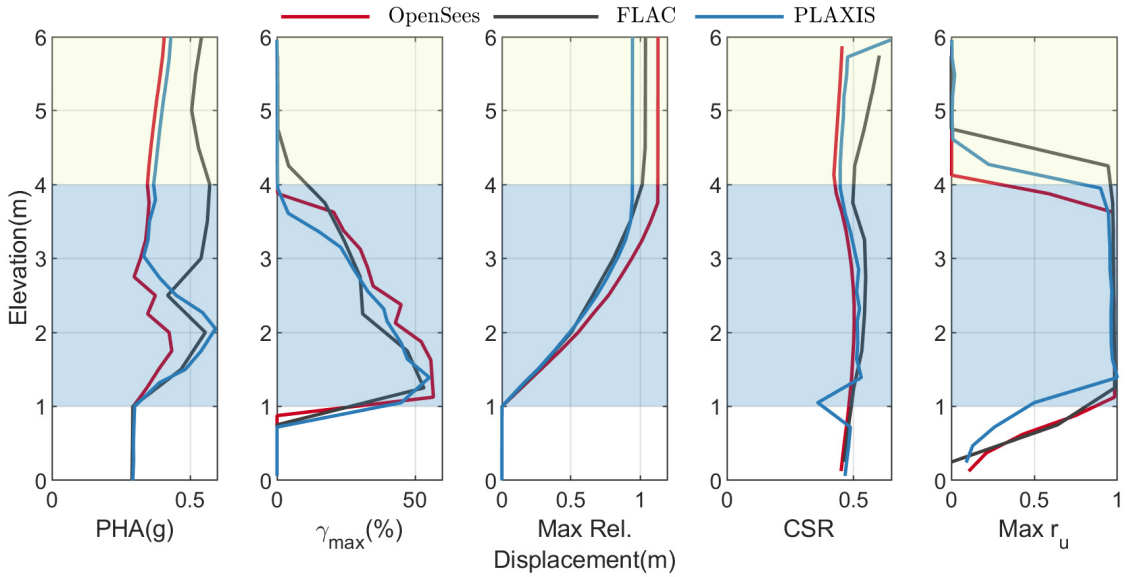

Figure 3.33: Comparison of PHA, γ_{max}, maximum displacement, CSR, and max r_u obtained using OpenSees, FLAC, and PLAXIS for motion RSN1203 and $a_{max} = 0.3g$.

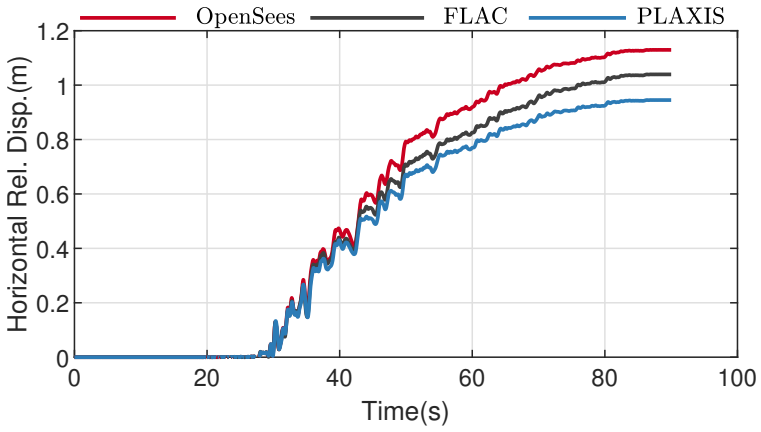

Figure 3.34: Comparison of horizontal displacement at the surface obtained using OpenSees, FLAC, and PLAXIS for motion RSN1203 and a_{max} = 0.3g..

3.5 SUMMARY

This chapter presents the results of a verification study for PM4Sand as implemented in OpenSees using point, single element, and 1D soil column analyses. The results show that, despite discrepancies due to platform differences—finite-element method vs. finite-difference method and different model discretization—the OpenSees implementation produced consistent results to those obtained from FLAC and PLAXIS.

4 Validation of PM4Sand in OpenSees

4.1 INTRODUCTION

This chapter presents the results of a validation study of the PM4Sand model implemented in OpenSees. Ever since its publication, the FLAC model has been used in a wide range of studies, including 1D site response analysis of liquefiable soil deposit (Ziotopoulou et al., 2012), 2D deformation analysis of embankments underlain by liquefied soils (Armstrong et al., 2013), analysis of spatial variability on liquefaction-induced settlement and lateral spreading (Montgomery and Boulanger, 2017), and prediction of centrifuge tests that represent 2D sloping ground (Ziotopoulou, 2017), etc.. These results have proven the model to be satisfactory and provide valuable insight on various problems related to liquefaction. Similarly, the PM4Sand model implemented in OpenSees has also been used in various research projects and has shown its ability to captured soil behavior during liquefaction. In this context, and to complement the aforementioned studies, a study on two well-known case histories are presented in this chapter. Accompanying studies by the authors on type-B and type-C prediction results of centrifuge experiments that represent a 2D sloping ground are presented in Chen et al. (2019).

4.2 SITE RESPONSE ANALYSIS OF WILDLIFE LIQUEFACTION ARRAY

This section describes simulation results for a vertical array installed in liquefiable soil profiles that in the past have captured strong-motion events. It is is widely regarded as one of the best available *in'situ* measurements of a liquefiable soil response to earthquake loading. This array, known as the Wildlife Liquefaction Array (WLA), has been studied extensively by different researchers (Youd et al., 2004; Holzer and Youd, 2007; Sideras, 2011; Ziotopoulou et al., 2012; Kramer et al., 2018). These field recordings provide excellent information to validate liquefiable soil models.

The WLA is a ground motion-monitoring and liquefaction research site located at the southern most terminus of the San Andreas fault system. It is situated in California's Imperial Valley on the west bank of the Alamo River, 13 km north of Brawley, California, and 160 km east of San Diego. This site is instrumented with six piezometers and two accelerometers. One of the piezometers, P5, is buried near the top of a sandy silt layer, and accelerometers are located at 0 m and 7.5 m, respectively. The WLA field site records numerous earthquakes

daily in this seismically active area. Among these events, two significant events have drawn researchers attention: the M6.2 Elmore Ranch event on November 23rd, 1987 (Holzer and Youd (2007)), and its aftershock, the M6.6 Superstition Hills earthquake that occurred the following day. Instruments were triggered, and acceleration and pore pressure time histories were recorded at this site during both events. Liquefaction was not triggered during the Elmore Ranch event; however, liquefaction was triggered during the Superstition Hills earthquake, as evidence by sand boils and ground cracks that were observed at the site. Although questions have been raised regarding the reliability of measured pore pressure during the Superstition Hills event (Kramer et al., 2018), the recorded ground motion (see Figure 4.1) clearly shows dilation pulses and shift of frequency contents after liquefaction triggering. In this study, only the north–south (NS) record was considered.

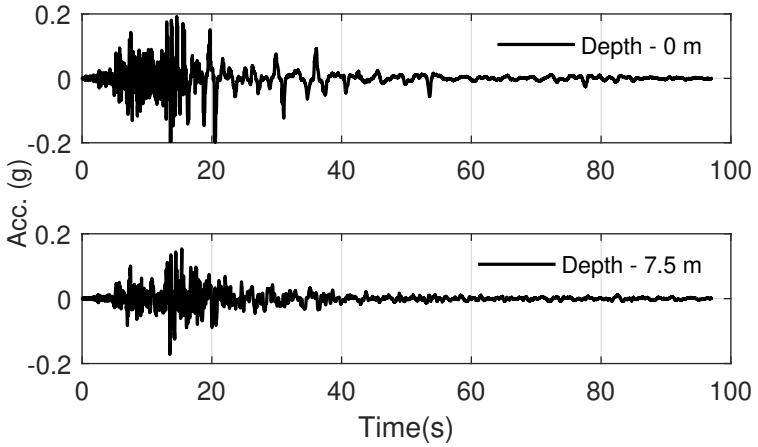

Figure 4.1: Recorded NS horizontal acceleration time histories at various depths for WLA.

In terms of soil conditions, the WLA soil profile consists of four general soil layers: the upper 2.5 m consists of lean clay/silt (CL-ML), underlain by 1 m of sandy silt (ML). Extending 3.3 m below this is a silty-sand (SM) layer, which is liquefiable. This layer is underlain by a 0.7-m deposit of high plastic clay (CH). The water table is at a depth of 1 m below the ground surface. The soil profile along with SPT, CPT, and V_s measurements is shown in Figure 4.2.

For modeling purposes, the profile was divided into five layers; see Table 4.1. Within these five layers, layers 1, 2 and 5 were modeled using the *PresusreIndepenedMultiYield* (PIMY) model available in OpenSees for clayey type soils. The shear modulus G for each layer was calculated using V_s, and the bulk modulus, K, was calculated from G with an assumed $\nu = 0.3$. Modulus reduction (G/G_{max}) curves proposed by Darendeli (2001) were used to define the yield surfaces in the PIMY model.

Darendeli (2001) curves are based on a hyperbolic model and are derived from cyclic laboratory tests (often not run to failure). Consequently, these curves do not necessarily provide an accurate representation of soil strength at large shear strains. In some cases, the

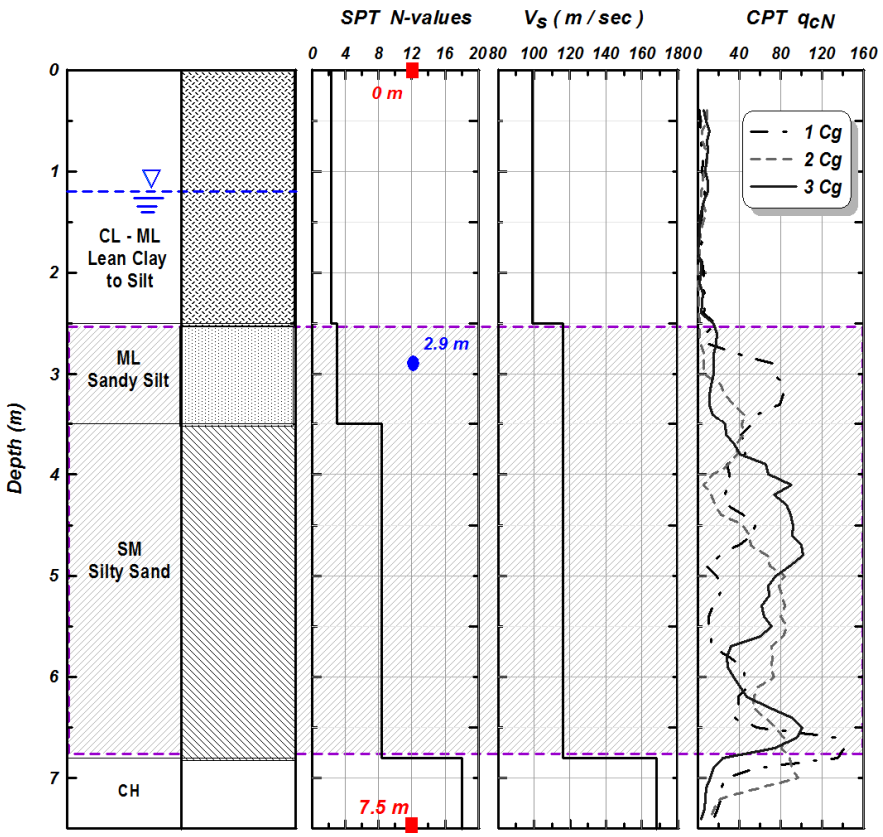

Figure 4.2: Soil profile for WLA site showing SPT N-values, and shear-value velocities [reproduced from Ziotopoulou et al. (2012)].

shear strength can be grossly inaccurate, which may result in significant errors for analyses involving shear stress levels at or near failure (Gingery and Elgamal, 2013).

In this study, a method proposed by Alborz Ghofrani (Personal Communication, 2016) was used to correct $G/Gmax$ curves to match the shear strength of soil at failure strain. Figure 4.3 illustrates the difference between the original Darendeli (2001) curves and the strength corrected ones. The dash line in the shear stress–strain plots depicts the shear strength of the soil obtained from laboratory tests. The figure clearly shows the original curves under-predicted the strength of the shallow layer, while in this case, it over-predicted the strength of the deep layer. The correction algorithm can smoothly transform the original curve from a desired strain to match real shear strength at large strains. In this study, the correction was applied at strain where 50% of shear strength implied by the original G/G_{max} curve was reached.

Layers 3 and 4 were modeled using the PM4Sand model. Material properties for PM4Sand are presented in Table 4.2. CRR and D_R values were adopted from Ziotopoulou (2010). G_o was computed based on V_s. Then, h_{po} was calibrated iteratively to match the targeted CRRs. All secondary parameters were kept as default values. The soil column was modeled using 15 SSPquadUP elements. *Uniform Excitation* was used to apply the

Table 4.1: Layering and material models used in OpenSees to simulate WLA site and adopted soil properties. Soil properties are adopted from Youd et al. (2004).

Layer #	Thickness (m)	Material Model	Hydraulic Conductivity(m/s)	γ_{Dry} (kN/m^3)	γ_{Sat} (kN/m^3)	OCR	PI	Su(kPa)
1	1.0	PIMY	10^{-5}	14.13	-	4	8	36.0
2	1.5	PIMY	10^{-5}	-	18.63	4	8	36.0
3	1.0	PM4Sand	10^{-4}	-	18.82			
4	3.5	PM4Sand	10^{-4}	-	18.82			
5	0.5	PIMY	10^{-5}	-	19.18	2	29	30.5

Table 4.2: Input parameters for PM4Sand for WLA.

Layer #	Material Model	$CRR_{M7.5}$	Primary Parameters		
			D_R	G_o	h_{po}
3	PM4Sand	0.115	0.38	525.0	1.2
4	PM4Sand	0.155	0.58	410.0	0.44

*All secondary input parameters were assigned the default values.

acceleration time history recorded in the downhole array. Other boundary conditions and analysis parameters were similar to those used in the 1D soil column analyses described in the verification study section.

From the simulations and comparison with field recordings, several findings are of interest. First, as indicated by the simulated pore water pressure evolution plot shown in Figure 4.5, liquefaction was triggered during this event. Figure 4.4 compares the simulated versus recorded acceleration response at the surface. Although the simulations captured the general trend of recorded acceleration response, they under-estimated the long-period components associated with post liquefaction softening and the intermittent higher frequencies associated with dilation pulses. This indicates that the material parameters should be modified to produce more dilative soil behavior than what is shown in Figure 4.6. Simulations using the original and corrected G/G_{max} curves produced similar results, as shown in Figure 4.4, indicating that the shear stress–strain behavior of those layers during this motion was still within the unaffected portion of the original curves.

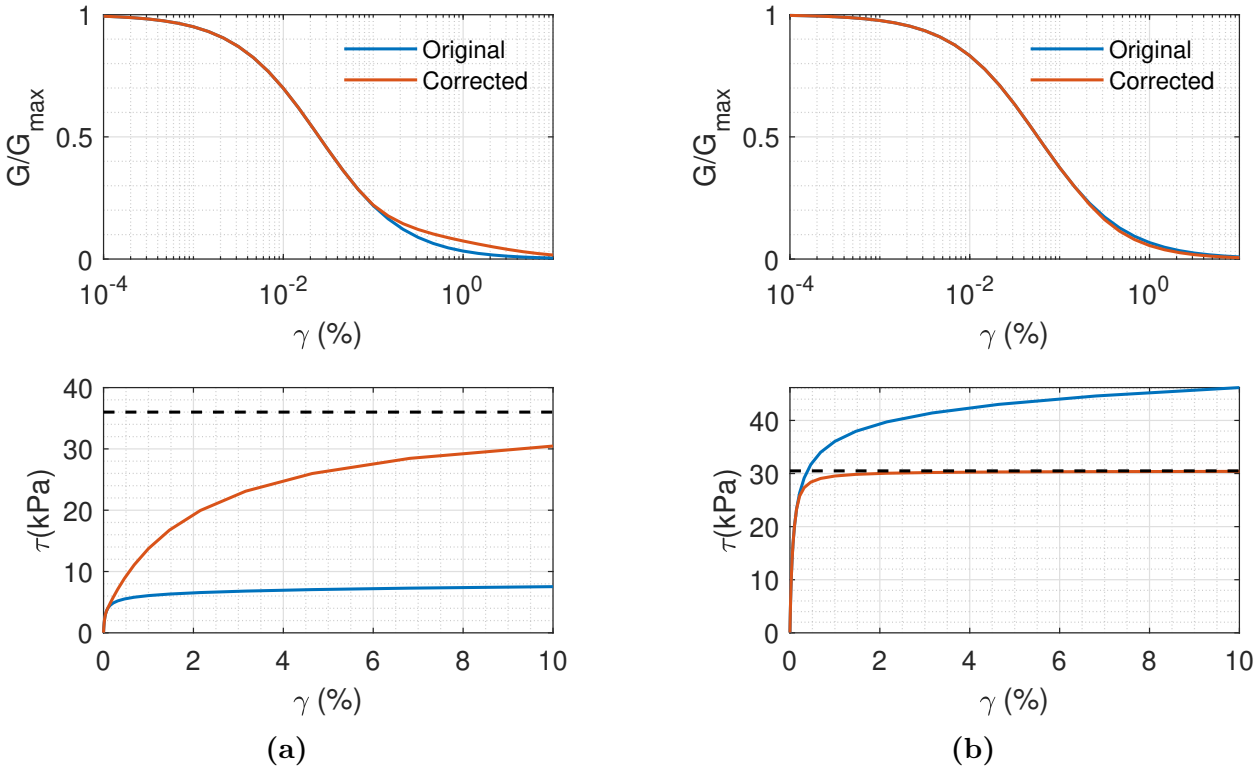

Figure 4.3: Comparison of strength corrected and original Darendeli (2001) shear modulus reduction curves and computed shear stress-shear strain curves for: (a) Layer 2 and (b) Layer 5.

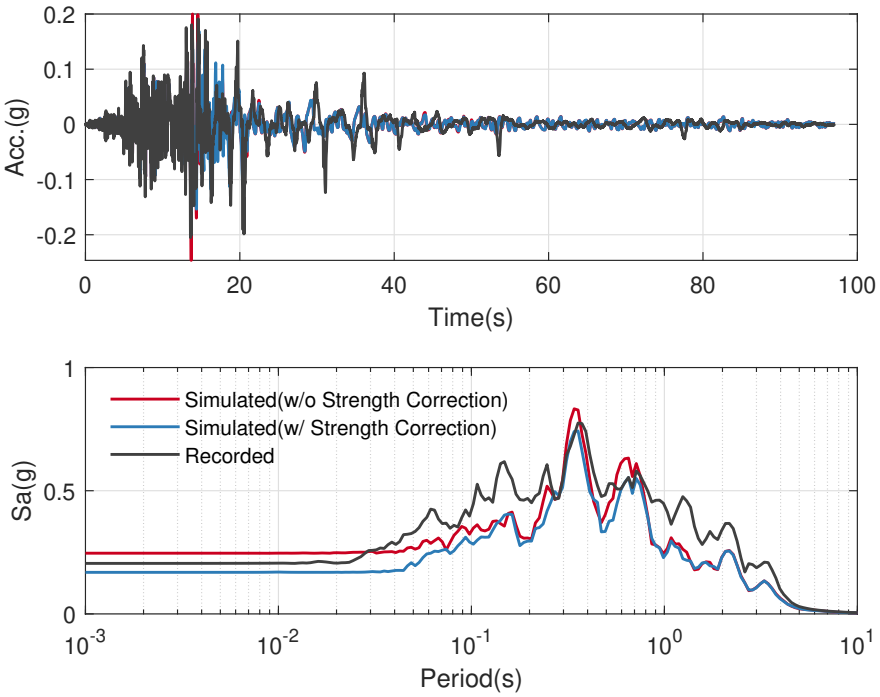

Figure 4.4: Comparison of time history and response spectra of simulated and recorded motions at surface.

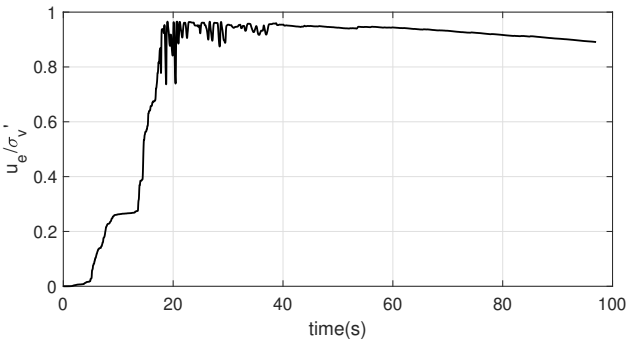

Figure 4.5: Evolution of excess pore pressure at the top of sandy silt layer.

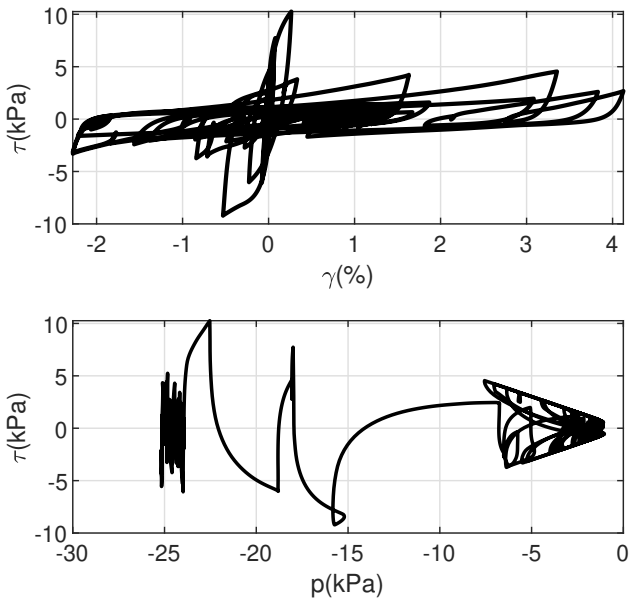

Figure 4.6: Stress–strain loop and stress path for PM4Sand model at a depth of 4 m for WLA.

4.3 SITE RESPONSE ANALYSIS OF PORT ISLAND ARRAY

The second case investigated in this study was the Port Island Array. This array is located in Kobe Port Island, Japan, which is a man-made island that suffered substantial damage during the 1995 Kobe earthquake (Hyogoken-Nambu earthquake). This array has been studied by several researchers, including (Ishihara et al., 1996; Cubrinovski et al., 1996, 1999; **?**; Ziotopoulou et al., 2012). The array consists of four sets of strong-motion accelerometers positioned at the ground surface at depths of 16, 32, and 83 m (Cubrinovski et al., 1996). Unlike the WLA, no piezometers have been installed. Shown in Figure 4.7, the soil profile consists of roughly five layers: a 18-m-thick reclaimed Masado soil (well-graded and containing a fairly large portion of gravel) at surface, a 10-m-thick alluvial clay layer, a 9-m-thick alluvial gravelly sand layer, a 22-m-thick diluvial gravelly sand layer, and a 22-m-thick diluvial clay layer. The water table oscillates at around a depth of approximately 3 m.

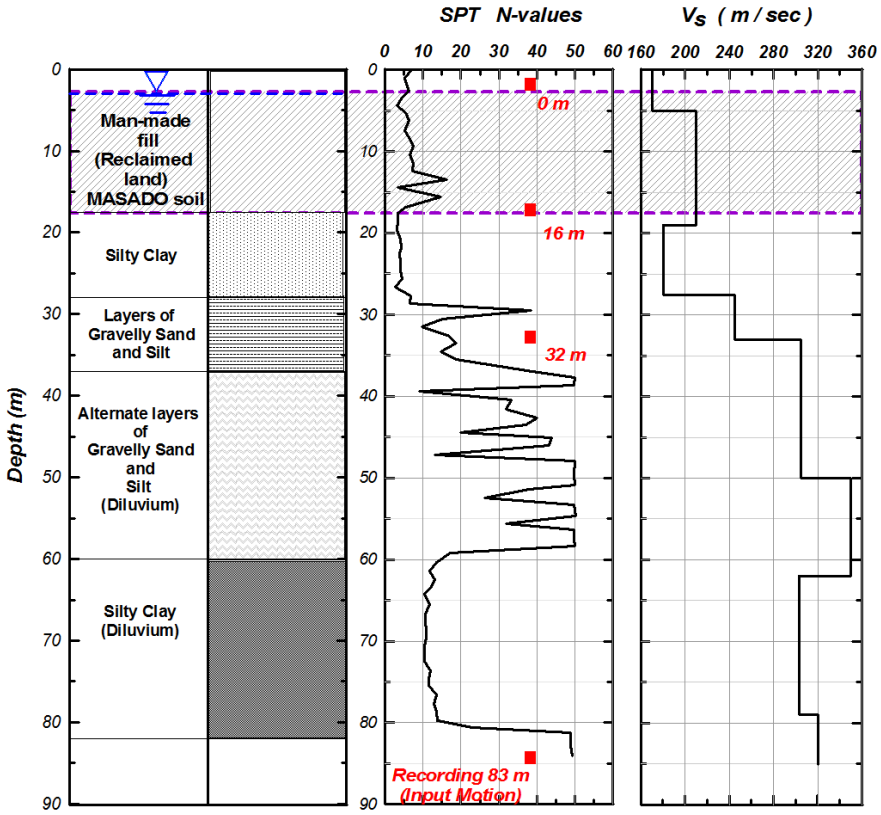

Figure 4.7: Soil profile for the Port Island site showing SPT N-values and shear-wave velocities [reproduced from Ziotopoulou et al. (2012)].

The Kobe earthquake triggered massive liquefaction in the area of this site, resulting in settlements and sand boils. Figure 4.8 illustrates the NS horizontal acceleration recorded by the downhole arrays. The records show the evolution of frequency content, possibly due to softening of soils during strong shaking.

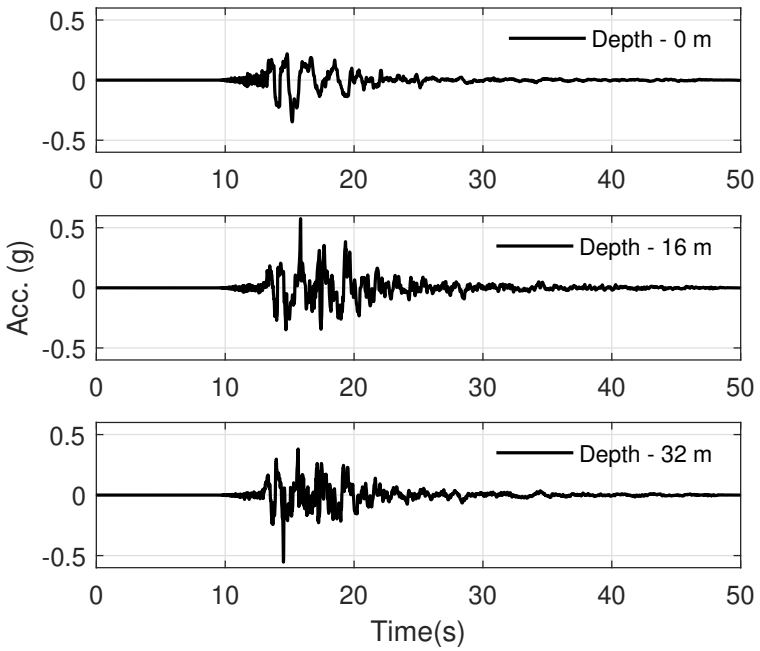

Figure 4.8: Recorded N-S horizontal acceleration time histories at various depths for Port Island Array.

Only the top 32 m of this profile was simulated in this study. Thus the motion recorded at 32 m in the downhole was applied as a within motion using the *Uniform Excitation* pattern in OpenSees. For modeling purposes, the profile was divided into 6 sublayers: see Table 4.3. The soil column was modeled using a total of 64 SSPquadUP elements with average size of 0.5 m. The material properties for PM4Sand was adopted from Ziotopoulou et al. (2012) and are listed in Table 4.4.

Table 4.3: Layering and material models used in OpenSees to simulate Port Island Array and adopted soil properties.

Layer #	Thickness(m)	Material Model	Hydraulic Conductivity(m/sec)
1	3.0	PM4Sand	10^{-4}
2	2.0	PM4Sand	10^{-4}
3	9.0	PM4Sand	10^{-4}
4	3.5	PM4Sand	10^{-4}
5	10.5	PM4Silt	10^{-6}
6	4.0	PM4Silt	10^{-6}

The silty clay and top of the gravelly sand and silt layer were expected to show clay-like behavior; therefore, the PM4Silt model was used, which is a 2D plastic material developed to represent clay-like behavior (Boulanger and Idriss, 2006) for earthquake engineering applications (Boulanger and Ziotopoulou, 2018). This model has also been implemented in

OpenSees and is presented in Chen (2020). Like PM4Sand, PM4Silt uses a set of primary parameters (namely undrained strength S_u or undrained strength ratio S_u/σ'_v, shear-modulus coefficient G_o, and contraction-rate parameter h_{po}) and optional secondary parameters whose predefined default values are related to the soil state. In this study, G_o was calculated from measured shear-wave velocity values at this site; see Figure 4.7. The other two primary parameters were selected for medium and stiff clays, respectively, based on SPT blow counts; see Table 4.4.

Table 4.4: Input parameters for PM4Sand for the Port Island Array.

Layer #	Material Model	Primary Parameters			
		D_R	S_u/σ'_v	G_o	h_{po}
1	PM4Sand	0.47		729.0	0.7
2	PM4Sand	0.47		729.0	0.7
3	PM4Sand	0.39		695.51	0.8
4	PM4Sand	0.47		507.53	0.9
5	PM4Silt		0.5	465.0	50.0
6	PM4Silt		0.75	686.0	60.0

*All secondary input parameters were assigned the default values.

Figure 4.9 illustrates the simulated soil behavior obtained using PM4Sand at a depth of 10 m. As indicated by the pore water pressure evolution plot, liquefaction was triggered at around 14 sec, and PM4Sand captured the general behavior of the sand and liquefaction triggered by the earthquake. Figures 4.10 and 4.11 compare the simulated versus the recorded acceleration response at the surface and a depth of 16 m, respectively. The simulations were able to capture the general trend of recorded acceleration response.

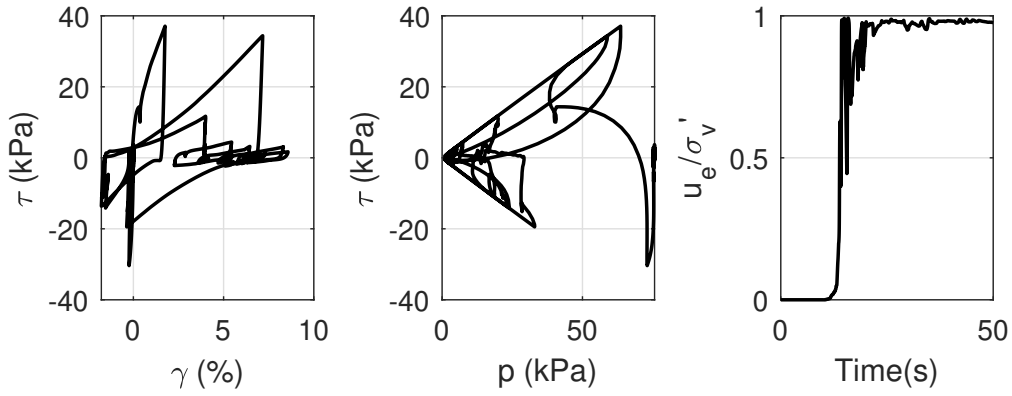

Figure 4.9: Stress–strain loop, stress path, and excess pore-pressure evolution at the depth of 10 m obtained using PM4Sand.

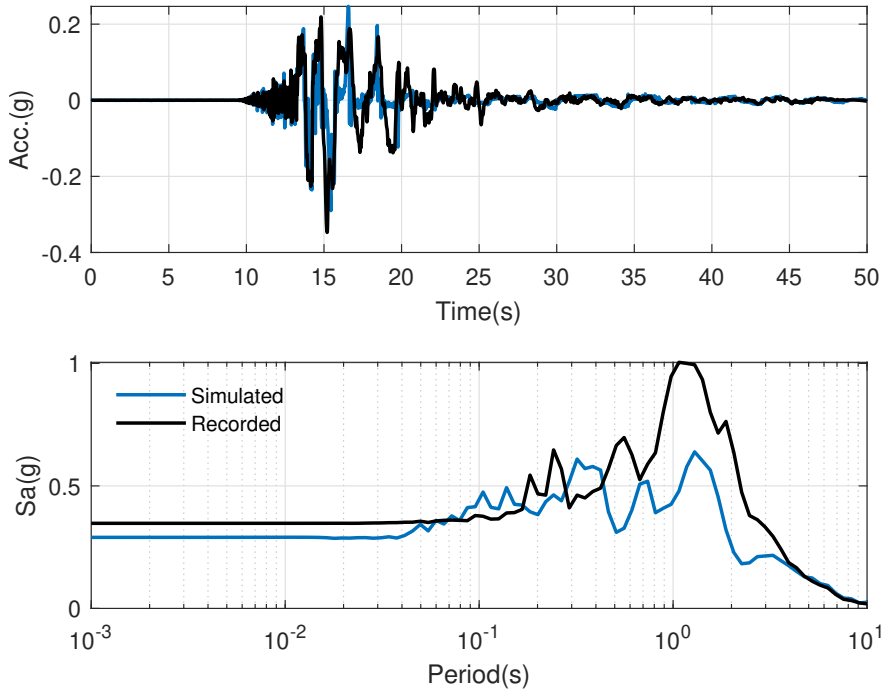

Figure 4.10: Comparison of acceleration time history and response spectra of simulated and recorded motions at the surface.

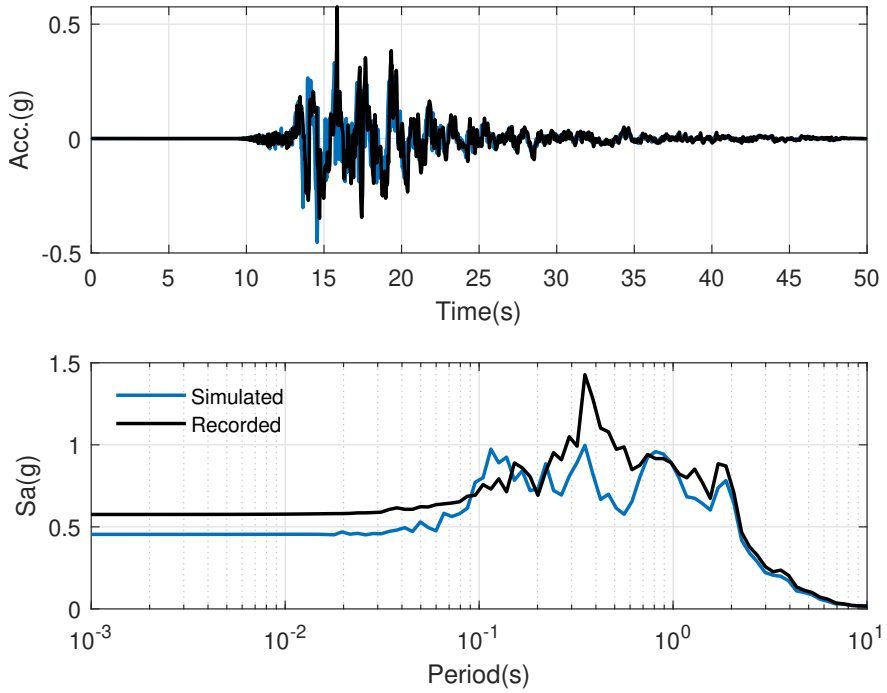

Figure 4.11: Comparison of acceleration time history and response spectra of simulated and recorded motions at a depth of 16 m.

4.4 SUMMARY

This chapter presented a series of validation studies for PM4Sand, including a 1D analysis of two liquefaction array case histories: the Wildlife Liquefaction Array and the Port Island Array. These studies illustrate capabilities and limitations of the simulation of liquefaction sites using PM4Sand. The results obtained using PM4Sand for the liquefiable layers provided realistic and reasonable responses for all three cases with limited soil information. Based on the results, further refinement of input parameters are warranted for better predictions.

5 Summary and Conclusions

This report documents the implementation, verification, validation, and application of an advanced bounding surface constitutive model, PM4Sand, in the OpenSees finite-element method (FEM) framework. It includes a brief introduction to the PM4Sand model and details about its implementation in OpenSees. A series of verification studies performed at different levels is also presented. The report ends with a validation study performed using one-dimensional (1D) case histories.

Implementation details on PM4Sand's includes bounding surface and yield surface stress correction strategies and several different integration schemes, e.g., modified Euler method with automatic error control. The implementation was optimized for performance and parallel computing. Thus, it can be used in large-scale numerical analyses using high-performance computing (HPC) systems.

To improve understanding of PM4Sand's behavior under a large-range of parameters, a parametric study was conducted. A correlation was proposed for h_{po} for a given combination of D_R, G_o, and CRR to speed up the calibration process when calibration has to be performed for each soil unit in a profile that shows large geological variability. The slope of the CRR curve, b, obtained using PM4Sand, was also presented and was shown to be representative for clean sands. The correlation appeared to be very useful for calibration purposes despite some limitation in representing dense sand behavior, and problems in capturing the response observed in undrained CDSS tests performed on Ottawa F-65 sand (Bastidas, 2016) that showed b values that are less than what would be expected. This showed the limitation of calibrating for primary parameters only.

The purpose of the verification study of the PM4Sand model and implemented in OpenSees was to (1) identify and remove programming errors in computer codes and (2) verify numerical algorithms. The goal of this verification phase was to ensure OpenSees produced comparative results as the model's original implementation in FLAC. This was challenging since comparisons were between responses obtained using different numerical tools and systems, i.e., finite-element method (FEM) vs. the finite-difference method (FDM). To address this issue, a series of stress point, single element, and 1D soil column analyses were performed such that system complexity was gradually increased and results were carefully examined to identify any inconsistency. The results showed that, despite discrepancies due to platform differences, i.e., FEM vs. FDM, and different model discretization, OpenSees produced consistent results compared to both FLAC and PLAXIS.

Finally, the validation study on PM4Sand included two 1D analyses of liquefaction array case histories, including the Wildlife Array (WLA) and Port Island Array. Simulations using PM4Sand in OpenSees were able to reproduce field observations. The verification and validation studies presented in this report, together with the corresponding validation studies using LEAP centrifuge experiments by the authors, demonstrate that the PM4Sand model implemented in OpenSees can be used in nonlinear dynamic effective stress analysis with confidence.

REFERENCES

Adams, B. M., Ebeida, M. S., Eldred, M. S., Jakeman, J. D., Swiler, L. P., and Eddy, J. P. (2017). "Dakota, a multilevel parallel object-oriented framework for design optimization, parameter estimation, uncertainty quantification, and sensitivity analysis: Version 6.7 reference manual.." *Report No. SAND2014-5015*, Sandia National Laboratories, Albuquerque, NM.

Alawaji, H., Runesson, K., Sture, S., and Axelsson, K. (1992). "Implicit integration in soil plasticity under mixed control for drained and undrained response." *International journal for numerical and analytical methods in geomechanics*, 16(10), 737–756.

Andrus, R. D. and Stokoe, K. H. (2000). "Liquefaction resistance of soils from shear wave velocity." *Journal of Geotechnical and Geoenvironmental Engineering*, 126(11), 1015–1025.

Armstrong, R. J., Boulanger, R. W., and Beaty, M. H. (2013). "Liquefaction effects on piled bridge abutments: Centrifuge tests and numerical analyses." *Journal of Geotechnical and Geoenvironmental Engineering*, 139(3), 433–443.

Bastidas, A. M. P. (2016). "Ottawa F-65 sand characterization," PhD thesis, University of California, Davis.

Bolton, M. D. (1986). "The strength and dilatancy of sands." *Géotechnique*, 36(1), 65–78.

Boulanger, R. W. and Idriss, I. M. (2004). "State normalization of penetration resistance and the effect of overburden stress on liquefaction resistance." *11th International Conference on Soil Dynamics and Earthquake Engineering, and 3rd International Conference on Earthquake Geotechnical Engineering*, University of California, Berkeley.

Boulanger, R. W. and Idriss, I. M. (2006). "Liquefaction susceptibility criteria for silts and clays." *Journal of Geotechnical and Geoenvironmental Engineering*, 132(11), 1413–1426.

Boulanger, R. W. and Ziotopoulou, K. (2015). "PM4Sand (Version 3): a sand plasticity model for earthquake engineering applications." *Report No. UCD/CGM-15/01*, Center for Geotechnical Modeling, University of California at Davis.

Boulanger, R. W. and Ziotopoulou, K. (2017). "PM4Sand (Version 3.1): a sand plasticity model for earthquake engineering applications." *Report No. UCD/CGM-17/01*, Center for Geotechnical Modeling, University of California at Davis.

Boulanger, R. W. and Ziotopoulou, K. (2018). "PM4SILT (Version 1): a silt plasticity model for earthquake engineering applications." *Report No. UCD/CGM-18/01*, Center for Geotechnical Modeling, University of California at Davis.

Cetin, K. O., Tokimatsu, K., Harder, L. F., Moss, R. E. S., Kayen, R. E., Der Kiureghian, A., and Seed, R. B. (2004). "Standard penetration test-based probabilistic and deterministic assessment of seismic soil liquefaction potential." *Journal of Geotechnical and Geoenvironmental Engineering*, 130(12), 1314–1340.

Chen, L. (2020). "Implementation, verification, validation, and application of two constitutive models for earthquake engineering applications," PhD thesis, University of Washington.

Chen, L., Ghofrani, A., and Arduino, P. (2019). "Prediction of LEAP-UCD-2017 centrifuge test results using two advanced plasticity sand models." *Model Tests and Numerical Simulations of Liquefaction and Lateral Spreading: LEAP-UCD-2017*, B. L. Kutter, M. Manzari, and M. Zeghal, eds. Springer, 405–420.

Cubrinovski, M., Ishihara, K., and Furukawazono, K. (1999). "Analysis of two case histories on liquefaction of reclaimed deposits." *Proceedings of the Twelfth World Conference on Earthquake Engineering*, Auckland, New Zealand.

Cubrinovski, M., Ishihara, K., and Tanizawa, F. (1996). "Numerical simulation of the Kobe Port Island liquefaction." *Eleventh World Conference on Earthquake Engineering*, number 330, Acapulco, Mexico.

Dafalias, Y. (1986). "Bounding surface plasticity. i: mathematical foundation and hypoplasticity." *Journal of Engineering Mechanics*, 112(9), 966–987.

Dafalias, Y. F. and Manzari, M. T. (2004). "Simple plasticity sand model accounting for fabric change effects." *Journal of Engineering Mechanics*, 130(6), 622–634.

Darendeli, M. B. (2001). "Development of a new family of normalized modulus reduction and material damping curves," PhD thesis, University of Texas at Austin.

Dowell, M. and Jarratt, P. (1972). "The "pegasus" method for computing the root of an equation." *BIT Numerical Mathematics*, 12(4), 503–508.

EduPro Civil Systems, I. (2017). *ProShake*. `http://www.proshake.com/`. EduPro Civil Systems, Inc., Sammamish, WA.

Ghofrani, A. (2018). "Development of numerical tools for the evaluation of pile response to laterally spreading soil," PhD thesis, University of Washington.

Gingery, J. R. and Elgamal, A. (2013). "Shear stress-strain curves based on the G/G_{max} logic: A procedure for strength compatibility." *IACGE 2013: Challenges and Recent Advances in Geotechnical and Seismic Research and Practices*. 721–729.

Hashash, Y., Musgrove, M., Harmon, J., Groholski, D., Phillips, C., and Park, D. (2016). *DEEPSOIL 6.1, User Manual*. `http://deepsoil.cee.illinois.edu/`. Board of Trustees of University of Illinois at Urbana-Champaign, Urbana, IL.

Holzer, T. L. and Youd, T. L. (2007). "Liquefaction, ground oscillation, and soil deformation at the wildlife array, california." *Bulletin of the Seismological Society of America*, 97, 961–976.

Howell, R., Rathje, E. M., and Boulanger, R. W. (2014). "Evaluation of simulation models of lateral spread sites treated with prefabricated vertical drains." *Journal of Geotechnical and Geoenvironmental Engineering*.

Idriss, I. M. and Boulanger, R. W. (2008). *Soil liquefaction during earthquakes*. MNO-12. Earthquake Engineering Research Institute, Oakland, Calif.

Ishihara, K. (1993). "Liquefaction and flow failure during earthquakes." *Géotechnique*, 43(3), 351–451.

Ishihara, K., Yasuda, S., and Nagase, H. (1996). "Soil characteristics and ground damage." *soils and foundations*, 109–118.

Itasca (2016). *FLAC - Fast Lagrangian Analysis of Continua, Version 8.0*. Itasca Consulting Group, Inc., Minneapolis, Minnesota.

Kramer, S. L. (1996). *Geotechnical Earthquake Engineering*. Pearson.

Kramer, S. L., Sideras, S. S., Greenfield, M., and Hushmand, B. (2018). "Liquefaction, ground motions, and pore pressures at the wildlife liquefaction array in the 1987 superstition hills earthquake." *Geotechnical Earthquake Engineering and Soil Dynamics V*. 384–402.

Kwok, A. O. L., Stewart, J. P., Hashash, Y. M. a., Matasovic, N., Pyke, R., Wang, Z., and Yang, Z. (2007). "Use of exact solutions of wave propagation problems to guide implementation of nonlinear seismic ground response analysis procedures." *Journal of Geotechnical and Geoenvironmental Engineering*, 133(11), 1385–1398.

Lysmer, J. and Kuhlemeyer, A. M. (1969). "Finite dynamic model for infinite media." *Journal of the Engineering Mechanics Division, ASCE*, 95, 859–877.

McGann, C. R., Arduino, P., and Mackenzie-Helnwein, P. (2012). "Stabilized single-point 4-node quadrilateral element for dynamic analysis of fluid saturated porous media." *Acta Geotechnica*, 7(4), 297–311.

McGann, C. R., Arduino, P., and Mackenzie-Helnwein, P. (2015). "A stabilized single-point finite element formulation for three-dimensional dynamic analysis of saturated soils." *Computers and Geotechnics*, 66(0), 126–141.

McKenna, F., Padhye, N., Wang, C., Mackenzie-Helnwein, P., and Gardner, M. (2018). *NHERI-SimCenter/uqFEM: Release V1.1.0*.

Menq, F.-Y. (2003). "Dynamic properties of sandy and gravelly soils," PhD thesis, The University of Texas at Austin.

Montgomery, J. (2012). "Issues in nonlinear deformation analyses of embankment dams affected by liquefaction," PhD thesis, University of California Davis.

Montgomery, J. and Boulanger, R. W. (2017). "Effects of spatial variability on liquefaction-induced settlement and lateral spreading." *Journal of Geotechnical and Geoenvironmental Engineering*, 143(1), 04016086.

Moss, R. E., Seed, R. B., Kayen, R. E., Stewart, J. P., Der Kiureghian, A., and Cetin, K. O. (2006). "CPT-based probabilistic and deterministic assessment of in situ seismic soil liquefaction potential." *Journal of Geotechnical and Geoenvironmental Engineering*, 132(8), 1032–1051.

Muir Wood, D. (1990). *Soil Behaviour and Critical State Soil Mechanics*. Cambridge University Press.

OpenSees (2007). *Open System for Earthquake Engineering Simulation*. `http://opensees.berkeley.edu`. Pacific Earthquake Engineering Research Center (PEER), University of California, Berkeley.

Plaxis.B.V (2018). *PLAXIS 2D*. `https://www.plaxis.com/product/plaxis-2d/`. Plaxis.B.V, Delft, Netherlands.

Potts, D. M. and Gens, A. (1985). "A critical assessment of methods of correcting for drift from the yield surface in elasto-plastic finite element analysis." *International Journal for Numerical and Analytical Methods in Geomechanics*, 9(2), 149–159.

Ramos, A. (2010). "Instabilities in sands," PhD thesis, Universidad de los Andes.

Rathje, E., Clint, D., E., P. J., Jean-Paul, P., Dan, S., Ashley, A., Pedro, A., J., B. S., Tim, C., Charlie, D., Maria, E., L., H. F., Matthew, H., Ahsan, K., Laura, L., Stephen, M., and Gilberto, M. (2017). "Designsafe: New cyberinfrastructure for natural hazards engineering." *Natural Hazards Review*, 18(3), 6017001.

Robertson, P. K. (1991). "Soil classification using the cone penetration test." *Canadian Geotechnical Journal*, 28(1), 176–178.

Robertson, P. K. and Wride, C. (1998). "Evaluating cyclic liquefaction potential using the cone penetration test." *Canadian Geotechnical Journal*, 35(3), 442–459.

Schofield, A. and Wroth, C. (1968). "Critical state soil mechanics." *Soil Use and Management*, 228.

Seed, H. B. and Idriss, I. M. (1971). "Simplified procedure for evaluating soil liquefaction potential." *ASCE J Soil Mech Found Div*, 97(9), 1249–1273.

Sideras, S. S. (2011). "Response of liquefiable soil deposits to earthquake loading". Master's thesis, University of Washington, Seattle, WA.

Sloan, S. W., Abbo, A. J., and Sheng, D. (2001). "Refined explicit integration of elastoplastic models with automatic error control." *Engineering Computations*, 18(1/2), 121–194.

Taiebat, M., Jeremić, B., Dafalias, Y. F., Kaynia, A. M., and Cheng, Z. (2010). "Propagation of seismic waves through liquefied soils." *Soil Dynamics and Earthquake Engineering*, 30(4), 236–257.

Vilhar, G., Laera, A., Foria, F., Gupta, A., and Brinkgreve, R. (2018). "Implementation, validation and application of PM4Sand model in PLAXIS." *Geotechnical Earthquake Engineering and Soil Dynamics V*. 200–211.

Yang, Z., Elgamal, A., and Parra, E. (2003). "Computational model for cyclic mobility and associated shear deformation." *Journal of Geotechnical and Geoenvironmental Engineering*, 129(12), 1119–1127.

Youd, T. L., Bartholomew, H. A. J., and Proctor, J. S. (2004). "Geotechnical logs and data from permanently instrumented field sites: Garner Valley Downhole Array (GVDA) and Wildlife Liquefaction Array (WLA)." *Report no.*, Brigham Young University.

Youd, T. L. and Idriss, I. M. (2001). "Liquefaction resistance of soils: Summary report from the 1996 nceer and 1998 nceer/nsf workshops on evaluation of liquefaction resistance of soils." *Journal of Geotechnical and Geoenvironmental Engineering*, 127(4), 297–313.

Ziotopoulou, K. (2010). "Evaluating model uncertainty against strong motion records at liquefiable sites. Master's thesis, University of California, Davis, Davis, CA.

Ziotopoulou, K. (2017). "Seismic response of liquefiable sloping ground: Class A and C numerical predictions of centrifuge model responses." *Soil Dynamics and Earthquake Engineering*.

Ziotopoulou, K. and Boulanger, R. W. (2013). "Calibration and implementation of a sand plasticity plane-strain model for earthquake engineering applications." *Soil Dynamics and Earthquake Engineering*, 53, 268–280.

Ziotopoulou, K., Boulanger, R. W., and Kramer, S. L. (2012). "Site response analysis of liquefying sites." *Geo-Congress 2012: State of the art and practice in Geotechnical engineering*, number March 2012. 1799–1808.

Appendix A: Additional Verification Results

A.1 N5T3

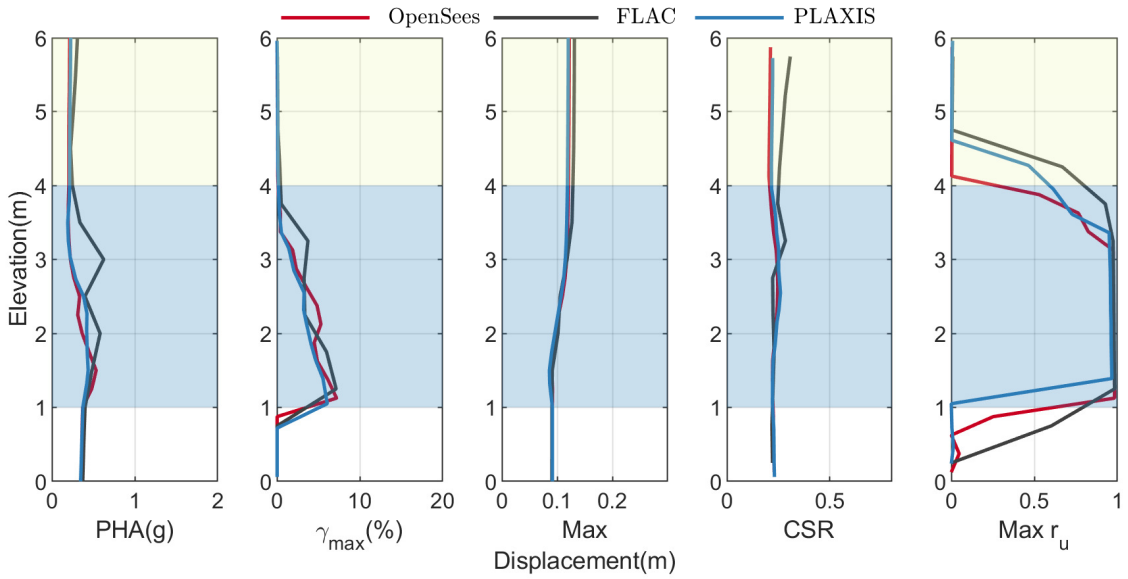

Figure A.1: Comparison of profile of PHA, γ_{max}, maximum displacement, CSR, and max r_u obtained using OpenSees, FLAC, and PLAXIS for motion RSN766.

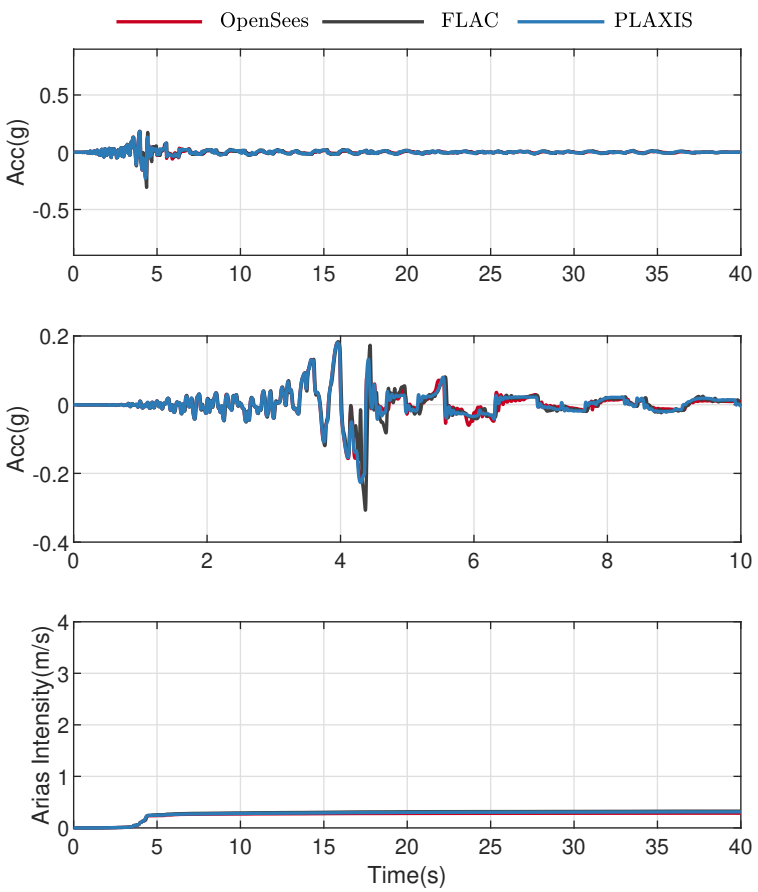

Figure A.2: Comparison of acceleration time histories at surface obtained using OpenSees, FLAC, and PLAXIS for motion RSN766.

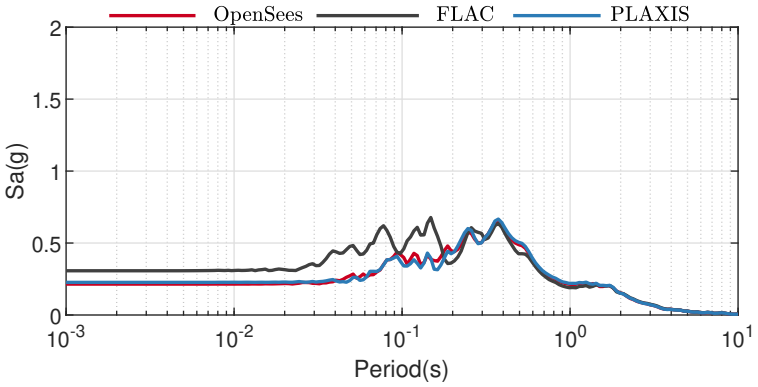

Figure A.3: Comparison of acceleration response spectra at surface obtained using OpenSees, FLAC, and PLAXIS for motion RSN766.

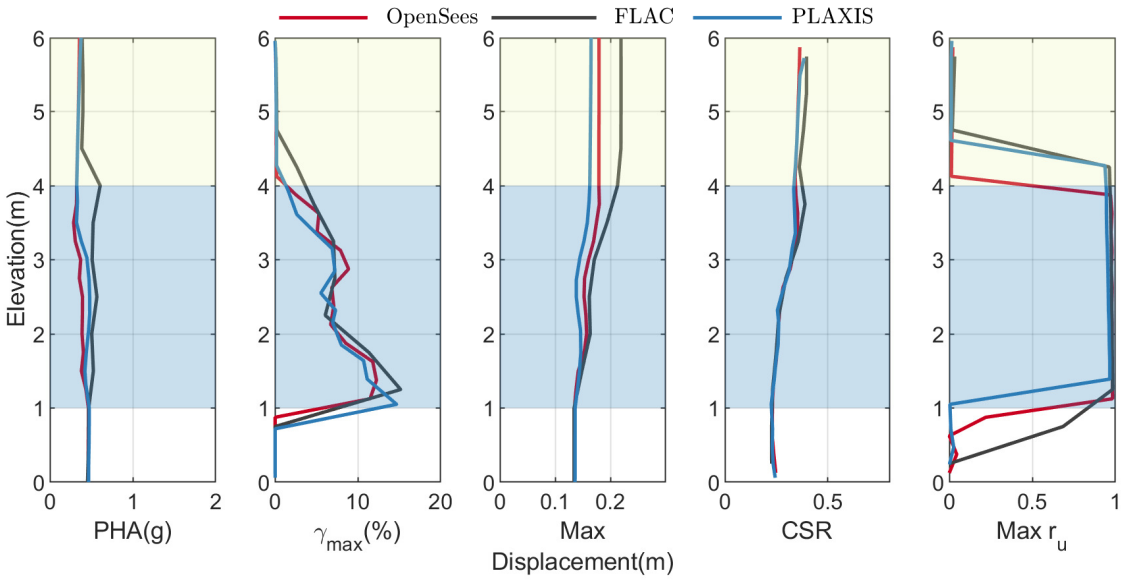

Figure A.4: Comparison of profile of PHA, γ_{max}, maximum displacement, CSR, and max r_u obtained using OpenSees, FLAC, and PLAXIS for motion RSN963.

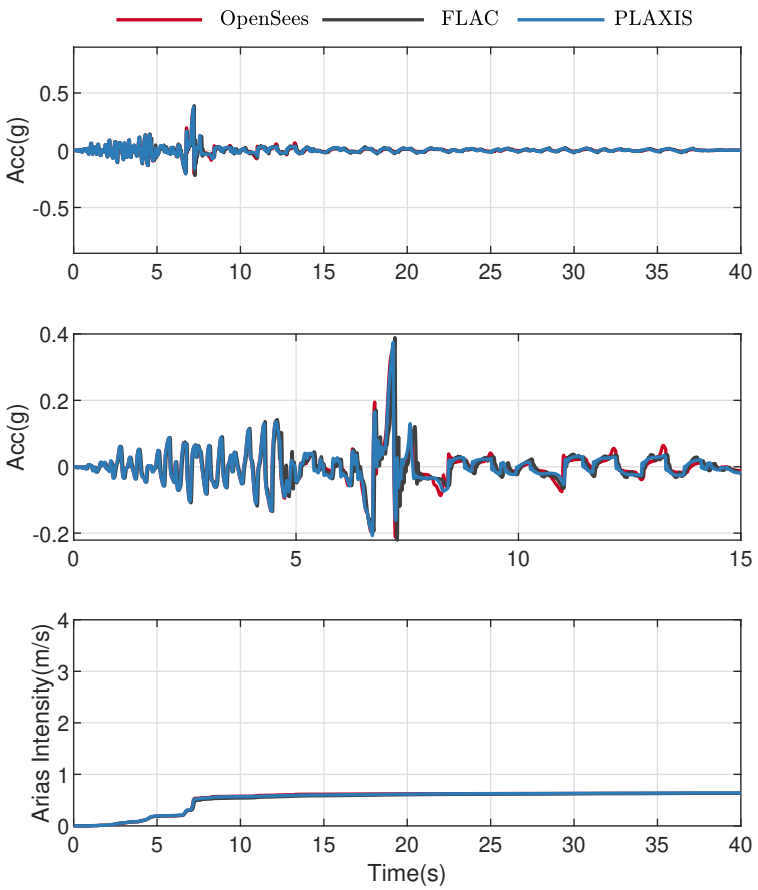

Figure A.5: Comparison of acceleration time histories at surface obtained using OpenSees, FLAC, and PLAXIS for motion RSN963.

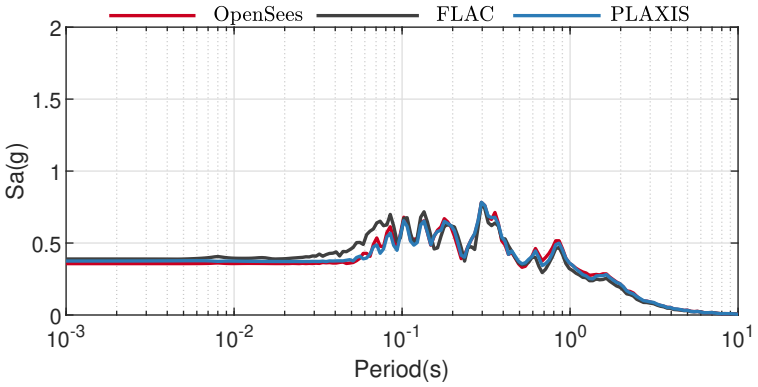

Figure A.6: Comparison of acceleration response spectra at surface obtained using OpenSees, FLAC, and PLAXIS for motion RSN963.

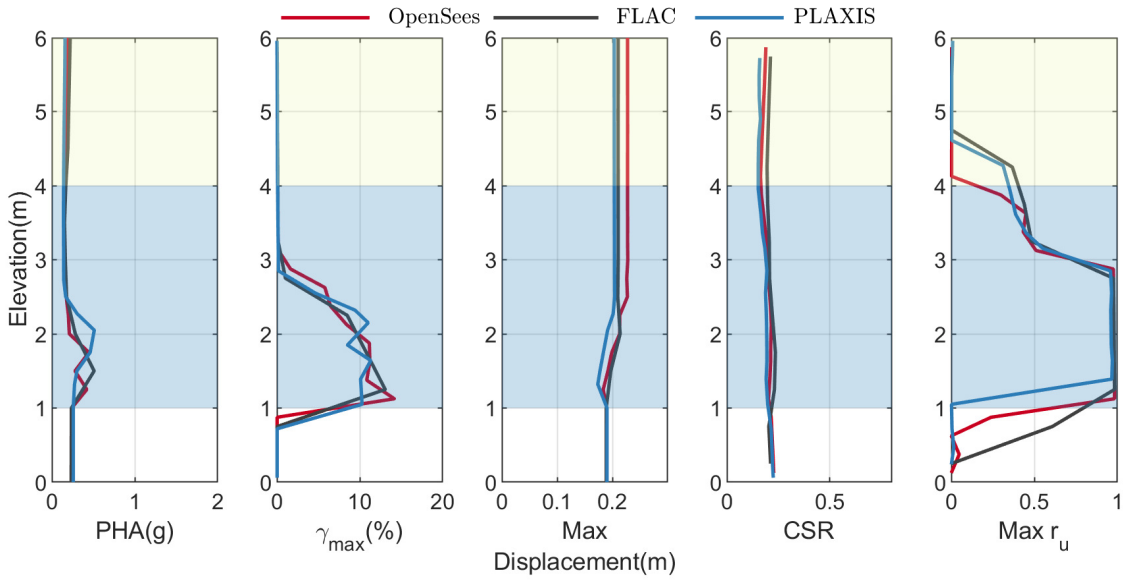

Figure A.7: Comparison of profile of PHA, γ_{max}, maximum displacement, CSR, and max r_u obtained using OpenSees, FLAC, and PLAXIS for motion RSN1203.

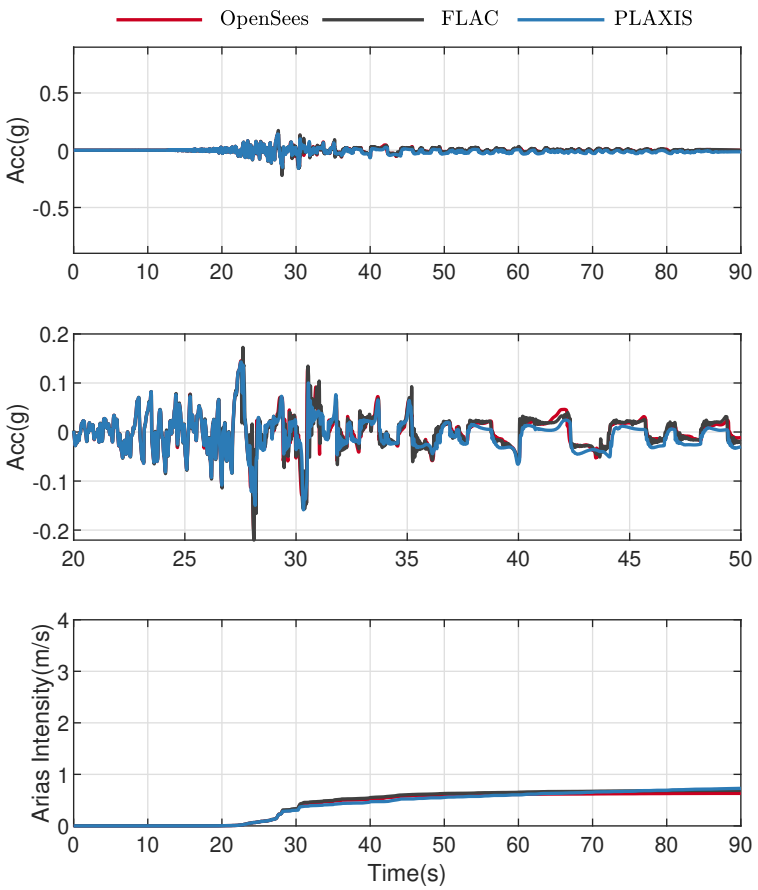

Figure A.8: Comparison of acceleration time histories at surface obtained using OpenSees, FLAC, and PLAXIS for motion RSN1203.

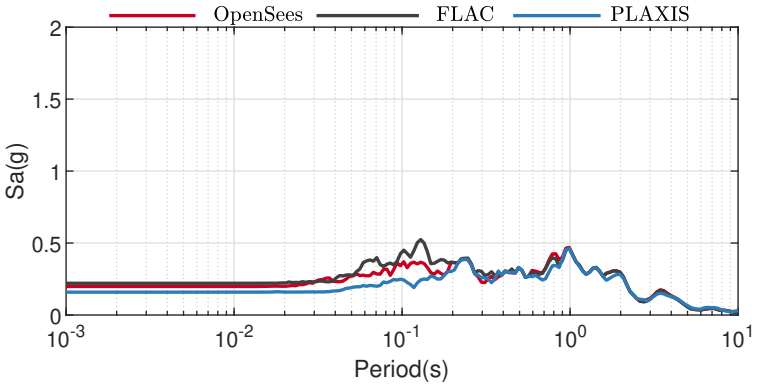

Figure A.9: Comparison of acceleration response spectra at surface obtained using OpenSees, FLAC, and PLAXIS for motion RSN1203.

A.2 N5T6

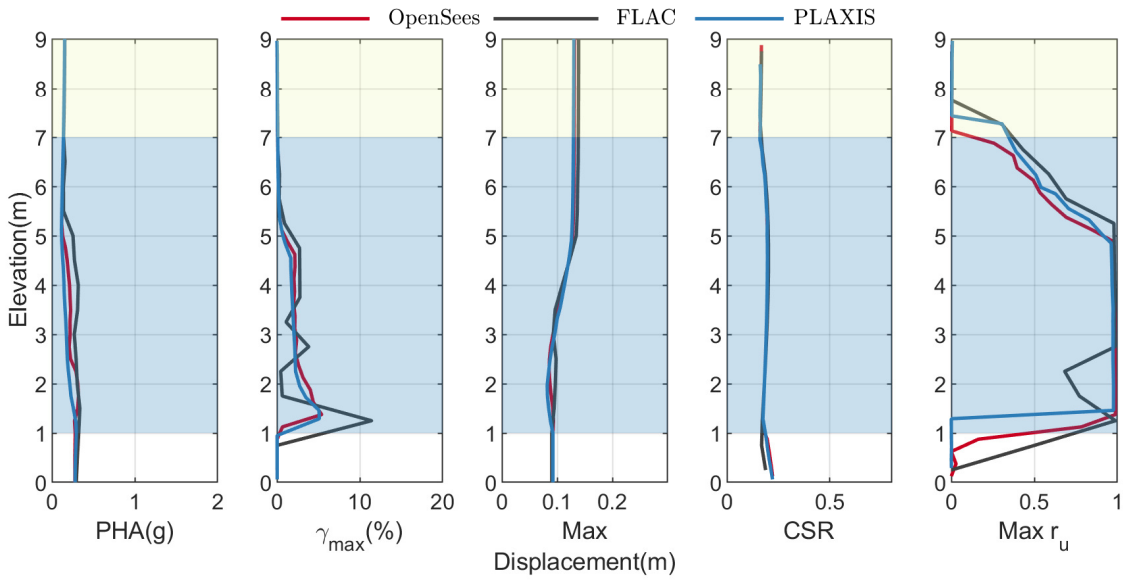

Figure A.10: Comparison of profile of PHA, γ_{max}, maximum displacement, CSR, and max r_u obtained using OpenSees, FLAC, and PLAXIS for motion RSN766.

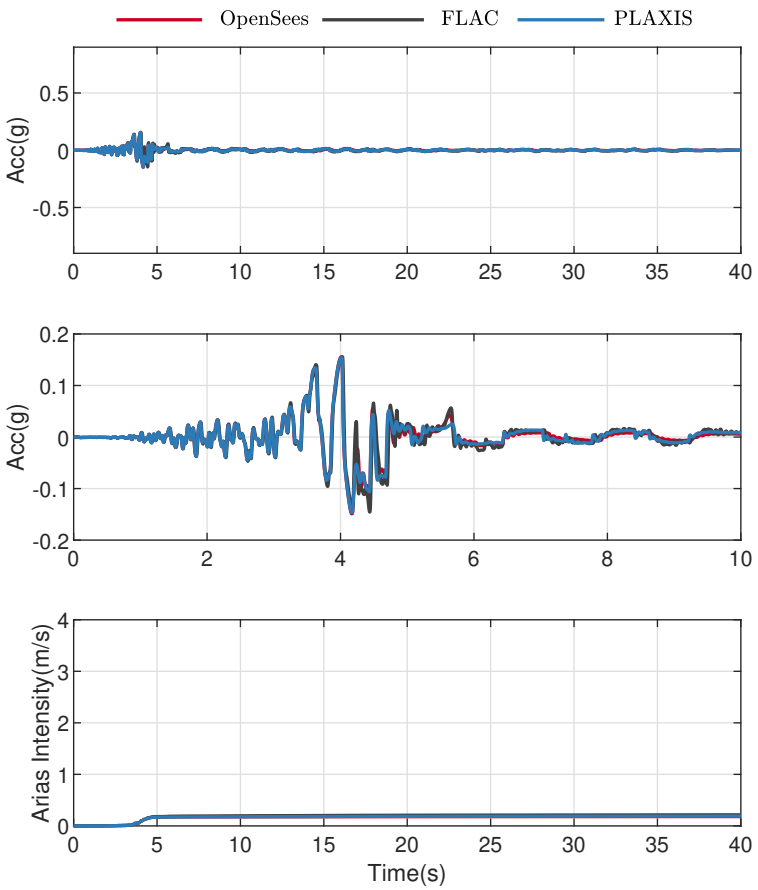

Figure A.11: Comparison of acceleration time histories at surface obtained using OpenSees, FLAC, and PLAXIS for motion RSN766.

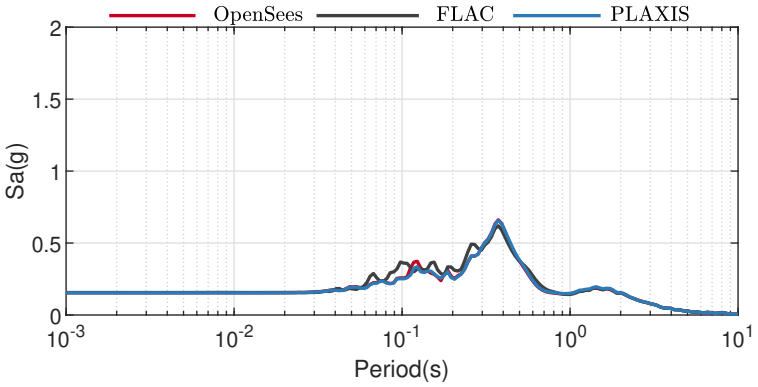

Figure A.12: Comparison of acceleration response spectra at surface obtained using OpenSees, FLAC, and PLAXIS for motion RSN766.

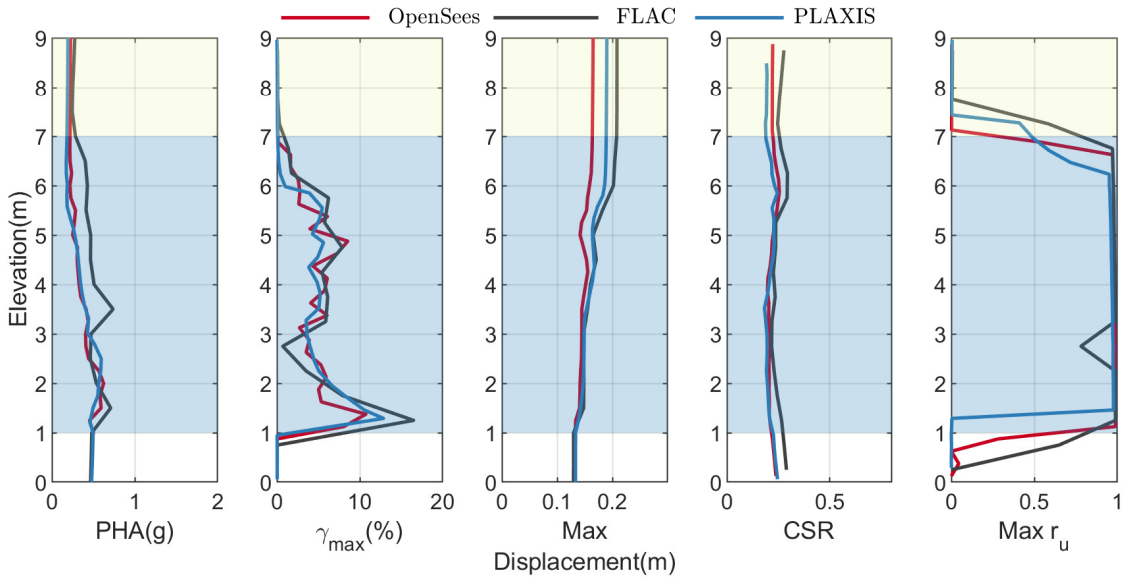

Figure A.13: Comparison of profile of PHA, γ_{max}, maximum displacement, CSR, and max r_u obtained using OpenSees, FLAC, and PLAXIS for motion RSN963.

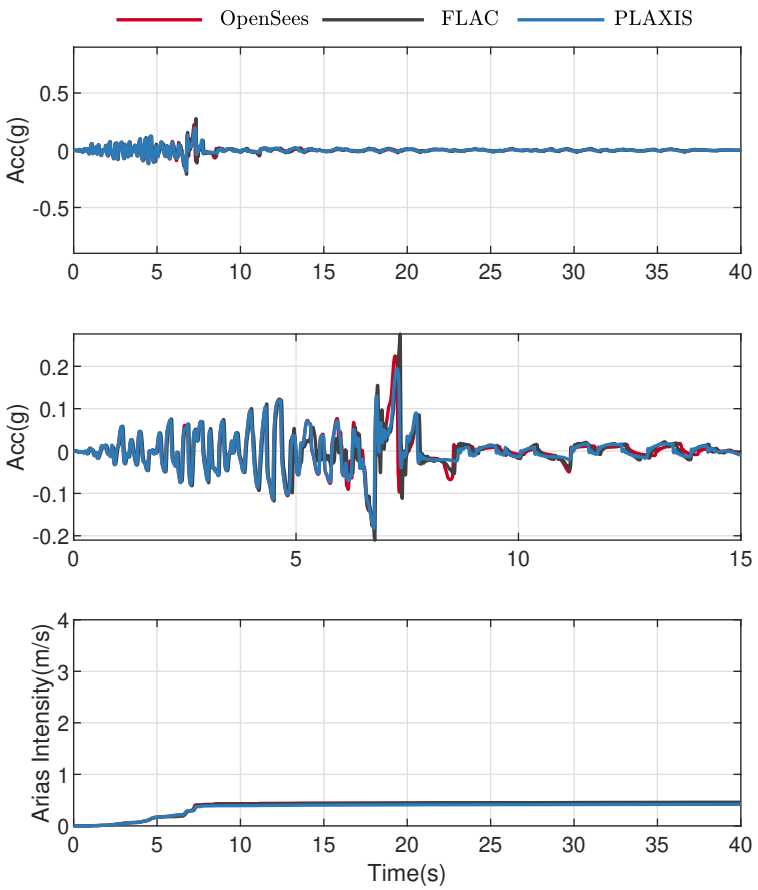

Figure A.14: Comparison of acceleration time histories at surface obtained using OpenSees, FLAC, and PLAXIS for motion RSN963.

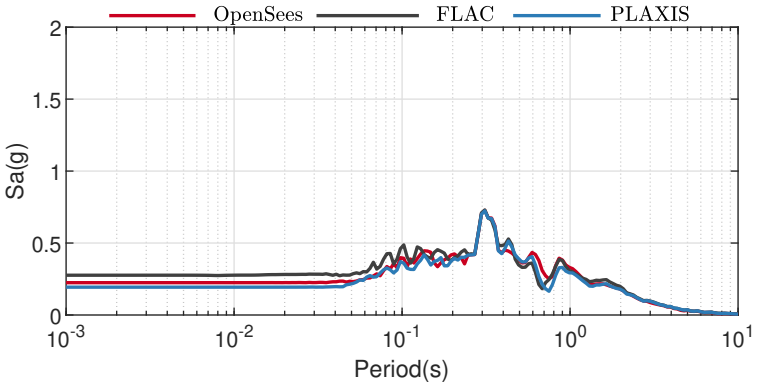

Figure A.15: Comparison of acceleration response spectra at surface obtained using OpenSees, FLAC, and PLAXIS for motion RSN963.

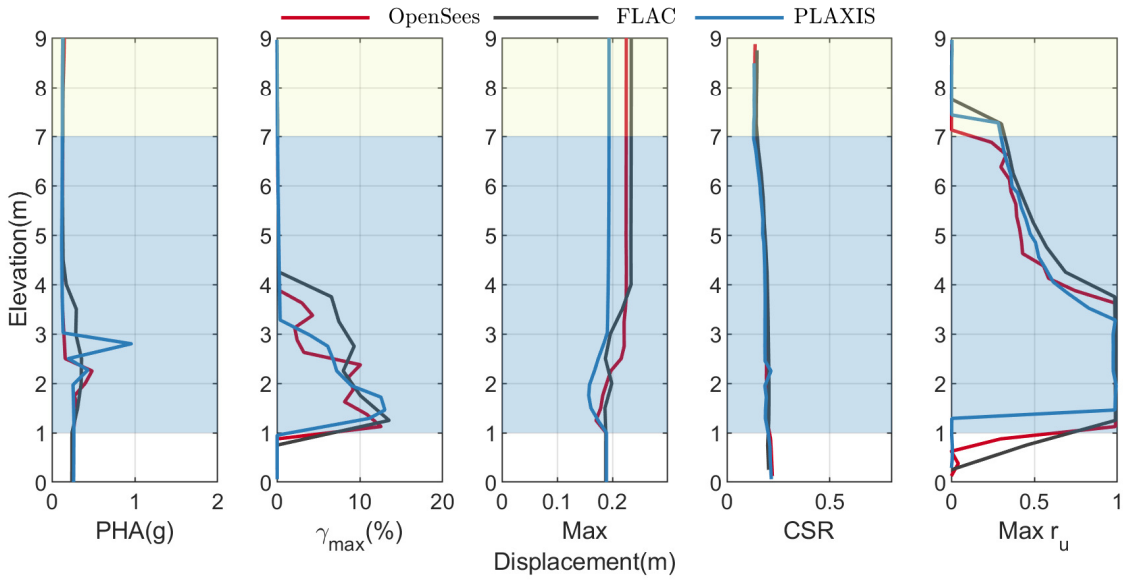

Figure A.16: Comparison of profile of PHA, γ_{max}, maximum displacement, CSR, and max r_u obtained using OpenSees, FLAC, and PLAXIS for motion RSN1203.

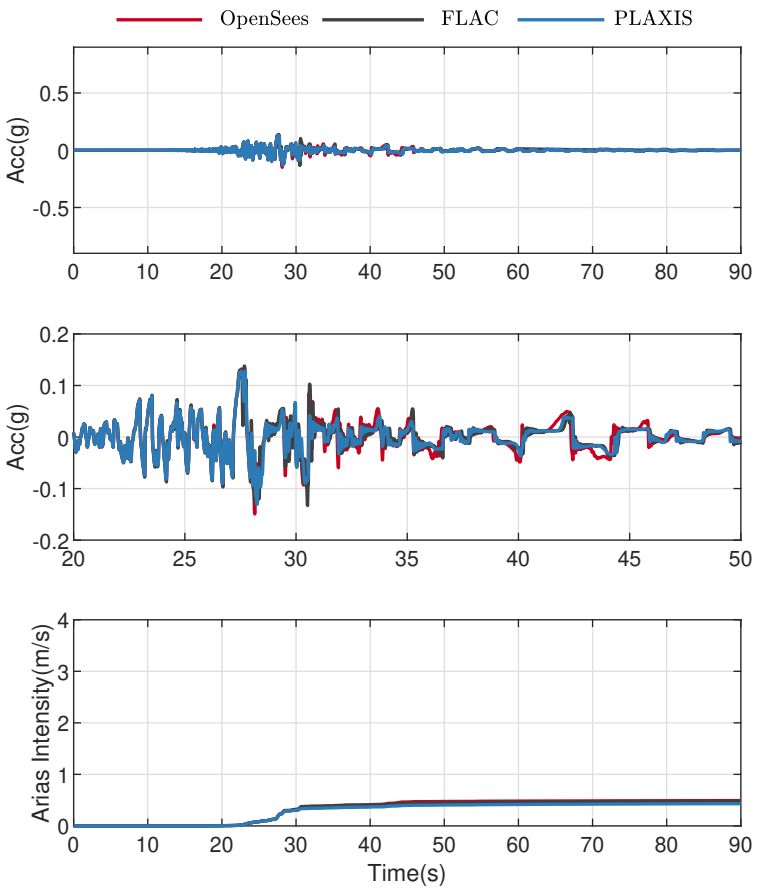

Figure A.17: Comparison of acceleration time histories at surface obtained using OpenSees, FLAC, and PLAXIS for motion RSN1203.

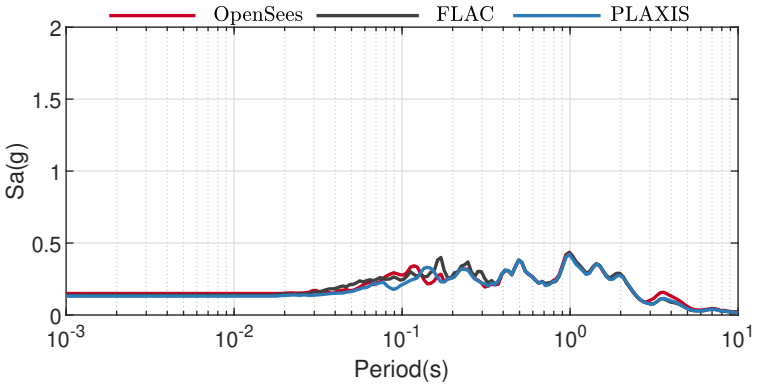

Figure A.18: Comparison of acceleration response spectra at surface obtained using OpenSees, FLAC, and PLAXIS for motion RSN1203.

A.3 N10T6

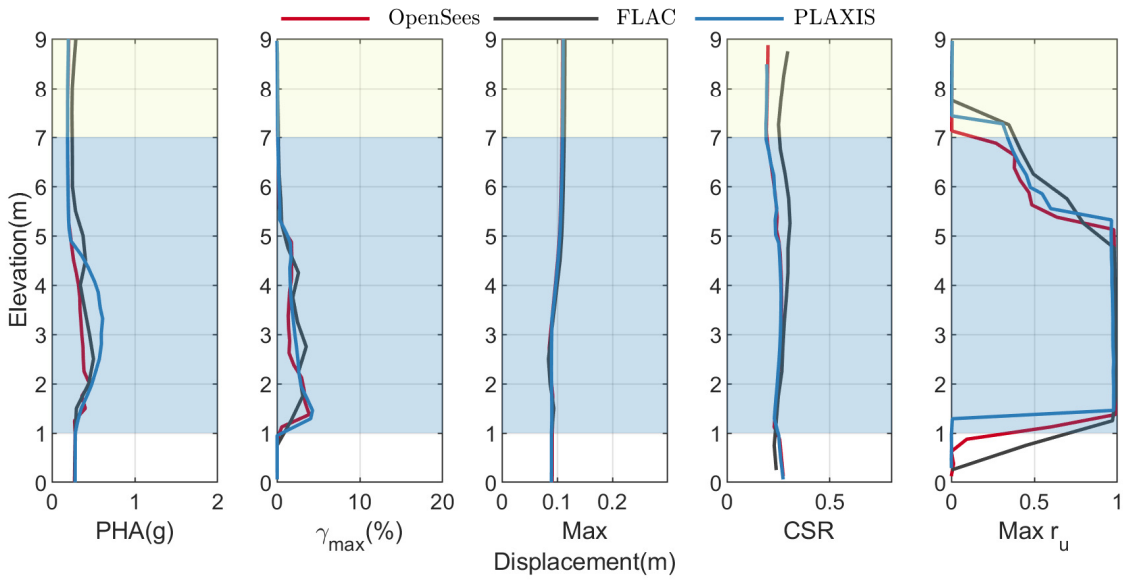

Figure A.19: Comparison of profile of PHA, γ_{max}, maximum displacement, CSR, and max r_u obtained using OpenSees, FLAC, and PLAXIS for motion RSN766.

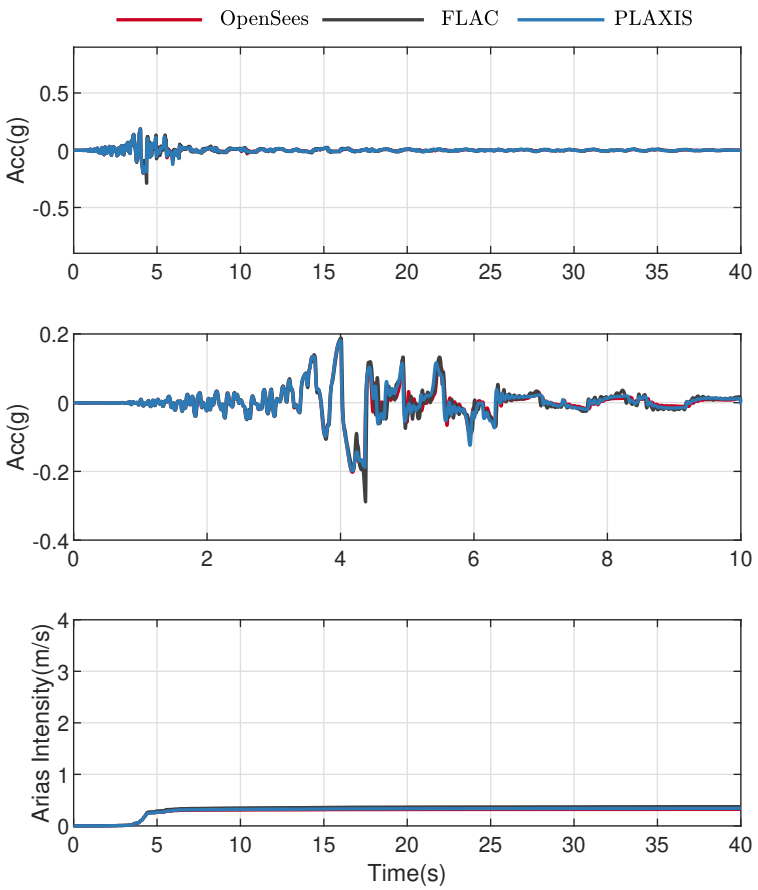

Figure A.20: Comparison of acceleration time histories at surface obtained using OpenSees, FLAC, and PLAXIS for motion RSN766.

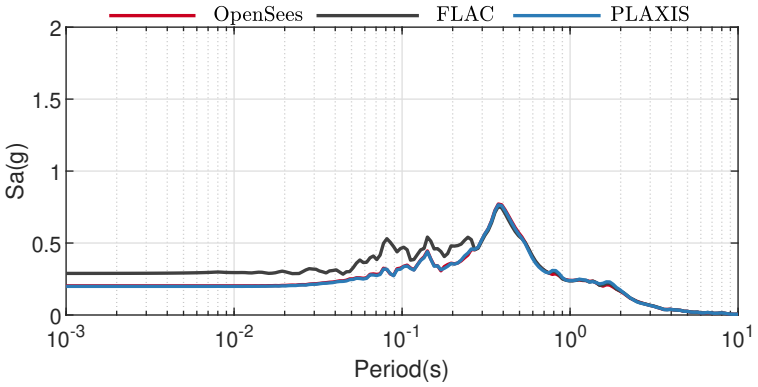

Figure A.21: Comparison of acceleration response spectra at surface obtained using OpenSees, FLAC, and PLAXIS for motion RSN766.

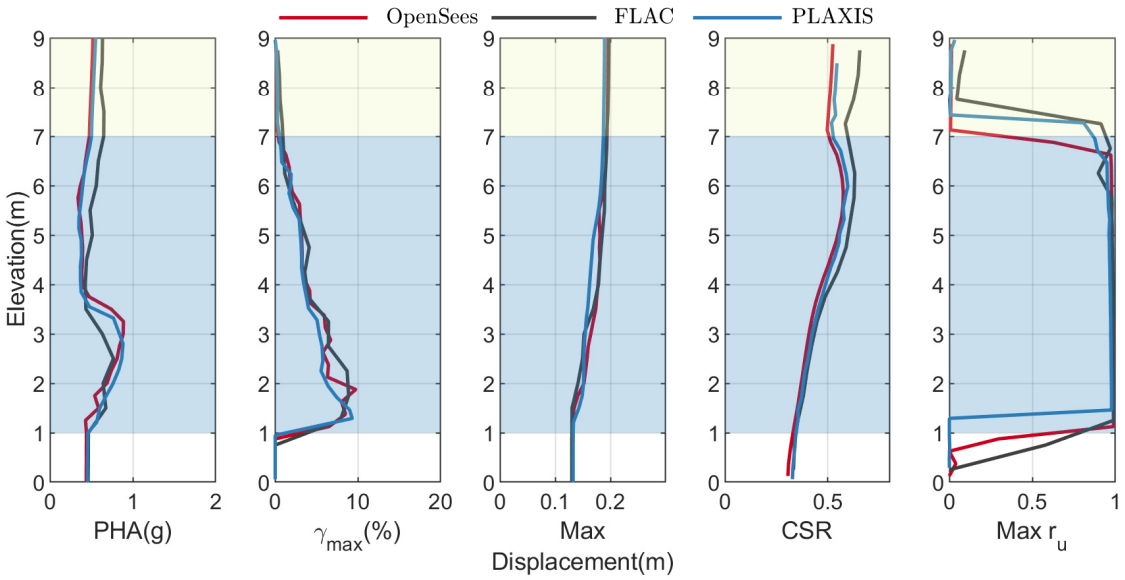

Figure A.22: Comparison of profile of PHA, γ_{max}, maximum displacement, CSR, and max r_u obtained using OpenSees, FLAC, and PLAXIS for motion RSN963.

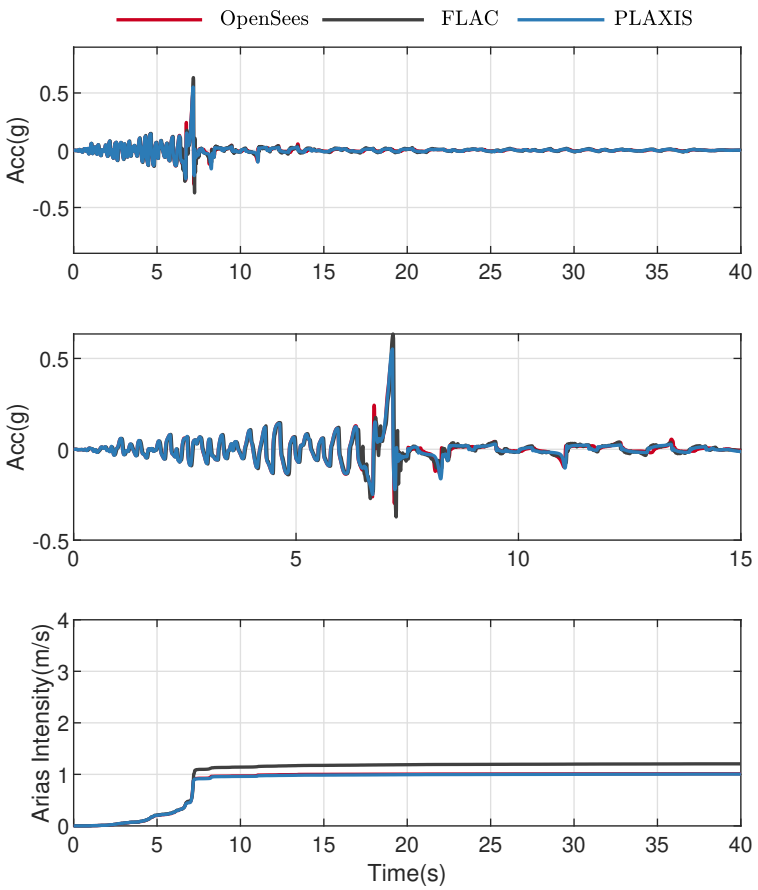

Figure A.23: Comparison of acceleration time histories at surface obtained using OpenSees, FLAC, and PLAXIS for motion RSN963.

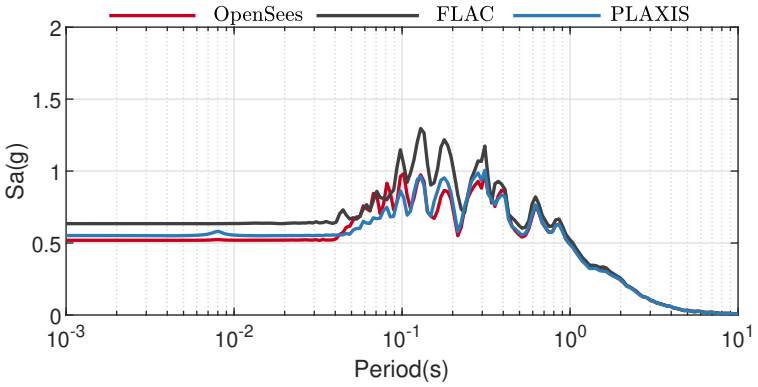

Figure A.24: Comparison of acceleration response spectra at surface obtained using OpenSees, FLAC, and PLAXIS for motion RSN963.

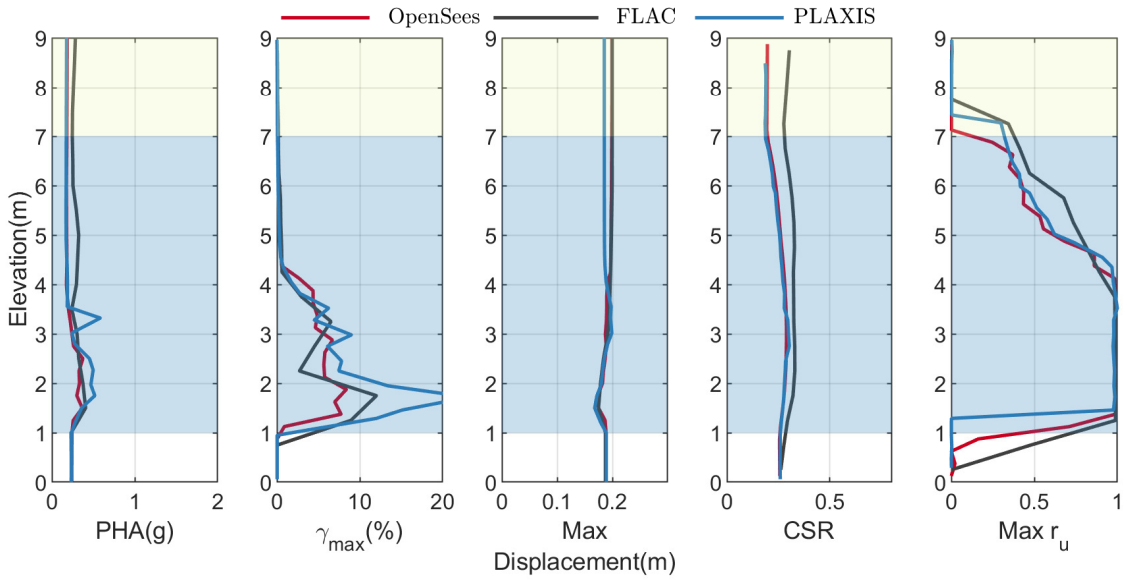

Figure A.25: Comparison of profile of PHA, γ_{max}, maximum displacement, CSR, and max r_u obtained using OpenSees, FLAC, and PLAXIS for motion RSN1203.

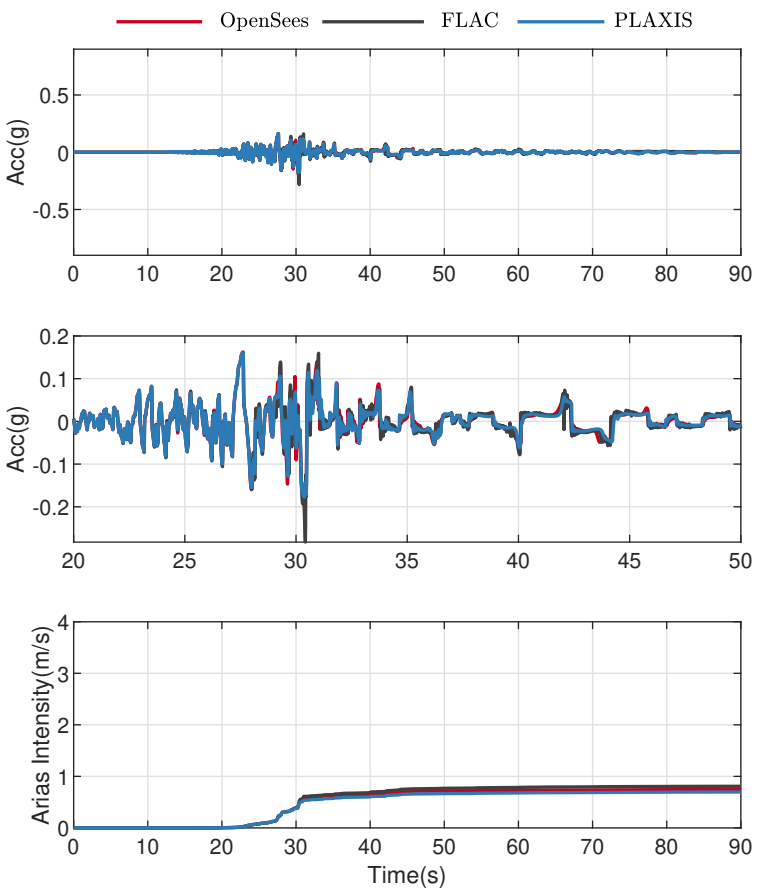

Figure A.26: Comparison of acceleration time histories at surface obtained using OpenSees, FLAC, and PLAXIS for motion RSN1203.

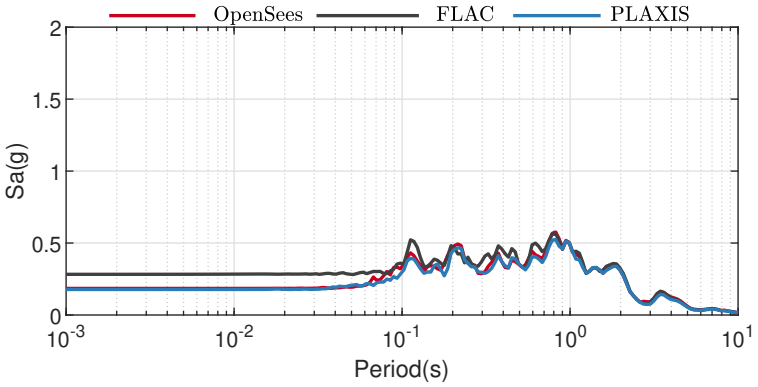

Figure A.27: Comparison of acceleration response spectra at surface obtained using OpenSees, FLAC, and PLAXIS for motion RSN1203.

A.4 N20T3

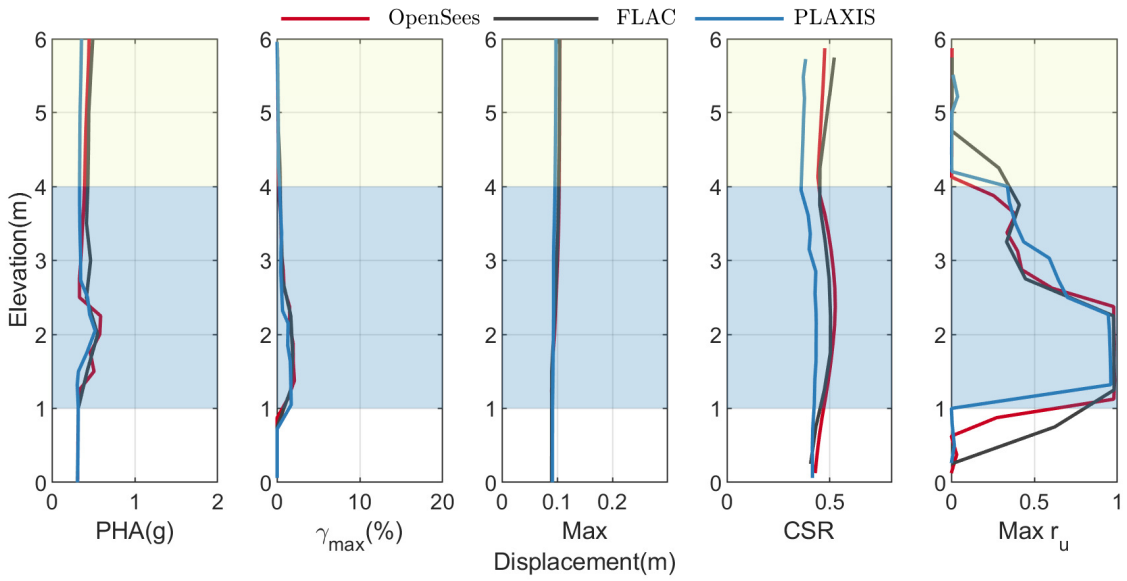

Figure A.28: Comparison of profile of PHA, γ_{max}, maximum displacement, CSR, and max r_u obtained using OpenSees, FLAC, and PLAXIS for motion RSN766.

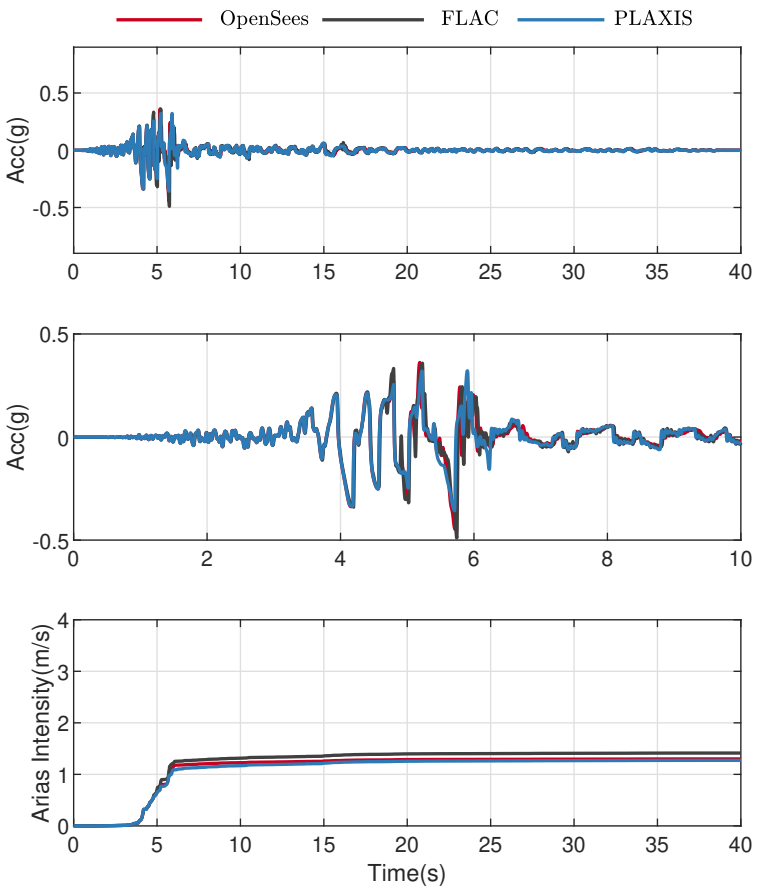

Figure A.29: Comparison of acceleration time histories at surface obtained using OpenSees, FLAC, and PLAXIS for motion RSN766.

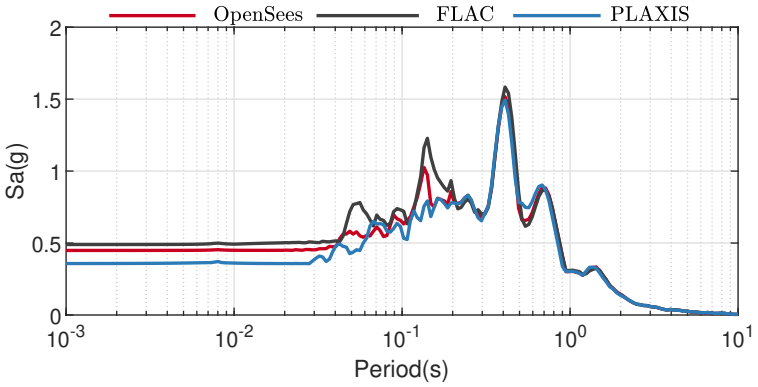

Figure A.30: Comparison of acceleration response spectra at surface obtained using OpenSees, FLAC, and PLAXIS for motion RSN766.

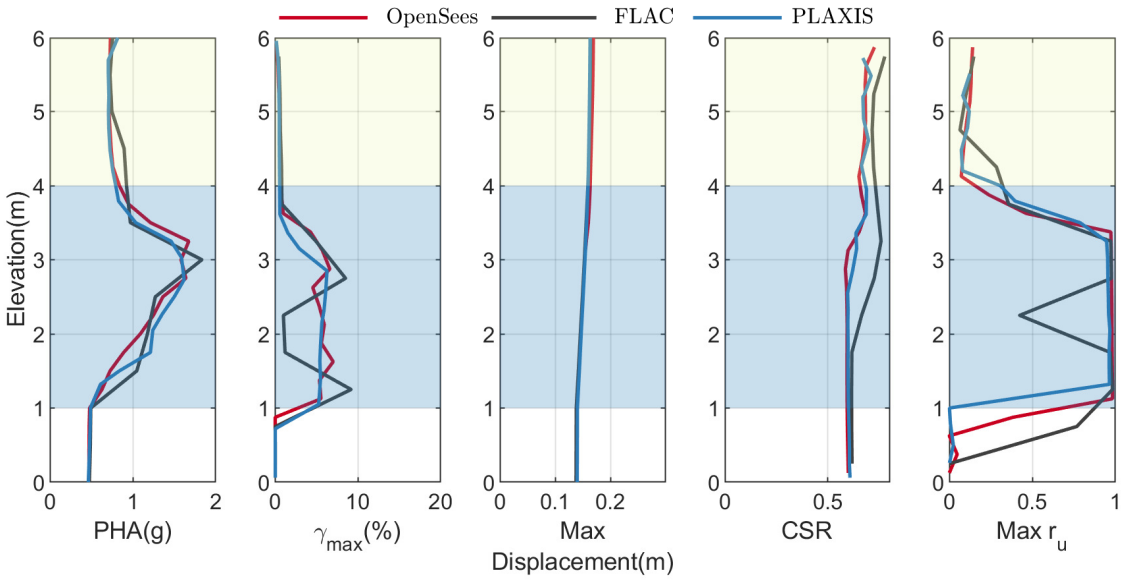

Figure A.31: Comparison of profile of PHA, γ_{max}, maximum displacement, CSR, and max r_u obtained using OpenSees, FLAC, and PLAXIS for motion RSN963.

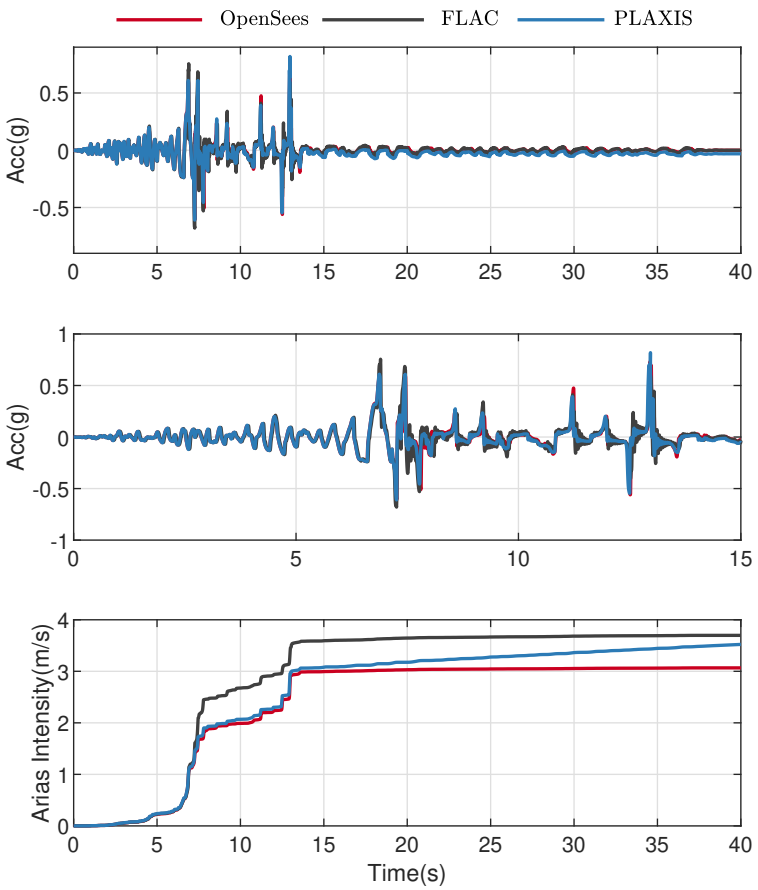

Figure A.32: Comparison of acceleration time histories at surface obtained using OpenSees, FLAC, and PLAXIS for motion RSN963.

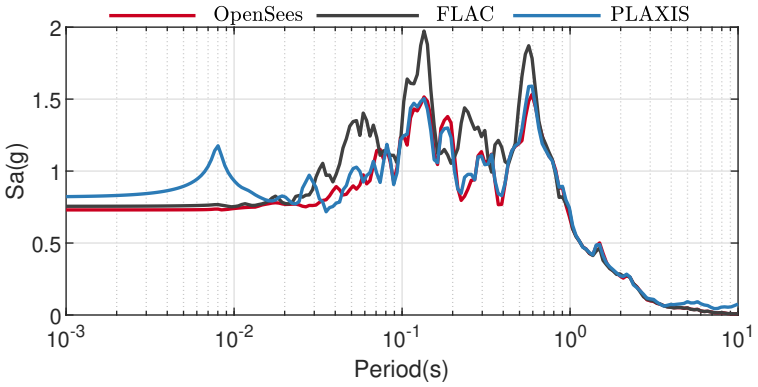

Figure A.33: Comparison of acceleration response spectra at surface obtained using OpenSees, FLAC, and PLAXIS for motion RSN963.

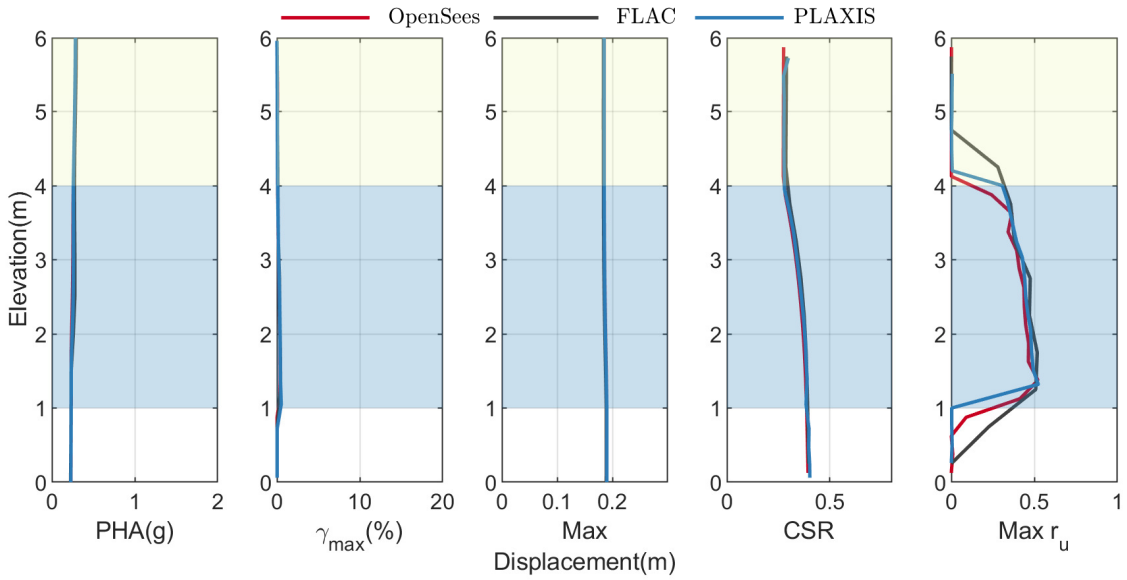

Figure A.34: Comparison of profile of PHA, γ_{max}, maximum displacement, CSR, and max r_u obtained using OpenSees, FLAC, and PLAXIS for motion RSN1203.

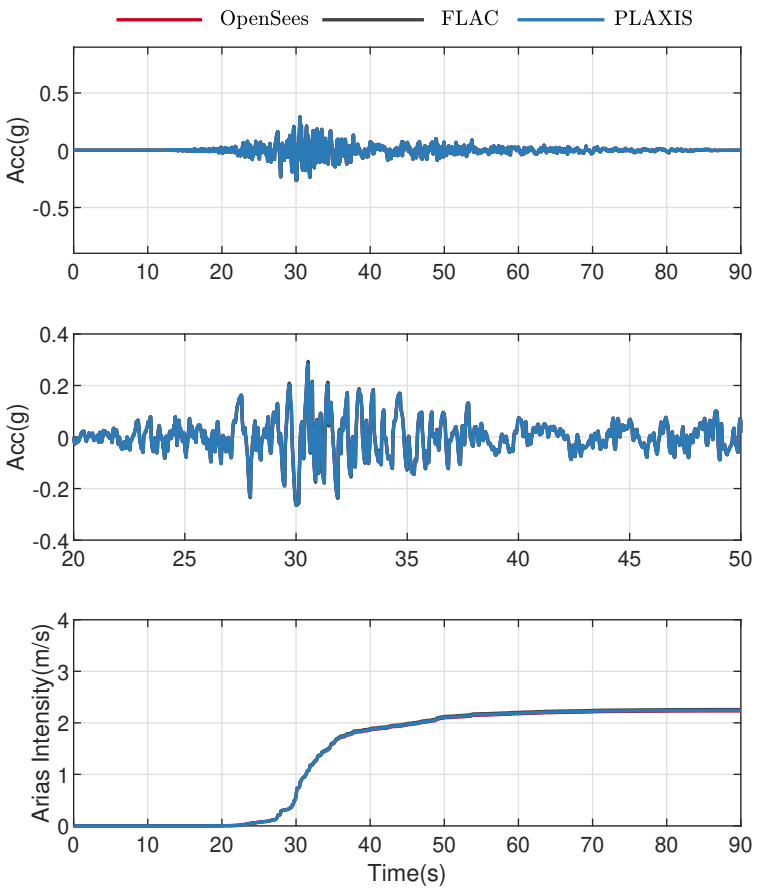

Figure A.35: Comparison of acceleration time histories at surface obtained using OpenSees, FLAC, and PLAXIS for motion RSN1203.

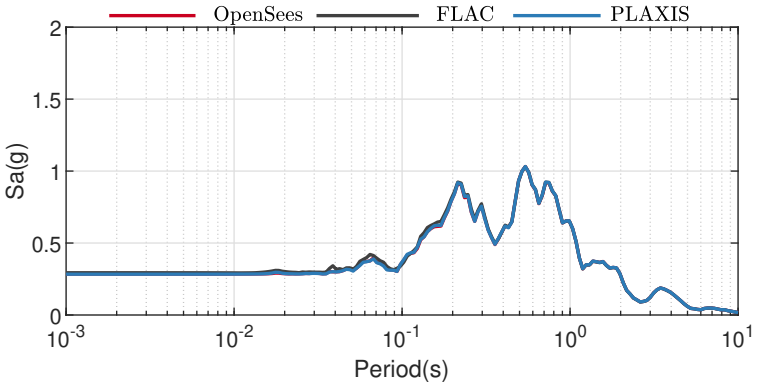

Figure A.36: Comparison of acceleration response spectra at surface obtained using OpenSees, FLAC, and PLAXIS for motion RSN1203.

A.5 N20T6

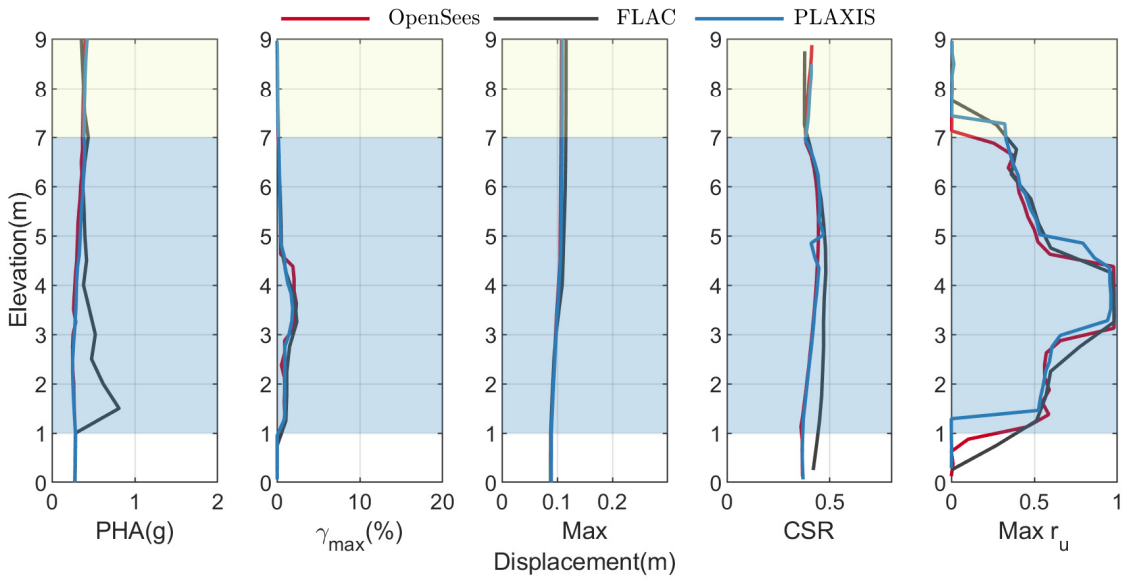

Figure A.37: Comparison of profile of PHA, γ_{max}, maximum displacement, CSR, and max r_u obtained using OpenSees, FLAC, and PLAXIS for motion RSN766.

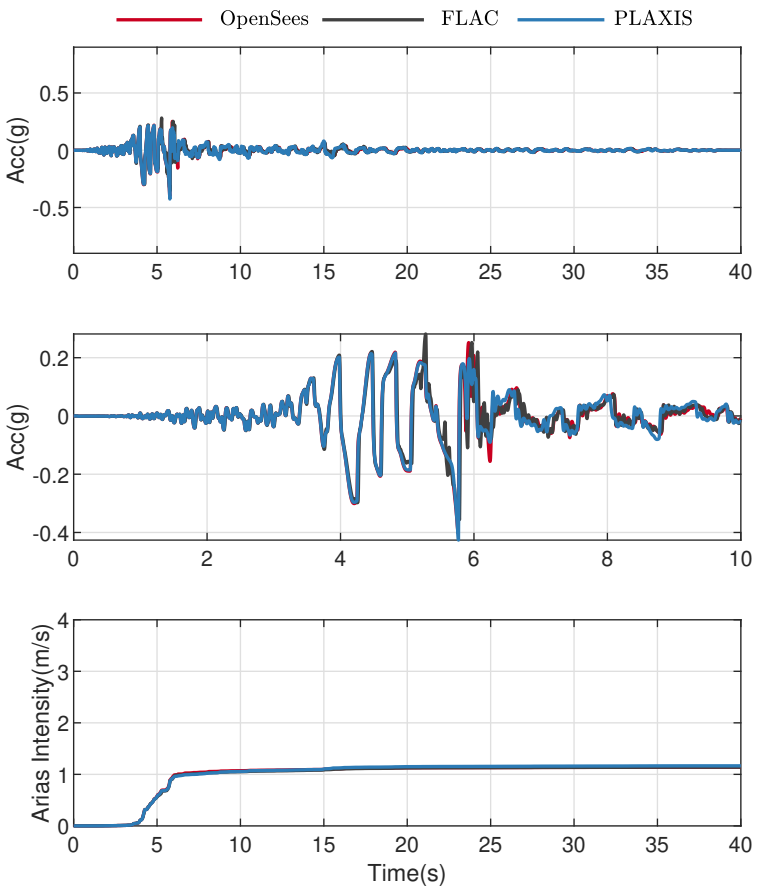

Figure A.38: Comparison of acceleration time histories at surface obtained using OpenSees, FLAC, and PLAXIS for motion RSN766.

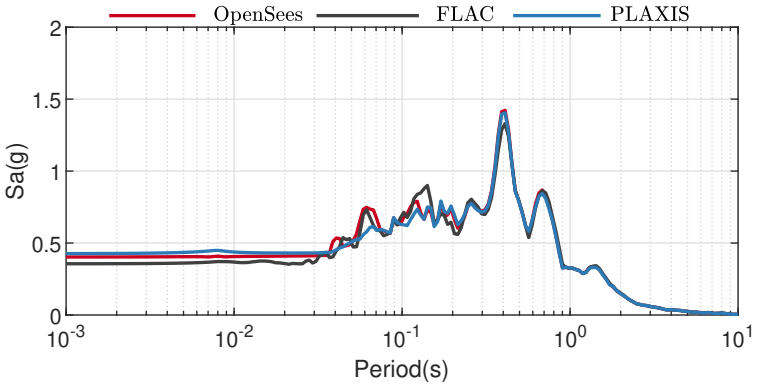

Figure A.39: Comparison of acceleration response spectra at surface obtained using OpenSees, FLAC, and PLAXIS for motion RSN766.

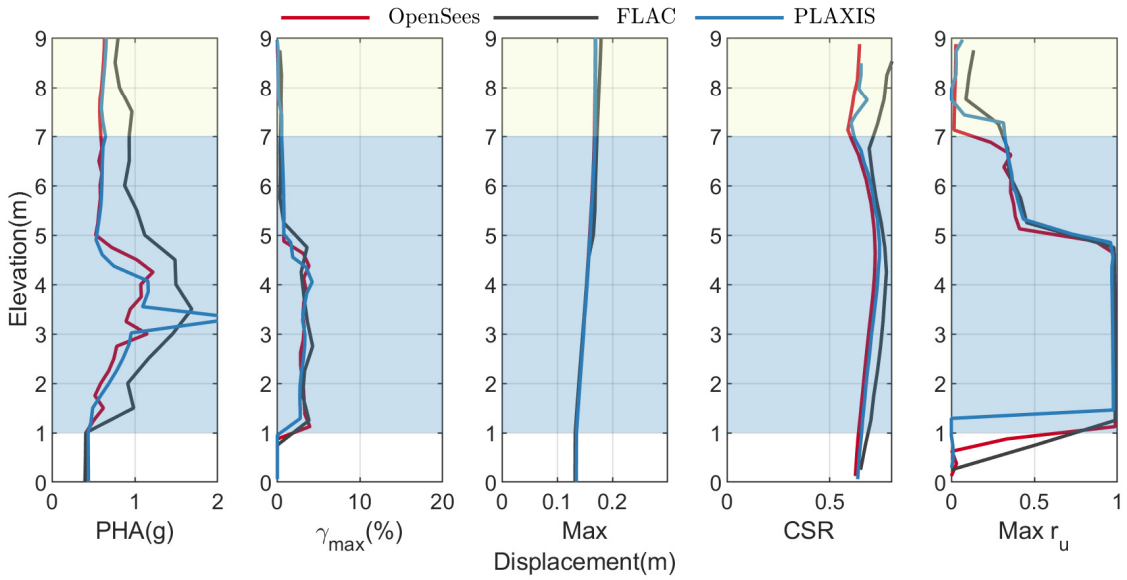

Figure A.40: Comparison of profile of PHA, γ_{max}, maximum displacement, CSR, and max r_u obtained using OpenSees, FLAC, and PLAXIS for motion RSN963.

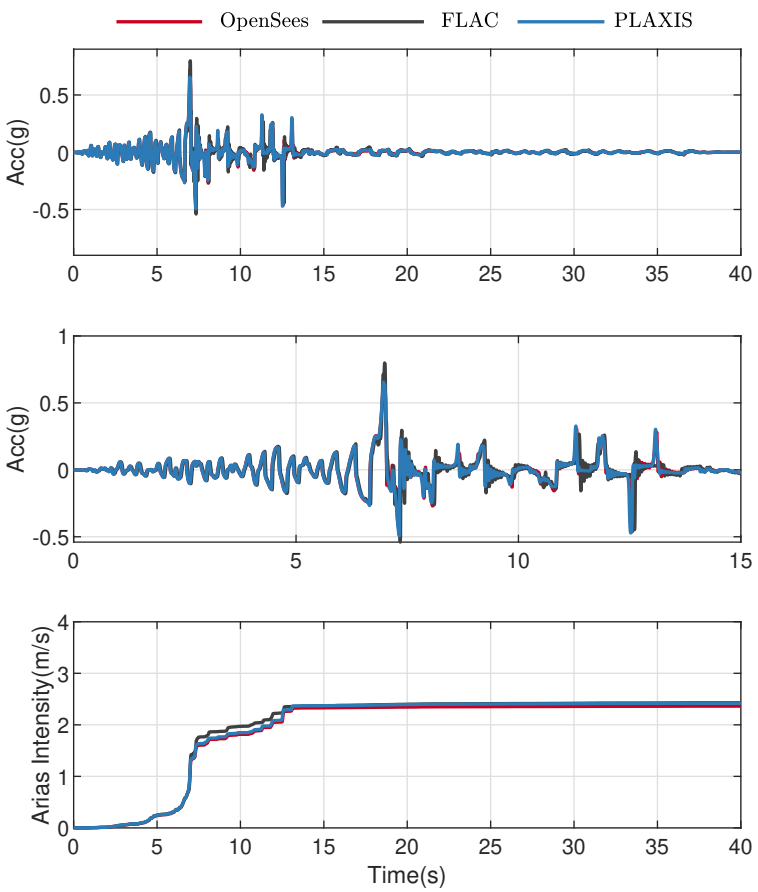

Figure A.41: Comparison of acceleration time histories at surface obtained using OpenSees, FLAC, and PLAXIS for motion RSN963.

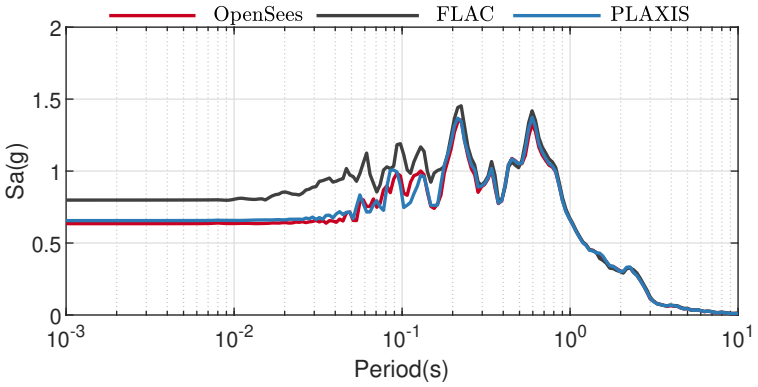

Figure A.42: Comparison of acceleration response spectra at surface obtained using OpenSees, FLAC, and PLAXIS for motion RSN963.

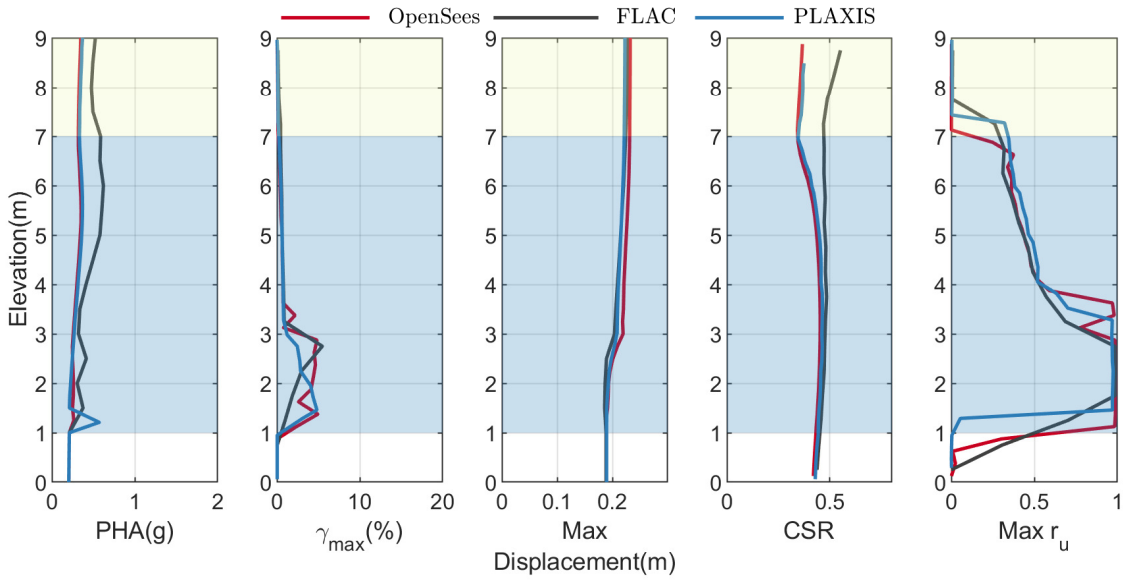

Figure A.43: Comparison of profile of PHA, γ_{max}, maximum displacement, CSR, and max r_u obtained using OpenSees, FLAC, and PLAXIS for motion RSN1203.

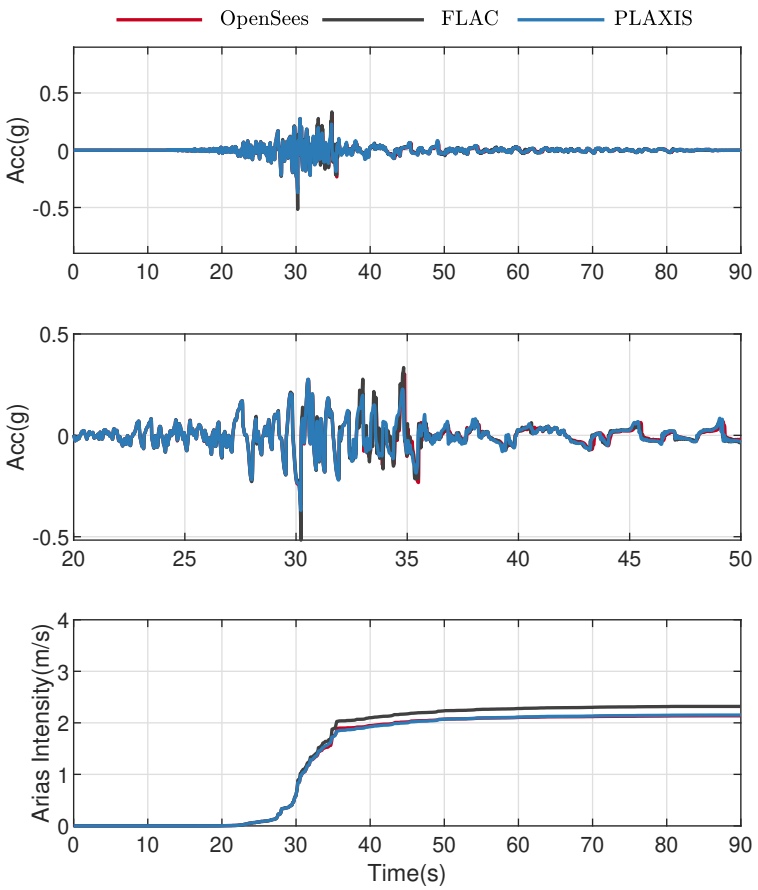

Figure A.44: Comparison of acceleration time histories at surface obtained using OpenSees, FLAC, and PLAXIS for motion RSN1203.

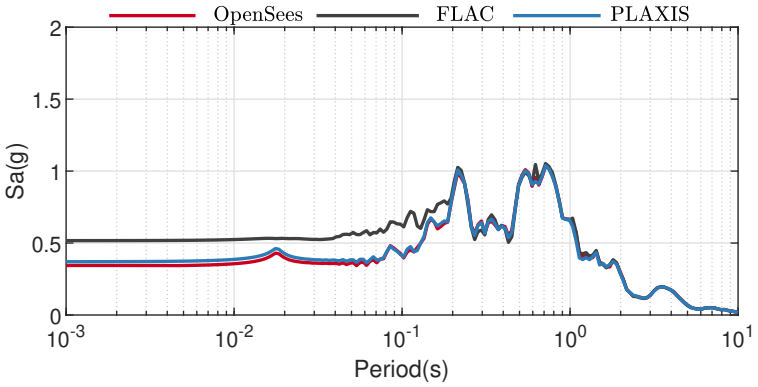

Figure A.45: Comparison of acceleration response spectra at surface obtained using OpenSees, FLAC, and PLAXIS for motion RSN1203.

A.6 ADDITIONAL SLOPING GROUND RESULTS

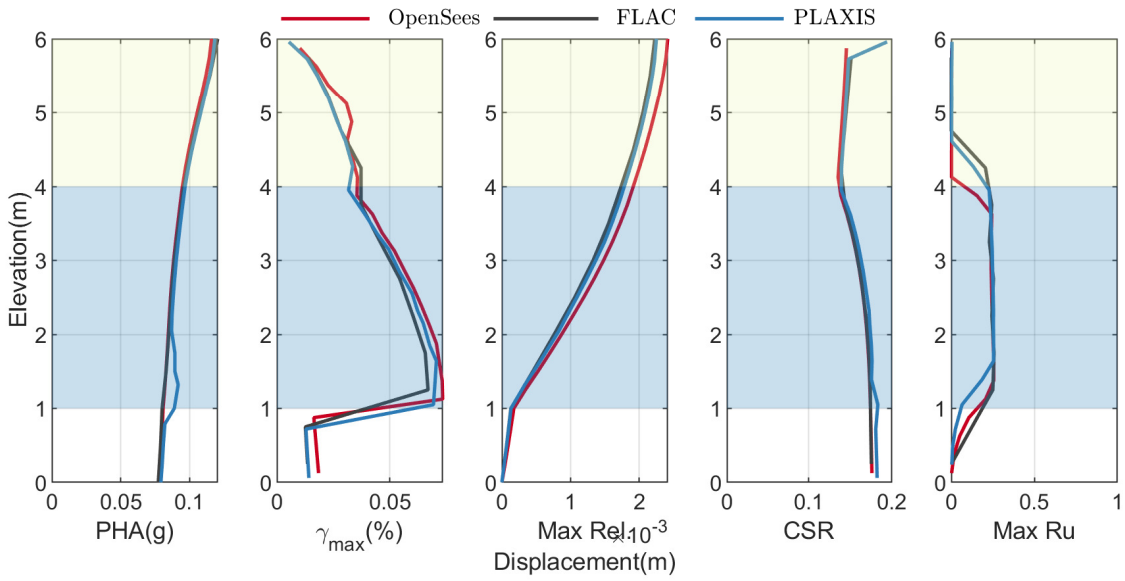

Figure A.46: Comparison of PHA, γ_{max}, maximum displacement, CSR, and max r_u obtained using OpenSees, FLAC and PLAXIS for Motion RSN766 and a_{max} = 0.1g.

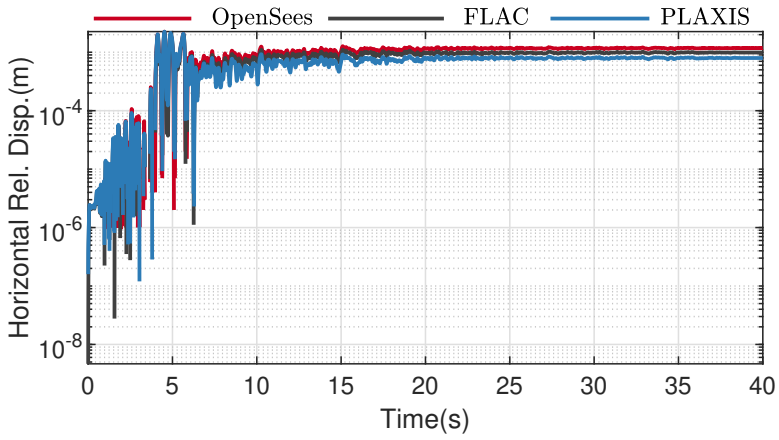

Figure A.47: Comparison of horizontal displacement at the surface obtained using OpenSees, FLAC, and PLAXIS for Motion RSN766 and a_{max} = 0.1g.

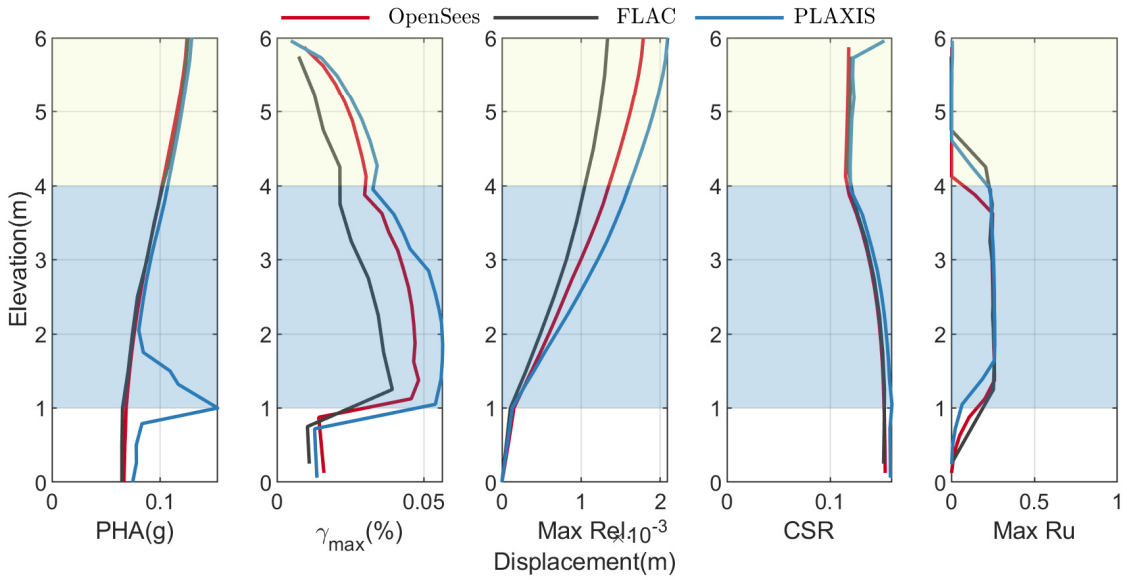

Figure A.48: Comparison of PHA, γ_{max}, maximum displacement, CSR, and max r_u obtained using OpenSees, FLAC and PLAXIS for Motion RSN963 and a_{max} = 0.1g.

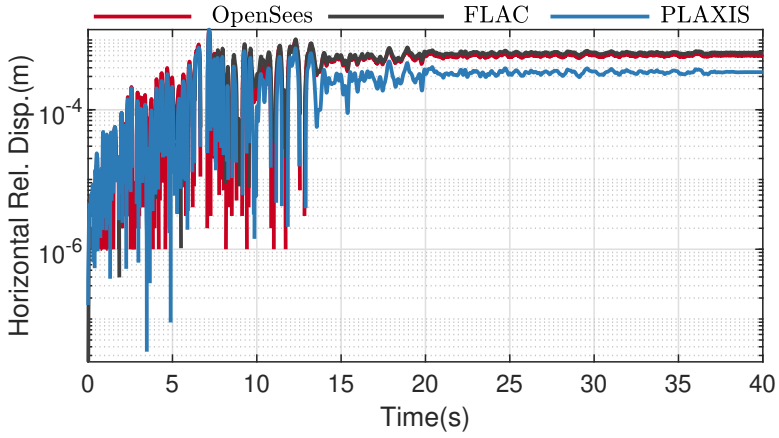

Figure A.49: Comparison of horizontal displacement at the surface obtained using OpenSees, FLAC, and PLAXIS for Motion RSN963 and a_{max} = 0.1g.

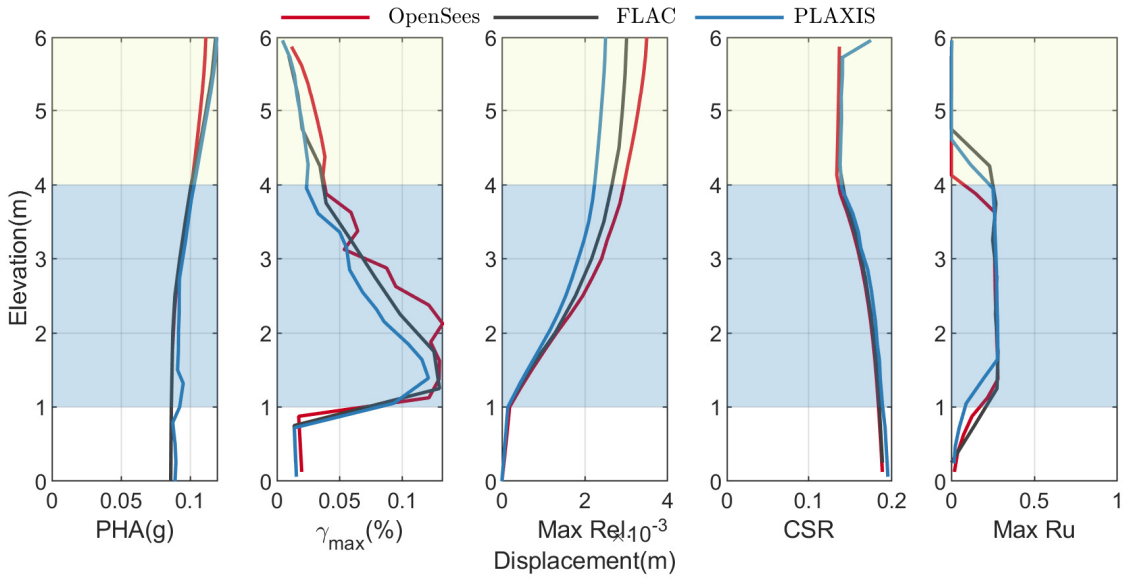

Figure A.50: Comparison of PHA, γ_{max}, maximum displacement, CSR, and max r_u obtained using OpenSees, FLAC and PLAXIS for Motion RSN1203 and a_{max} = 0.1g.

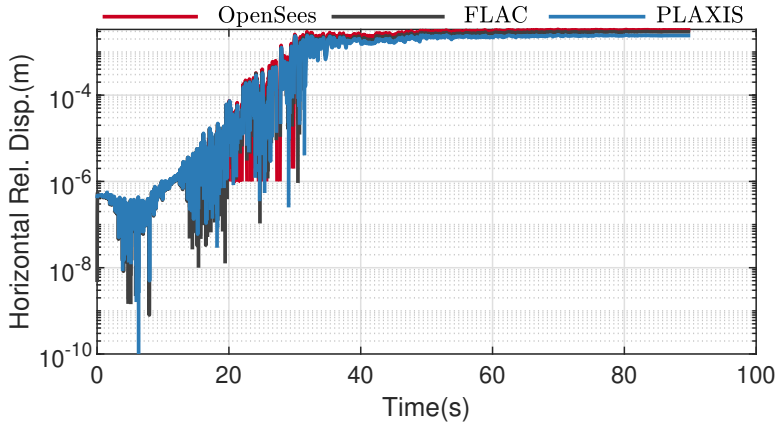

Figure A.51: Comparison of horizontal displacement at the surface obtained using OpenSees, FLAC, and PLAXIS for Motion RSN1203 and a_{max} = 0.1g.

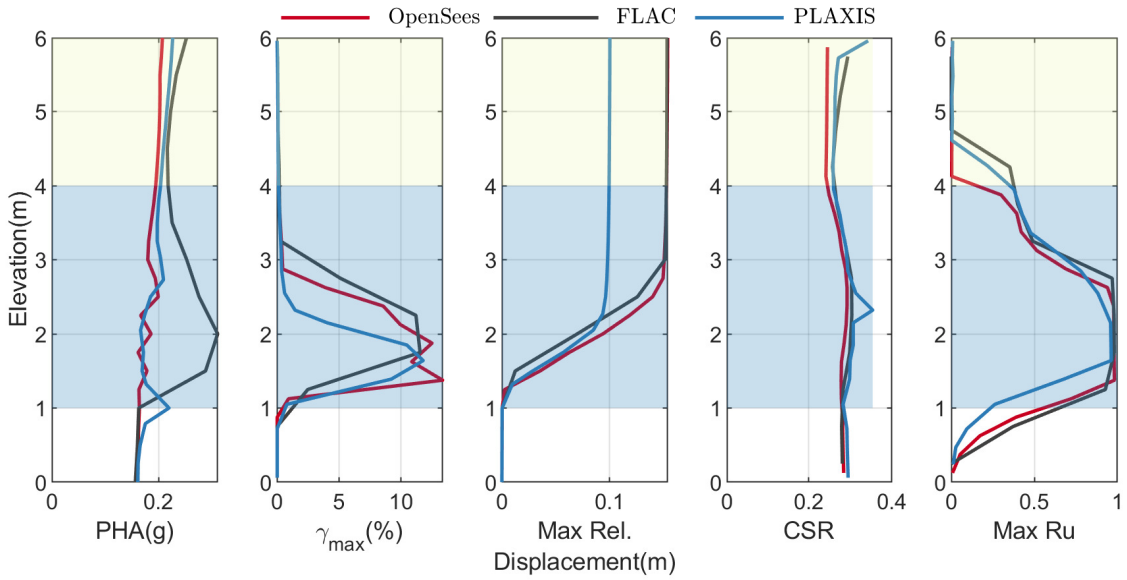

Figure A.52: Comparison of PHA, γ_{max}, maximum displacement, CSR, and max r_u obtained using OpenSees, FLAC and PLAXIS for Motion RSN766 and a_{max} = 0.2g.

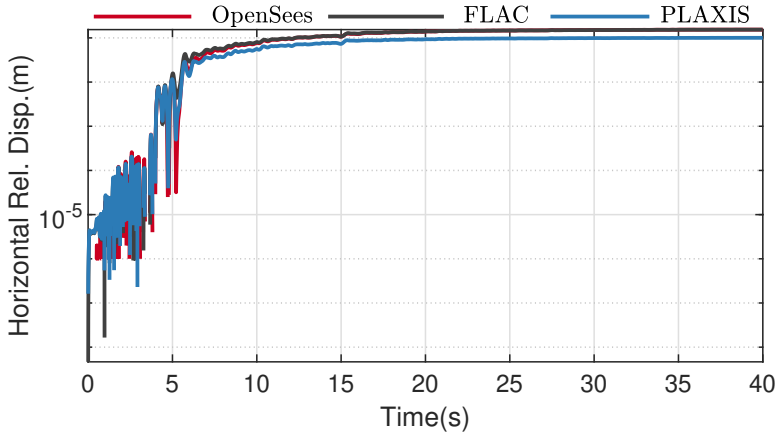

Figure A.53: Comparison of horizontal displacement at the surface obtained using OpenSees, FLAC, and PLAXIS for Motion RSN766 and a_{max} = 0.2g.

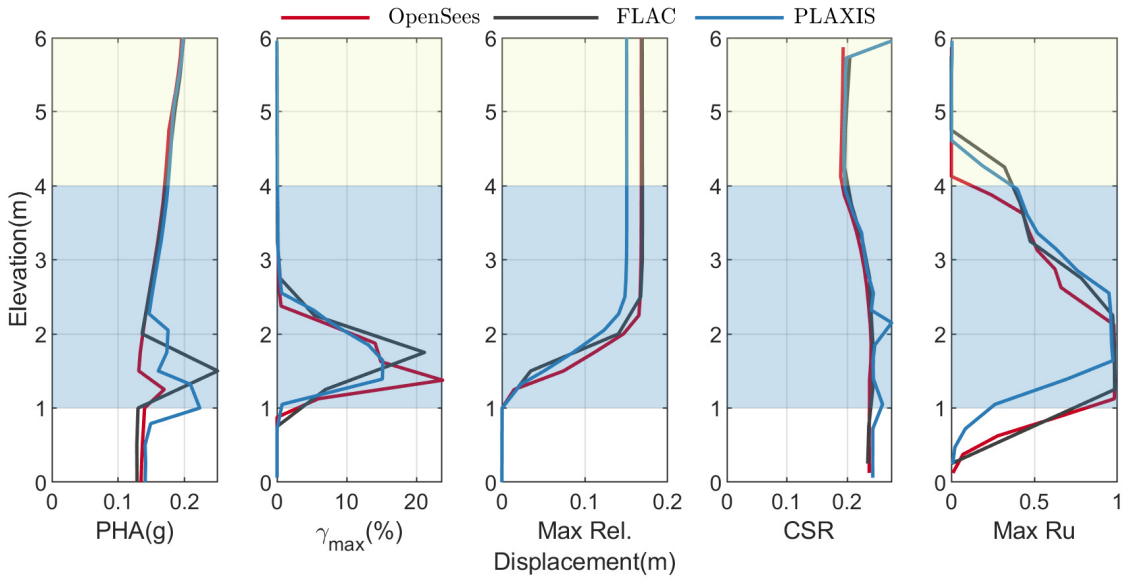

Figure A.54: Comparison of PHA, γ_{max}, maximum displacement, CSR, and max r_u obtained using OpenSees, FLAC and PLAXIS for Motion RSN963 and a_{max} = 0.2g.

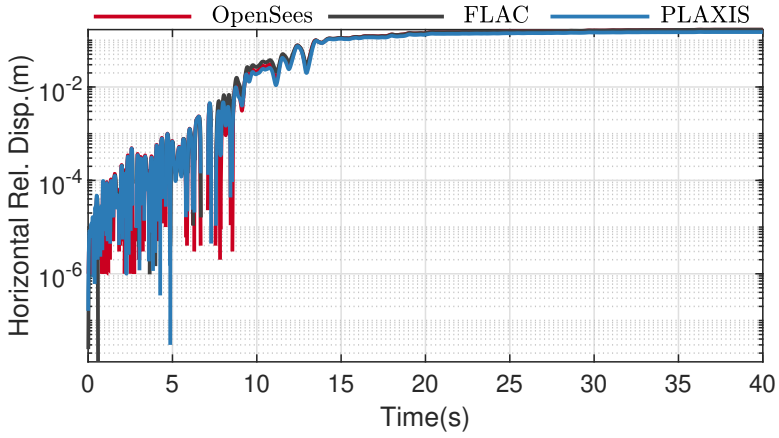

Figure A.55: Comparison of horizontal displacement at the surface obtained using OpenSees, FLAC, and PLAXIS for Motion RSN963 and a_{max} = 0.2g.

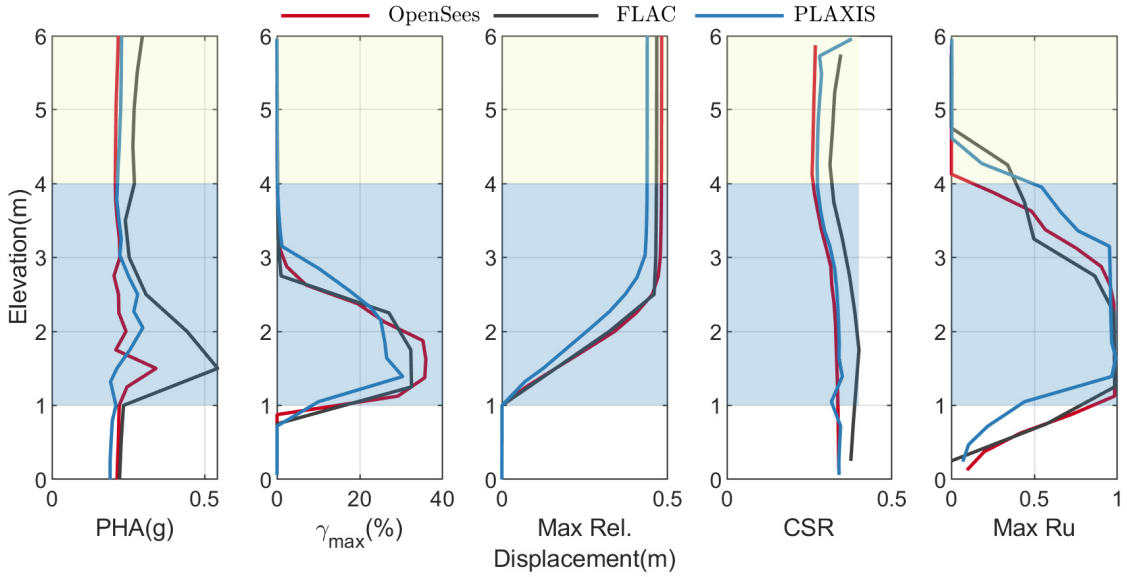

Figure A.56: Comparison of PHA, γ_{max}, maximum displacement, CSR, and max r_u obtained using OpenSees, FLAC and PLAXIS for Motion RSN1203 and a_{max} = 0.2g.

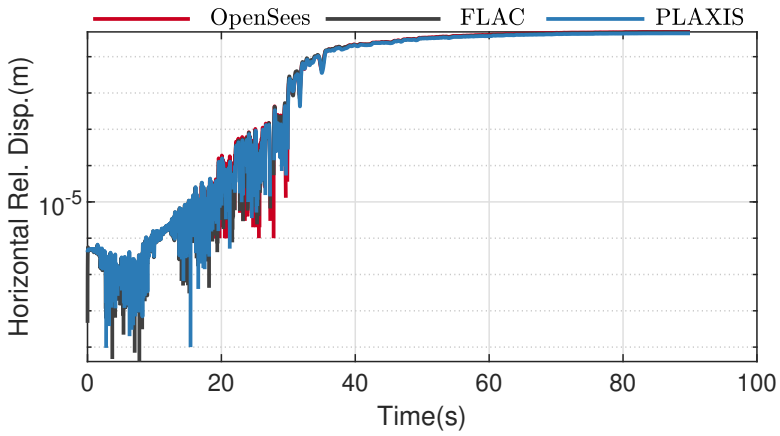

Figure A.57: Comparison of horizontal displacement at the surface obtained using OpenSees, FLAC, and PLAXIS for Motion RSN1203 and a_{max} = 0.2g.

The Pacifi c Earthquake Engineering Research Center (PEER) is a multi-institutional research and education center with headquarters at the University of California, Berkeley. Investigators from over 20 universities, several consulting companies, and researchers at various state and federal government agencies contribute to research programs focused on performance-based earthquake engineering.

These research programs aim to identify and reduce the risks from major earthquakes to life safety and to the economy by including research in a wide variety of disciplines including structural and geotechnical engineering, geology/seismology, lifelines, transportation, architecture, economics, risk management, and public policy.

PEER is supported by federal, state, local, and regional agencies, together with industry partners.

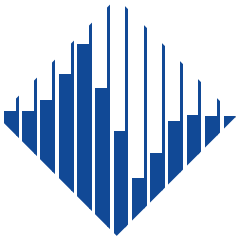

PEER Core Institutions

University of California, Berkeley (Lead Institution)
California Institute of Technology
Oregon State University
Stanford University
University of California, Davis
University of California, Irvine
University of California, Los Angeles
University of California, San Diego
University of Nevada, Reno
University of Southern California
University of Washington

PEER reports can be ordered at https://peer.berkeley.edu/peer-reports or by contacting

Pacific Earthquake Engineering Research Center
University of California, Berkeley
325 Davis Hall, Mail Code 1792
Berkeley, CA 94720-1792
Tel: 510-642-3437
Email: peer_center@berkeley.edu

ISSN 2770-8314
https://doi.org/10.55461/SJEU6160